A SEMI-QUANTITATIVE SCHLIEREN HIGH-SPEED FLOW DIAGNOSTIC: ANALYSIS OF HIGH-PRESSURE-RATIO, OVEREXPANDED PLANAR FLOW IN ROCKET NOZZLES

by

Karen Thorsett-Hill

A dissertation submitted to the faculty of
The University of North Carolina at Charlotte
in partial fulfillment of the requirements
for the degree of Doctor of Philosophy in
Mechanical Engineering

Charlotte

2012

Approved by

_____
Dr. Russell Keanini

_____
Dr. Peter Tkacik

_____
Dr. David Weggel

_____
Dr. Yogendra Kakad

ABSTRACT

KAREN THORSETT-HILL. A semi-quantitative schlieren high-speed flow diagnostic: analysis of high-pressure-ratio, overexpanded planar flow in rocket nozzles. (Under the direction of (DR. RUSS KEANINI)

This work introduces a semi-quantitative schlieren (SQS) method which is used to qualitatively and quantitatively analyze complex, unsteady, compressible flows in a small, planar convergent-divergent nozzle. A basic schlieren system is used to image the evolution in time of complex supersonic flow structures, including Prandtl-Meyer expansion fans, internal shocks, near-wall oblique shocks, quasi-normal shocks, shock/boundary layer interactions, shock/shock interactions, and shock trains. The first images of shock trains in high nozzle-pressure-ratio flows are shown, and the underlying processes are described. A flow-field decomposition method is presented which allows the entire flow field to be separated into unit processes and analyzed. Various methods of analysis are presented, including a new method for the determination of node locations along a defined nozzle wall geometry using the method of characteristics. A numerical solution is developed for the analysis of a blow-down process. Computer programs which implement these solutions are presented.

ACKNOWLEDGMENTS

I would like to gratefully and sincerely thank my advisor, Dr. Russ Keanini for his guidance, patience, and, most importantly, his friendship during my graduate studies at UNC Charlotte. His mentorship was paramount in providing a well-rounded experience. It is rare that a graduate student is given the opportunity to develop self-sufficiency and individuality in research by being allowed to work with such independence. I would also like to thank Dr. Peter Tkacik for developing great experiments which were the foundation of this dissertation. His support was invaluable. I would like to thank Dr. Weggel and Dr. Kakad for serving on my committee.

On a personal note, I would like to thank Dr. Sue Holl for encouraging me to return to school and earn my Ph.D. and for guiding me towards a suitable and challenging dissertation topic. I owe deep gratitude to Dr. Sam Thomason, my life-long mentor, who, more than anyone else, has positively influenced my life's course and career and who introduced me to my husband, Dr. Jerre Hill. Without Jerre's extreme patience, support, advice, and encouragement, there is no way that I could have accomplished this dissertation.

Most fondly, this dissertation is dedicated to my father. Thank you for being proud of me and believing in me. I miss you so incredibly much, Dad.

TABLE OF CONTENTS

CHAPTER 1: OVERVIEW OF AVAILABLE DIAGNOSTICS FOR HIGH-SPEED FLOW

1.1 Introduction

Over the past 60 years, a number of diagnostics have been developed for investigating high-speed flows. Unfortunately, experimental high-speed flow test facilities are typically difficult to access and expensive to use [1]. Indeed, most existing high-speed flow research has been carried out at specialized university and government-sponsored laboratories.

The primary objective of this dissertation centers on development of an accessible, low-cost approach for experimentally investigating complex, high-speed flows. Prior to describing this new approach, available experimental and numerical methods for studying compressible flow are reviewed.

1.2 Current experimental methods

Available experimental high-speed flow diagnostics include shadowgraph methods [2,3,4], various pressure measurement techniques [5,6], schlieren methods [2,7,8], interferometric techniques [9,10,11], and various hot wire [12,13], hot film [14,15], Mie scattering [16], molecular tagging velocimetry [17], laser fluorescence, Raman scattering [18], laser Doppler velocimetry [12], and Particle Image Velocimetry (PIV) [12] methods.

Photonic methods play a central role in compressible flow research. These techniques can be grouped into one of four categories: i) methods based on light

scattering by small particles or molecules, ii) methods that rely on light-induced atomic or molecular fluorescence, iii) techniques that measure phase shifts produced by variations in the index of refraction, and iv) methods that mark the flow via molecular tags. Of relevance to the present investigation, all of these methods have the potential of providing nominally frozen-in-time images of the flow field; this is achieved when the imaging time scale is much shorter than the unsteady flow time scale.

1.2.1 Light scattering methods

Light scattering methods introduce small particles into a flow and track particle motion using various light-based interrogation techniques. For example, particle image velocimetry (PIV) measures velocity fields by seeding the flow with particles (e.g., dye, smoke) and correlating close-in-time images of the displaced particle field [12]. In all light scattering approaches, it is implicitly assumed that particles faithfully follow motion of the fluid. Due to particle inertia, however, particularly in high speed flows, particle paths may diverge significantly from flow path lines [12].

Smoke injection, comprising a widely-used scattering method, produced the first quantitative volumetric flow field data [19]. Time lines were introduced by Lippisch [20]. This method uses pulsed-smoke injection in conjunction with a high-speed video to produce and portray velocity distributions within the flow. Thin light sheets generated by high intensity lamps [21] or lasers [22] have extended this technique so that two-dimensional cross sections of three-dimensional flow fields can be visualized. By pulsing the light source or using a short time gate on the camera [22], the fluid motion can be frozen to give an instantaneous cross section of mixing phenomena or complex structures. If separate particles are distinguishable, two-dimensional velocity fields can be

mapped by measuring the length and direction of the particle streak trajectories in the image and relating that exposure to the time [24, 25]. Numerous examples of particle scattering in both air using smoke or seeded particulates, and in water using particulates or bubbles, are shown in Van Dyke's *An Album of Fluid Motion* [26].

Using high-powered lasers, scattering from molecules is a feasible alternative to particle scattering for flow diagnostics. This eliminates the problems associated with particle seeding and gives quantitative information on mixing, density, and temperature. Both Rayleigh scattering, which is direct scattering of light by molecules, and Raman scattering, which is inelastic scattering of light from molecules, have been used to generate cross-sectional images [27, 28]. The use of Raman scattering as a probe for gas diagnostics is well-established [29], as are numerous forms of nonlinear Raman spectroscopy [30]. Planar images of Raman scattering have been achieved, but require multiple passes of a very high-energy laser to generate enough scattered light to record an image.

1.2.2 Flourescence methods

Laser and fluorescence mechanisms are somewhat more complex than light scattering techniques. Here the exciting laser is scanned across an absorption line and the resulting fluorescence and Doppler shift are observed. Given these measurements, the local fluid temperature, velocity, and density can be extracted. Specifically, temperature and velocity correlate with the observed Doppler shift, while density largely determines the observed collision frequency [31]. By continuously recording the fluorescence intensity as the laser is tuned, velocity, temperature, and density at any point can be determined [31]. The dependence of fluorescence on laser frequency, transition length,

and the local environment significantly complicates these measurements, however. Velocity measurements rely on either the Doppler shift or line tagging, both of which are independent of the fluorescence intensity, and thus are somewhat easier to accomplish.

In compressible flows, either a naturally occurring species such as oxygen can be used [32, 33], or some fluorescing atomic or molecular species, such as sodium can be added to the flow and used as a marker [34]. Oxygen fluorescence can potentially be used to measure instantaneous temperatures and densities, but suffers from very low signals below a temperature of 500K. Direct Rayleigh scattering from molecules in a flow, together with simultaneous laser-induced fluorescence, can potentially yield two dimensional temperature cross-sections [35].

1.2.3 Molecular tagging methods

The direct interaction of light with molecules in the flow has led to the development of new laser tagging methods in which the flow is marked at a particular location and the motion of these marked molecules is followed to generate quantitative velocity information. In air, the stimulated Raman effect has been used to vibrationally excite thin lines of oxygen molecules which are subsequently interrogated to give instantaneous velocity profiles [36]. These techniques show great promise for generating volumetric velocity fields and can be coupled with Rayleigh scattering to simultaneously generate density cross-sections [37].

1.2.4 Simultaneous measurement methods

The method developed in this dissertation provides approximate, simultaneous measurements of the velocity, pressure, temperature, density, and Mach number fields in complex high-speed flow. In marked contrast to existing approaches for obtaining

multiple space-dependent field measurements, the proposed technique is inexpensive and easily implemented.

In this subsection, we briefly review existing multiple-property measurement methods. Approaches which do not introduce sensors directly into a flow, can be grouped into the same categories used for single-property measurements: flow marking by molecular tagging [34], atomic or molecular laser-induced fluorescence [34], light scattering by seeded particles or molecules native to the flow [32, 33, 38], and measurement of phase shifts resulting from variation in index of refraction caused by density gradients [39, 40, 41]. Of these, only laser-induced fluorescence allows the determination of at least three properties, namely temperature, velocity, and density [38].

It is important to emphasize, again, however, that all of these methods are complex, costly, require use of special equipment, and, often, must be performed in controlled laboratory environments. For instance, seeding often requires very specific seeding rates. Fluorescence with sodium requires careful control of seeding density on the order of 1 part per 100 million, and is not useful in low temperature air. Raman scattering, when used for generation of planar images in 3-dimensional flow fields, rests on acquisition of sufficient scattered light, which in turn, requires multiple passes of a very high energy laser. In some cases, the seed material must be heated before injection into a flow. This can introduce thermal distortion into the flow field. Likewise, seeding can also cause corrosion and environmental pollution [38]. Furthermore, in compressible flows, as noted, scattering particles often do not follow the flow in regions of steep velocity gradients [38].

1.3 Overview of computational fluid dynamics approaches

Computational modeling provides an alternative to experimental measurements when diagnosing high speed flows. Quantitative data acquired from computational fluid dynamics (CFD) analysis requires problem-specific tuning via validation of benchmark calculations through experimentation. Furthermore, while CFD can provide a global and qualitative understanding of complex, high-speed flows, it often fails to allow distillation of simpler models which may lead to a conceptually deeper understanding of a particularly complex flow. Computational treatments of complex supersonic flows can be time-consuming, expensive, and frequently fail to accurately capture important features of the flow field, such as shock structures or shock/boundary-layer interactions. For example, spectral methods for flows having Reynolds numbers on the order of 10^6 require on the order of 1000 to 5000 hours of time on teraflop machines, on the order of 10^9 grid points, and on the order of 1 terabytes of memory. Flows having order 10^7 Reynolds number and higher require (in principle) on the order of 350 years of teraflop computer time, 100-500 hours on petaflop computers, and on the order of 10^{11} grid points and 100 terabytes of memory [42].

Even large eddy simulations (LES) which allow capture of unsteady separated flows require an extremely large number of grid points and, hence, carry significant computational cost, especially at high Reynolds numbers [42].

Progress in computer speed has led to a shift from RANS (Reynolds Averaged Navier-Stokes) simulations to LES, which again allows for capture of unsteady separated flows. RANS calculations cannot capture the high level of unsteadiness that characterizes flows in which shock-induced separation occurs, however. Moreover, LES requires fine

mesh resolution near wall boundaries, limiting time-step size. The LES/RANS hybrid methodology represents a more powerful method, and is more cost-effective since it alleviates the requirement for fine mesh resolution near walls. The major drawback of this technique centers on its limited ability to accurately capture boundary layer transitions [42].

With regard to high Reynolds number nozzle flows, a major CFD modeling challenge centers on accurately predicting boundary layer behavior in the presence of shock waves. Hadjadj and Onofri's recent work, representing the state-of-the-art [43], modeled the transient flow in a supersonic, ideal nozzle [43]. Their computations gave insight into the complex time evolution of the nozzle starting process, showing the development and effect of shock wave propagation, as well as capturing the early stages of boundary layer separation from the wall [43]. More generally, nonlinear schemes such as the weighted-essentially-non-oscillatory (WENO) scheme, weighted compact non-linear scheme (WCNS), discontinuous Galerkin methods, and spectral volume methods are required to capture discontinuities such as shock waves [42].

High-order compact schemes may be used on non-uniform meshes with a variety of boundary conditions. When used to solve flows having steep gradients, however, such as those containing shock waves, these schemes often generate non-physical (numerical) oscillations [44]. There have been many approaches that modify high-order schemes in order to capture shock waves. For instance, for shock-turbulence interaction problems, Adams and Shariff [45, 46] proposed a high-order compact-essentially nonoscillatory scheme, and later, Pirozzoli introduced a conservative compact weighted essentially nonoscillatory (WENO) scheme [47]. Rizzetta et al. proposed a hybrid compact Roe-type

scheme in order to simulate supersonic compression ramp flows [48]. Deng and Zhang developed high-order compact schemes based on a weighted technique involving combinations of the above schemes [49].

1.4 Overview of schlieren methods

As noted, this dissertation proposes and describes a new, approximate approach for diagnosing complex high-speed flows. The method combines straightforward, schlieren imaging with simple theoretical modeling to develop an experimentally and theoretically consistent description of a given complex flow. Prior to describing the method, a brief overview of existing schlieren-based diagnostics is provided.

Schlieren imaging approaches are often used for qualitative analysis of flow fields, as are shadow methods, where the former has a much higher degree of resolution and sensitivity [50]. The schlieren technique allows for the visualization of fluid motion, does not require intrusion into the fluid, does not modify the flow in any way, and is commonly used to study density fields in transparent media, such as gases or liquids.

The physical principal underlying the schlieren approach, depicted in Figure 1-1, centers on the coupling between index of refraction and density. A light beam traveling in the z-direction passes through a medium whose index of refraction varies in the x- and y-directions; the light beam thus undergoes a small deviation of angle, α [12], where the magnitude of the deviation depends on the path integrated density gradient normal to the beam travel direction. The larger the integrated normal density gradient (where integration sums the local normal density gradient at all points along the beam path), the larger the deflection angle. Thus, collimated light rays passing through regions of significant (normal direction) density gradients experience larger deviations than rays

passing through lower gradient regions. In the present investigation, where a portion of the collimated light passes through, for example, a normal shock wave, that portion is refracted significantly. Thus, by placing a small aperture or knife edge at the focal point of a second lens, such refracted light is removed, resulting in a dark (or darkened) region in the final image plane.

In this dissertation, the z-shaped schlieren imaging set-up is used [51, 52], as shown schematically in Figure 1-2. Here, the schlieren field of view is optimized to allow complete imaging of the nozzle flow.

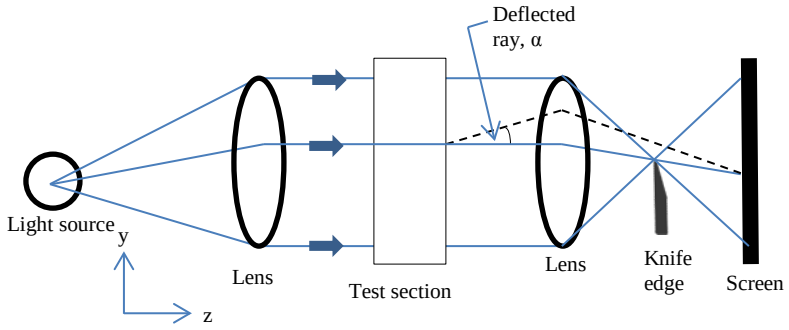

Figure 1-1: Typical schlieren setup [12]

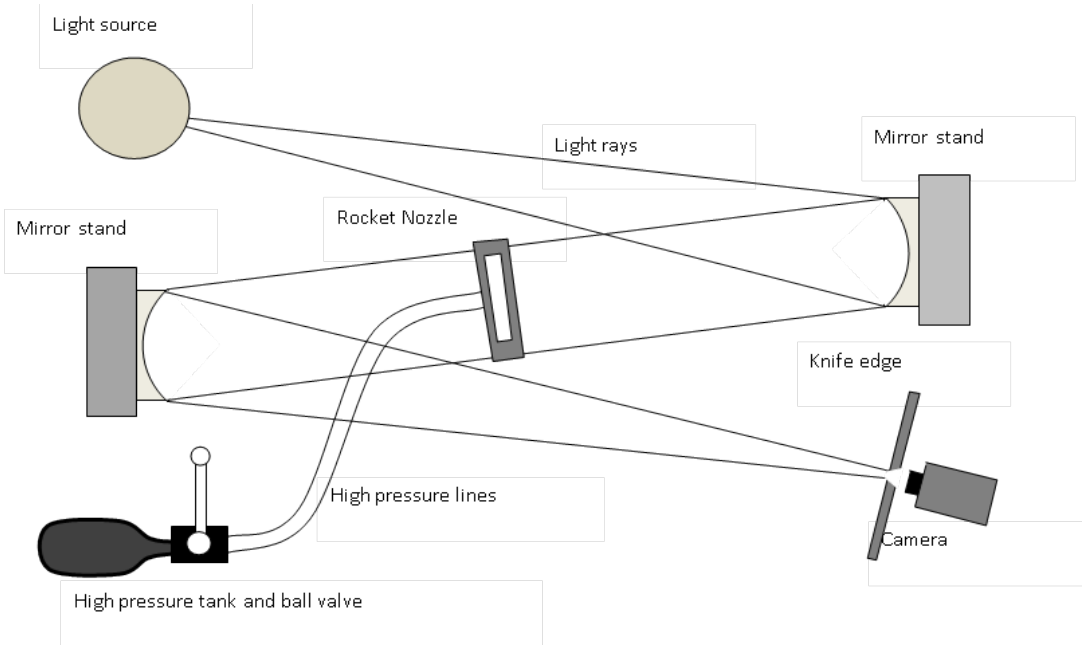

Figure 1-2: Z-type schlieren arrangement used in present experimental system

In the z-type arrangement, a white light source passes through a thin slit, and is then collimated by using two parabolic mirrors. The collimated light passes through the flow test section (a convergent/divergent nozzle in this dissertation) and is then brought into focus. A knife edge at the focal point then blocks most of the refracted light.

In this study, a variation of the standard schlieren method is employed, using instead color schlieren [8, 50]. In this approach, a transparent color film is placed at the focal/aperture point. Thus, regions having the same color in the image plane correspond to beam elements (within the collimated light beam) that have experienced the same integrated, normal-to-beam-direction density gradients.

As a closing remark, it is noted that both calibrated color schlieren (CCS) and background-oriented schlieren (BOS) employ quantitative techniques to evaluate the integrated density gradient. Essentially, CCS and BOS measure the light deflection angle

in two spatial directions, yielding the projected density gradient vector field. Spatial integration using the conjugate gradient method then gives the projected density field [8].

CHAPTER 2: OVERVIEW OF SEMI-QUANTITATIVE SCHLIEREN METHOD

2.1 Introduction

As mentioned, this dissertation proposes a new, approximate diagnostic termed the semi-quantitative schlieren method, for analyzing complex, high-speed flows. This chapter provides an overview of the technique.

Semi-quantitative schlieren (SQS) represents a simple, low-cost approach for determining, in an approximate sense, the velocity, temperature, pressure, Mach number, and density field properties. The method estimates flow field properties by combining schlieren images with simple compressible-flow models of the following:

i) isentropic, steady or unsteady flow, including flow through Prandtl-Meyer expansions,

ii) steady or unsteady flow through oblique and quasi-normal shocks,

iii) shock and expansion wave interactions with other shocks and expansion waves, flow boundaries, and contact discontinuities, and

iv) interactions of weak waves with other weak waves.

The method is classified as semi-quantitative since its accuracy is determined by a number of often poorly controlled or poorly characterized features, including the quality of schlieren images used, the level of uncertainty in upstream boundary conditions, and the degree to which ideal wave interactions with boundary layers, shear layers, and/or contact discontinuities deviate from real wave interactions.

Since similar uncertainties plague even high-fidelity numerical simulations, it becomes apparent that a semi-quantitative approach can offer a number of potential benefits, including use as a precursor, adjunct, or replacement for numerical solutions, use in code validation, and application in fundamental studies of complex compressible flow processes, such as shock/boundary-layer interactions.

In order for the method to be of practical use, it is important that simple, low-cost techniques for generating and imaging high speed flows are available. Tkacik et al. 2010 [1] address this important point, detailing the design and construction of a reliable, safe, inexpensive system for generating high Mach number flows in planar nozzles [1]. Indeed, the same experimental system is used here.

It is emphasized that the proposed diagnostic is not an extension of quantitative schlieren techniques [2, 8, 11]. The latter methods require pixel-level, or equivalent non-digital measurements of light intensity or color hue fields. These measurements can, in turn, be related to flow field properties such as density, temperature, pressure, and/or velocity through detailed consideration of light propagation through density and/or temperature-induced refractive-index gradient fields within the flow.

In traditional quantitative schlieren methods, the refraction index gradient distribution is obtained from the intensity distribution of the schlieren image. This refraction index gradient distribution can be related to distributions of temperature, density, and pressure. Here, in the semi-quantitative schlieren approach, by contrast, the schlieren image is used to *identify or diagnose* regions of the flow for analytical treatment by appropriate theoretical models. These models include, but are not limited to:

i) isentropic ideal gas flow,

ii) flow through normal shocks,

iii) flow through oblique shocks,

iv) flow through Prandtl-Meyer expansions, and

v) flow through wall-generated Mach waves.

2.1.1 Schema of the semi-quantitative schlieren method

In essence, the semi-quantitative schlieren method is based on the following iterative approach in which experimental data and simple theoretical models are combined to arrive at an approximate diagnosis of a given flow. Refer to Figure 2-1.

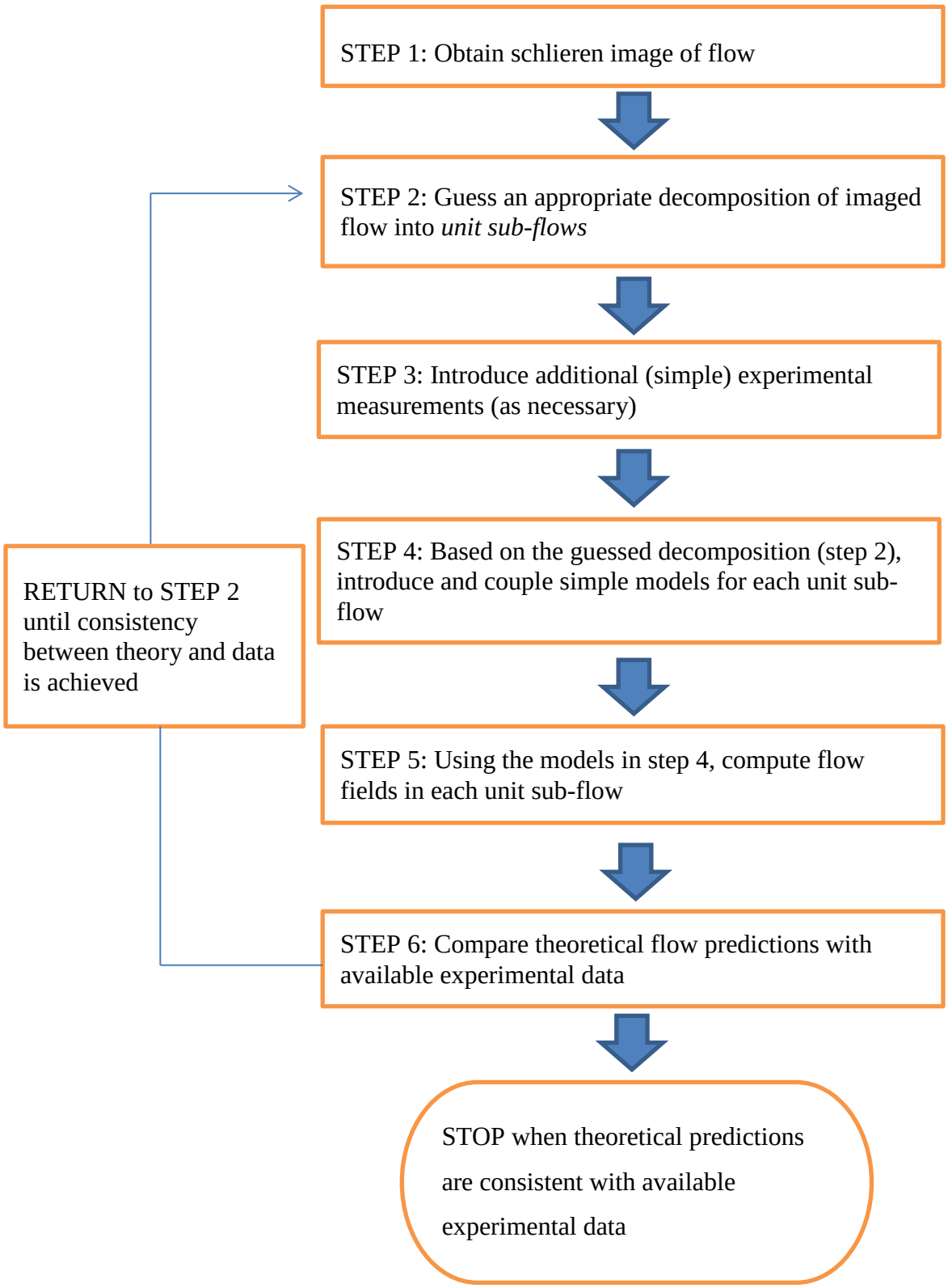

Figure 2-1: Flowchart of the semi-quantitative schlieren method

Consistent with the schematic description shown in Figure 2-1, subsequent chapters will:

i) detail the experimental system used in this study (Chapter 3),

ii) detail the procedures used when initially decomposing a complex flow into simpler unit sub-flows (Chapter 4),

iii) review the theoretical models used to analyze each sub-flow (Chapter 5), and

iv) present the results obtained.

2.2 Objectives of dissertation

The primary objective of this study centers on proposing and developing a new approach, the semi-quantitative schlieren method, for diagnosing complex high-speed flows. This method is proposed as a simple, low-cost alternative to existing experimental and numerical techniques for studying high-speed flows. The technique is not only suitable for a laboratory environment, but can be easily and inexpensively adapted to industrial applications.

CHAPTER 3: EXPERIMENTAL SYSTEM

3.1 Introduction

Prior to discussing the experimental system, three important points are highlighted.

i) Considering the typical approach in which a high-pressure plenum forces a steady or quasi-steady high-speed nozzle flow, costs can be minimized by shrinking the plenum volume, subject to two competing constraints. On one hand, the volume must be small enough to allow affordable pressurization. On the other, the volume must be large enough to provide quasi-steady flow within the test apparatus. In this dissertation, a simple scaling argument is presented to determine the conditions leading to quasi-steady flow conditions.

ii) In a relative sense, it can be argued that designing, fabricating, and setting up a small high-speed flow experiment suitable for simple schlieren imaging is often much simpler than, for example, constructing a high-fidelity numerical simulation. The experimental system employed here was designed, fabricated, and used to obtain experimental schlieren images over a period of 4 weeks [1].

iii) The experimental apparatus is designed to investigate flow physics under high nozzle pressure ratio (NPR) conditions, where NPR is the ratio of plenum to ambient pressures. Outside of a limited number of large, specialized, limited-access facilities, e.g. the Nozzle Test Facility at Marshall Space Flight Center

(Huntsville, Alabama), similar small-scale, high NPR test set-ups do not exist. The cost of building and operating this system is less than $1000 per year.

The approximate nature of the semi-quantitative schlieren approach encourages use of various non-standard approaches when diagnosing a given flow. This important feature is illustrated in three ways:

i) In order to validate model calculations within the flow region adjacent to the nozzle wall, small facets are etched into the wall. These produce weak oblique shocks which, in turn, can be used to either diagnose the near-wall region or validate the near-wall flow model. Since the strength of these artificially induced shocks approaches that of Mach waves, this strategy has minimal effect on the diagnosed flow.

ii) The plenum blow-down process in the apparatus sets the time available for collecting schlieren images. Due to the small size of the system (pressurizing tank volume = 8500 cm^3), blow down is complete in less than one second. Nevertheless, as noted, scaling shows that quasi-steady conditions persist throughout any given run within the nozzle.

iii) One of the long-term objectives of this research program centers on investigating the physical processes underlying side loads in rocket nozzles [53]. An important open question concerns in-nozzle flow mechanisms underlying bifurcation to and from so-called free-shock and restricted-shock flow structures [53]. Presently, no visual data exist concerning this bifurcation.

Although the time resolution of the imaging system is too coarse to resolve such bifurcations (and moreover, the present nozzle does not produce this

bifurcation) due to high repeatability, the highly dynamic evolution of complex, high-speed flows including shock trains can be traced out, via repeated runs. Many essential flow structures which are believed to underlie free-shock separation, and that are predicted by numerical simulation, are observed in this study. Indeed, it appears that this is the first experimental visualization of a rapidly evolving free shock structure within a nozzle [1].

The schlieren technique produces two-dimensional images of a flow field. Thus, a two-dimensional planar nozzle is used in this study. Since planar nozzles are geometrically similar to circular cross-section nozzles, all of the complex flow field features observed in a planar nozzle are also present in an axisymmetric convergent-divergent nozzle. Additionally, the method of characteristics, which plays a central role in this study, is much more easily applied to a two-dimensional planar nozzle.

Although several imaging studies with planar nozzles have been reported, these are primarily limited to flows in which the nozzle pressure ratio lies below the range characteristic of medium to large rockets [1]. This study focuses on flow in high NPR nozzles.

One of the main advantages of the SQS method is the immediate, direct connection between modeling and experiments. The present experimental system is sufficiently small, simple, and inexpensive that new diagnostics, such as additional wall pressure measurements, can be readily introduced, and experiments quickly repeated. Here, flexibility is a major advantage.

As highlighted in Chapter 2, the SQS method requires an iterative approach to the development of the model and the design of the experiment. Essentially, visual

(schlieren) data guides/suggests which models might be appropriate to a given flow region. If it is found that additional experimental data is required in order to complete a model prediction, the experimental system can be easily modified to gather the necessary data. This process of testing models and modifying the experiment continues until a coherent picture of the physical processes underlying a given compressible flow emerges.

3.2 Nozzle experimental set-up

A schematic of the experimental apparatus is shown in Figure 3-1.

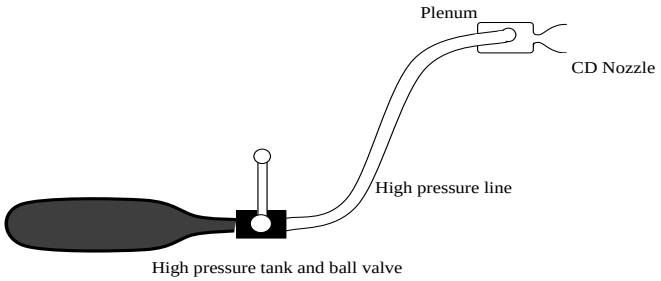

Figure 3-1: Schematic of experimental set-up

Here, a high-pressure tank is connected to the nozzle plenum, which in turn supplies the experimental convergent-divergent nozzle, where the latter is shown in Figures 3-2 and 3-3. (Figure 3-2 shows a detailed schematic of the experimental nozzle, while Figure 3-3 shows photographs.)

The supply tank is designed for safe operation up to pressures of approximately 16.4 MPa (2400 psi). In all experiments, the tank is charged with argon to 15.0 MPa; the corresponding maximum nozzle plenum pressure is 28 bar (407 psi). The tank is connected to the plenum by a hose with an inside diameter of 2.54 cm. A Kulite ETM-375 2500 psi pressure sensor is mounted in the nozzle plenum (not shown), as well as on the high-pressure supply tank.

Four holes are drilled into the side of the nozzle. Two of these are plugged and two are used for placement of two pressure sensors. The sensors are mounted flush with the interior nozzle wall to avoid flow disturbances. The sensors and plugs are sealed in place with Dow 732 multi-purpose sealant.

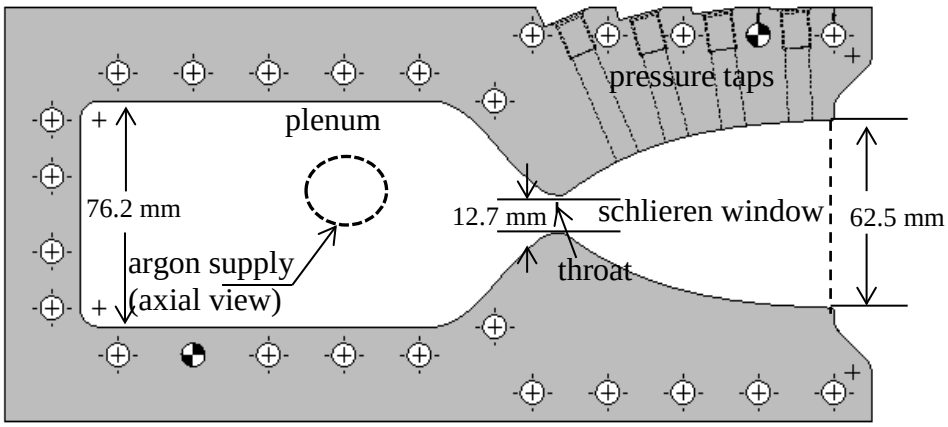

Figure 3-2: Schematic of planar nozzle

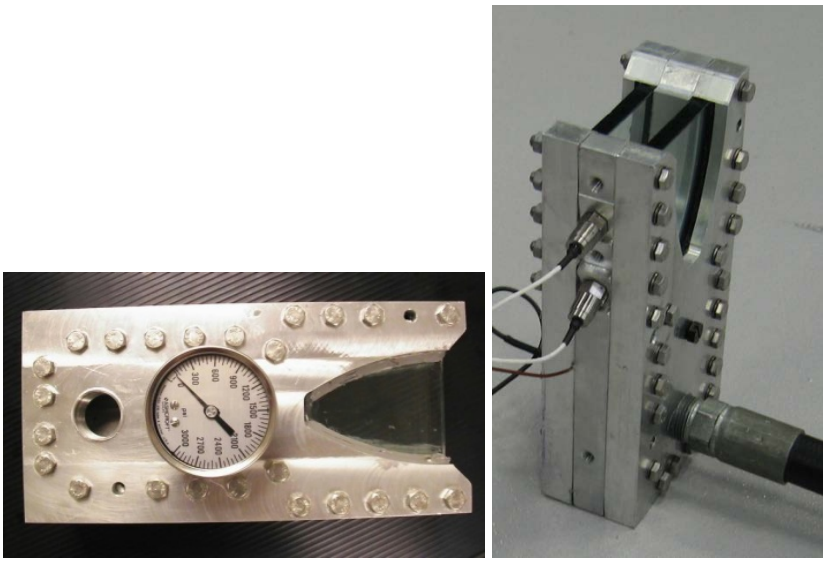

Figure 3-3: Photographs of planar nozzle

The contour of this 5:1 convergent-divergent planar nozzle purposely deviated from an ideal contour in order to produce the complex flow structures observed. The nozzle used in these experiments was designed with a maximum wall turn of 36 degrees in the expansive section, followed by a straightening turn of 36 degrees, yielding axial flow at the exit. For comparison, a thrust-optimized contoured nozzle would require a maximum wall turn in the expansive section of 24 degrees, typically using a centered expansion. Nozzles with long expansive turns could, of course, make do with less.

In order to accommodate relatively high pressures, the viewing windows are fabricated from 1/2-inch-thick tempered glass and sealed to the aluminum nozzle with Dow 732. In order to allow analysis of the near-wall flow field upstream of the boundary layer separation zone [54, 55], small facets are machined, at fixed axial intervals, into the nozzle wall. This technique, pioneered by Prandtl and Meyer [56], allows straightforward, experimentally-based determination of the near-wall Mach number distribution, where the latter is determined via the classical oblique shock equation, or its

weak-disturbance asymptotic form, the simple Mach wave-Mach number relation given by:

$$\sin^{-1}\frac{1}{M} = \mu \qquad \text{Equation 3.1}$$

Here, μ is the Mach wave angle and M is the local Mach number.

3.3 Schlieren set-up

As noted, the color schlieren imaging system uses a typical, z-shaped arrangement [51, 52], as shown in Figure 3-4. Again, the schlieren field of view is optimized to allow complete imaging of the nozzle flow. Pressure signals and corresponding schlieren images are acquired at 1000 Hz using a National Instruments PCI-6024E data logger and a Redlake Motion Xtra HG-XR high-speed digital camera. The lens is a Nikon 24-85 mm zoom f2.8.

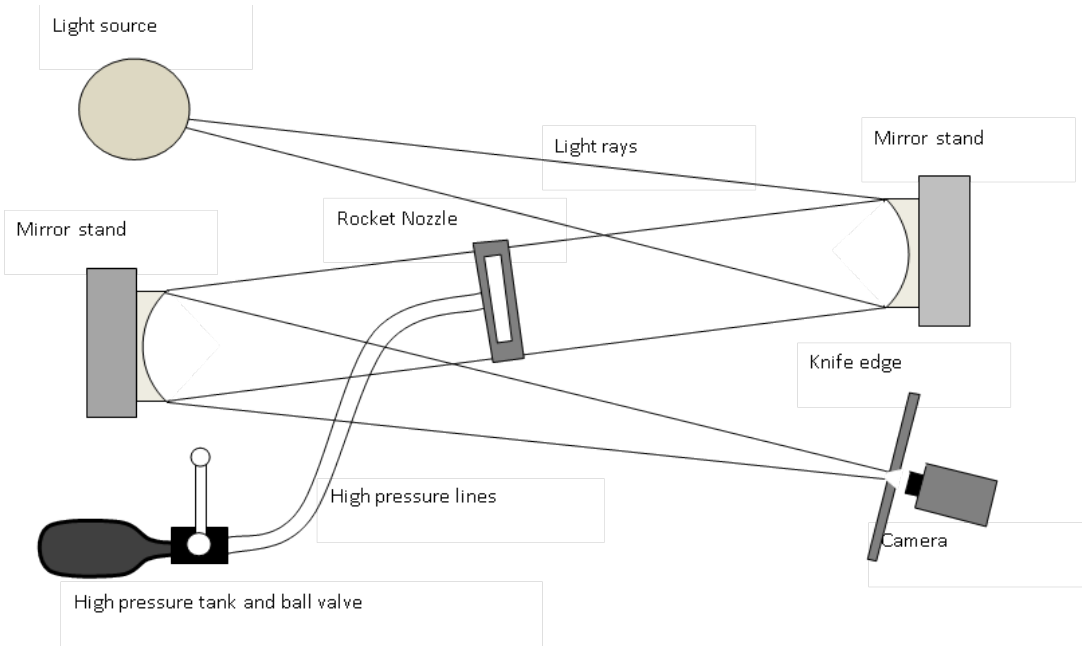

Figure 3-4: Z-type arrangement for schlieren imaging system

3.4 Notes on safety

Since the exhaust from the nozzle is supersonic, care must be taken to prevent anything from entering the gas flow area. The thrust downstream of the upward exhausting nozzle is strong enough that the nozzle must be fastened down to the work surface/lab bench. The pressure test run is initiated by rotating the ball valve 90 degrees as quickly as possible. This ball valve is located between the hose and the argon tank and is rated at 3000 psi. The nozzle is constructed using high-strength tempered glass. As an extra safety measure, the nozzle is placed behind a 2-inch metal shield.

CHAPTER 4: COMPRESSIBLE FLOW MODELS

4.1 Introduction

Analysis of high-speed, non-reacting flow often requires the combined use of the equations of fluid motion, i.e., the Navier-Stokes equations, and the equations of equilibrium (macroscopic) thermodynamics. Depending on the problem under study, and the level of information required, theoretical analysis of high-speed flows typically follows one of three paths

I) Thermodynamic-based analysis is used when spatially coarse descriptions of, e.g., temperature, pressure, density, and/or flow velocity are sufficient. Compressible flow analysis typically emphasizes thermodynamics, often combined with conservation of mass. In this energy-based approach, one applies conservation of energy and mass, for example to fluid particles moving along streamlines or within stream tubes of various dimensions. [Stream tubes are one-inlet, one-outlet control volumes whose lateral surfaces correspond to streamlines. By definition, all mass entering a stream tube (at the inlet) eventually leaves the stream tube at the outlet. Typical stream tubes have small cross-sectional areas, and, in essence, correspond to thick, hybrid streamlines. However, in some internal flow problems, stream tubes, for example, can encompass most of the non-boundary layer internal flow.]

In the thermodynamics-based approach, conservation of energy and mass are augmented with thermodynamic relationships appropriate to the problem at hand. The latter can include, for example, isentropic relations, and an equation of state. In the thermodynamics-based approach, fluid mechanics is typically not treated in any depth.

II) Differential continuum-based analysis is used when detailed information is required, for example, on a velocity distribution, as well as on spatially-varying temperature, pressure, and density fields, one focuses on solving the coupled, differential forms of the conservation of linear momentum, energy, and mass. In this field-based approach, beyond the energy equation, thermodynamics enters peripherally, providing, for example, the equation of state. While the thermodynamics-based approach often allows *analytical solution* of a given high-speed flow problem, the field-based method, more often than not, requires high-level numerical treatments.

III) Modular analysis of unit flow processes is used when the hyperbolic nature of high-speed flow, wherein flow conditions at a given position and time depend on upstream conditions (and in subsonic flow, downstream conditions) lends this class of flows a strong sense of modularity. In particular, it is often possible to analyze a given flow *sequentially* in *modular* fashion, by decomposing the flow into simpler, connected unit flow processes. Examples of unit flow processes that often appear in high-speed flows include:

i) normal shocks,

ii) oblique shocks,

iii) expansion fans,

iv) interacting shocks of the same or opposite families [57],

v) simple and non-simple [57] isentropic flow regions, and

vi) stream tubes.

Importantly, simple models and methods have been developed for analyzing each of these unit flow processes. Thus, as illustrated in this dissertation, it is often possible to decompose a complex high-speed flow into simpler, connected unit flow processes, and to then analyze the flow by sequentially analyzing the unit flows.

This chapter highlights the unit flow process models that are used in diagnosing the complex high-speed flow observed in the experimental nozzle. The next chapter highlights how this flow was decomposed.

4.2 Isentropic flow

As discussed in subsequent chapters, much of the time-varying flow field within the nozzle remains isentropic, or nominally so. Thus, isentropic flow models feature prominently in this analysis. In brief, an isentropic process is one which is adiabatic and reversible. When analyzing compressible flows, we use the isentropic relations from thermodynamics

$$\frac{p_2}{p_1} = \left(\frac{\rho_2}{\rho_1}\right)^{\gamma} = \left(\frac{T_2}{T_1}\right)^{\frac{\gamma}{\gamma-1}} \qquad \text{Equation 4.1}$$

which relate pressure, p, density, ρ, ratio of specific heats, γ, and temperature, T, for an isentropic process. Here, subscripts 1 and 2 represent upstream and downstream conditions, respectively, in a one-dimensional isentropic flow, e.g., within a stream tube. This relationship holds in regions where spatial gradients in temperature and velocity remain small, i.e., where irreversible energy transfer to the molecular scale remains minimal. It should also be noted that this relationship is valid for calorically perfect gases

i.e., ideal gases having constant specific heats. In this study, the assumption of constant specific heat is made.

4.3 Prandtl-Meyer expansions

A Prandtl-Meyer expansion occurs immediately downstream of the nozzle throat over a short axial distance as shown in Figure 4-1.

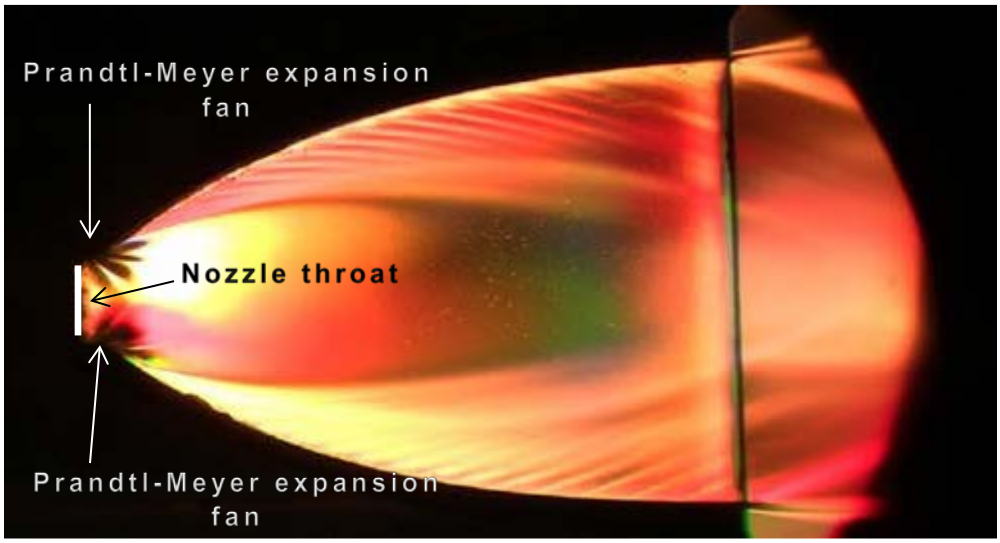

Figure 4-1: Schlieren image of Prandtl-Meyer expansion fan

This expansion fan is a continuous expansion region composed of an infinite number of Mach waves that act to isentropically increase the flow Mach number. Since the expansion happens over a continuous succession of Mach waves, and entropy is constant across each Mach wave, the entire expansion is considered to be isentropic, even for centered expansions with a slope discontinuity in the wall. Analysis of flow through expansion fans relies on the Prandtl-Meyer function, $\nu(M)$, as given by

$$\nu(M) = \sqrt{\frac{\gamma+1}{\gamma-1}}\tan^{-1}\sqrt{\frac{(\gamma-1)(M^2-1)}{(\gamma+1)}} - \tan^{-1}\sqrt{M^2-1} \qquad \text{Equation 4.2}$$

where M is the Mach number and γ is the ratio of specific heats. Essentially, this function relates changes in Mach number to the turning angle of the Prandtl-Meyer flow, where the latter corresponds to flow through an expansion, or flow through a series of infinitesimal, compressive, oblique shocks. This relationship is derived geometrically, and can be found in any compressible flow textbook. See e.g. Anderson [57]. Using this function in conjunction with the nozzle geometry, wall Mach numbers immediately downstream of the throat can be calculated. A Matlab program was written to solve the Prandtl-Meyer function and is given in Appendix A.

4.4 Oblique shocks

As also described in subsequent chapters, weak and non-weak oblique shocks are observed at various locations in, and during various periods of, the time-varying nozzle flow field. Oblique shock waves are analyzed using a well-known equation [57]

$$\tan\theta = \left[\frac{M_1^2(\sin\beta)^2-1}{M_1^2(\gamma+\cos 2\beta)+2}\right] \qquad \text{Equation 4.3}$$

where θ is the wall turning angle, M_1 is the Mach number in front of the shock, β is the oblique shock angle relative to the oncoming free stream, and γ is, again, the ratio of specific heats. As depicted in Figure 4-2, this relationship is geometrically derived using the integral forms of momentum, energy, and mass conservation. Again, see e.g., Anderson [57] for details.

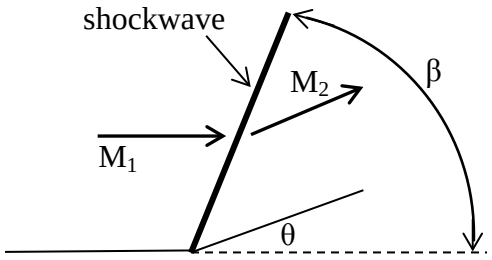

Figure 4-2: Theta-Beta-Mach relation

When analyzing flow through an oblique shock, additional relationships come into play. Specifically, when determining property changes across an oblique shock, well-known normal shock equations [57] can be applied, based on the normal component of the upstream Mach number, M_{n1} , where M_{n1} is given by

$$M_{n1} = M_1 \sin\beta \qquad \text{Equation 4.4}$$

Refer to Figure 4-3. Thus, in terms of M_n, and for calorically perfect gases, changes in density are determined using

$$\frac{\rho_2}{\rho_1} = \frac{(\gamma+1)M_{n1}^2}{(\gamma-1)M_{n1}^2+2} \qquad \text{Equation 4.5}$$

where ρ_2 and ρ_1 are the densities downstream and upstream of the shock, respectively. Likewise, the pressure change across an oblique shock is determined using

$$\frac{p_2}{p_1} = 1 + \frac{2\gamma}{\gamma+1}(M_{n1}^2 - 1) \qquad \text{Equation 4.6}$$

where p_2 and p_1 are the pressures downstream and upstream of the shock, respectively. In addition, the cross-shock static temperature change is obtained using

$$\frac{T_2}{T_1} = \frac{p_2}{p_1}\,\frac{\rho_1}{\rho_2} \qquad \text{Equation 4.7}$$

where T_2 and T_1 are the temperatures downstream and upstream of the shock, respectively.

Finally, the downstream normal component of the Mach number, M_{n2}, follows from

$$M_{n2}^2 = \frac{M_{n1}^2 + [2/(\gamma-1)]}{[2\gamma/(\gamma-1)]M_{n1}^2 - 1}$$ Equation 4.8

Figure 4-3 shows the relationship among M_{n1}, M_{n2}, M_1, and M_2.

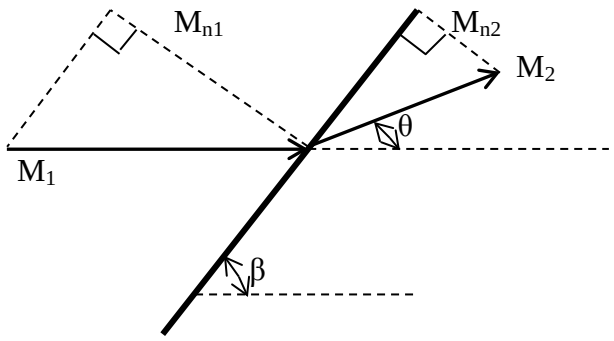

Figure 4-3: Oblique wave shock geometry

For situations where the strength of the pressure wave across an oblique shock approaches zero, the oblique shock wave becomes a Mach wave. In this limit, the angle, θ, approaches zero and the shock angle, β, approaches the Mach angle, μ, where μ is again related to the local Mach number by:

$$\sin^{-1}\frac{1}{M} = \mu$$ Equation 4.9

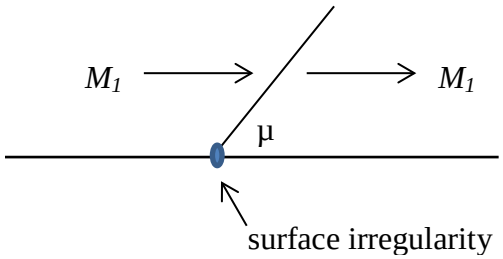

Figure 4-4: Mach angles emanating from wall irregularities

See Figure 4-4. Since the strength, i.e., the pressure increase across a Mach wave, is infinitesimal, the Mach number and flow direction remain unchanged across Mach waves.

4.5 Blow-down model

As a means of gaining physical insight into flow conditions upstream of the nozzle plenum, a model of time-dependent pressure variation within the high pressure holding tank was developed. Unfortunately, for safety reasons, it was not possible to fit the tank with a pressure sensor; thus, the objective centered on comparing theoretical blow-down time, $\tau_{BD,}$ as predicted by the model, against the observed blow-down time.

As noted, the high-pressure tank (volume = 8500 cm^3) is pressurized to approximately 14.4 MPa. The tank is then discharged through a 2.54-cm ID hose into the nozzle plenum, which, in turn, discharges through the nozzle to the surrounding atmosphere. A schematic of the experimental apparatus is shown in Figure 3-1, and a photograph is shown in Figure 4-5.

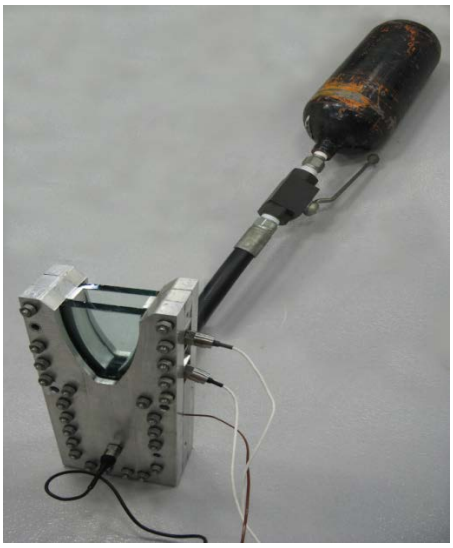

Figure 4-5: Blowdown apparatus

The analysis starts with the unsteady form of the first law of thermodynamics, applied to a fixed control volume. Here, the control volume includes the tank, hose, plenum, and convergent-divergent nozzle. Thus,

$$\dot{Q} + \sum \dot{m}_i(h + \frac{\vec{V}^2}{2} + gZ)_i = \dot{W} + \sum \dot{m}_e(h + \frac{\vec{V}^2}{2} + gZ)_e + \frac{dE}{dt} \qquad \text{Equation 4.10}$$

where the subscripts *i* and *e* refer to properties at the control volume inlet and exit, respectively. Here, $\dot{Q}$ is the rate of heat transfer through the control surface, and $\dot{W}$ is the rate of shaft work done by or on the fluid within the control volume. In addition, *E* denotes the total instantaneous energy, $\int \rho(u + \frac{\vec{V}^2}{2})dV$, within the control volume. Thus, $\frac{dE}{dt}$ represents the time rate of change of this energy. Here, $\dot{m}_e$ and $\dot{m}_i$ are the instantaneous argon mass flow rates at the nozzle exit and inlet, respectively, and *h* and $\vec{V}$ are the corresponding exit/inlet enthalpy and (average) fluid speed.

In the present case, there is no work done on or by the fluid in the control volume (excluding flow work, which is incorporated in the enthalpy terms), and the blow-down

process occurs in such a short time that heat transfer may be neglected. Neglecting potential energy terms, introducing the large-reservoir approximation at the pressure tank, and recognizing that most of the fluid within the control volume lies, at any given instant, within the tank, Equation 4.10 simplifies to

$$\frac{dE}{dt} = -\dot{m}_e\left(h + \frac{\vec{V}^2}{2}\right)_e \qquad \text{Equation 4.11}$$

where E now represents the internal and kinetic energy within the tank alone. Since variations in fluid kinetic energy within the tank are small however, $\frac{\vec{V}^2}{2}$ in Equation 4.11 can be neglected, and dE can be written in finite-difference form as

$$dE = \Delta E = U_2 - U_1 \qquad \text{Equation 4.12}$$

where U represents the total instantaneous internal energy of the fluid within the high pressure tank.

It is assumed that argon, the gas used in the experiment, is calorically perfect. Thus, the specific heat C_v is constant, so that

$$\Delta U = m_{j+1} C_v T_{j+1} - m_j C_v T_j \qquad \text{Equation 4.13}$$

where the subscripts j and j+1 represent the thermodynamic states within the tank at two different times.

The energy equation thus assumes the final form:

$$m_{j+1}C_v T_{j+1} - m_j C_v T_j = \dot{m}_e\left(h + \frac{\vec{V}^2}{2}\right)_e \qquad \text{Equation 4.14}$$

where $\dot{m}_e$ is the instantaneous argon mass flow rate at the nozzle exit, and h and $\vec{V}$ are the corresponding exit enthalpy and (average) fluid speed. The mass flow rate, $\dot{m}$, and velocity, $\vec{V}$, are determined at each time step using the choked-flow assumption at the

nozzle throat. This, in turn, allows calculation of the stagnation temperature, T_{j+1}, of the fluid within the tank at each time step. Additional properties, such as pressure and density are calculated using traditional equations for the compressible, isentropic flow of a calorically perfect gas. Appendix B contains the Matlab computer program written to carry out the finite-difference solution.

Equation 4.14 is solved numerically in time-incremental fashion with a plot of theoretical tank pressure versus time is shown in Figure 4-6. Comparing the predicted blow-down time, τ_{BD}, with those observed experimentally, it is found that $\tau_{BD} \approx 0.65$s, which compares well with the approximate 0.65 to 0.90s times observed experimentally.

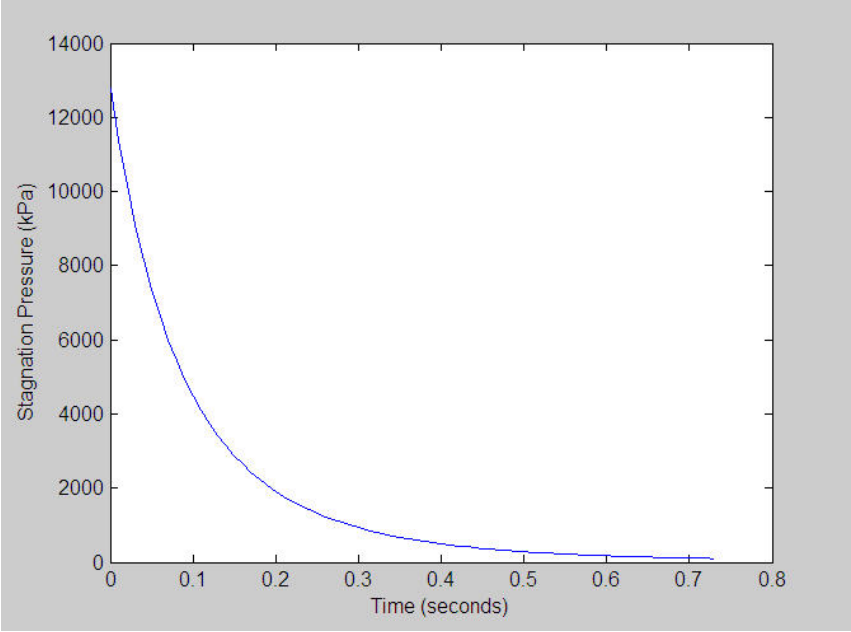

Figure 4-6: Theoretical prediction of stagnation pressure versus time for the tank blow-down process

CHAPTER 5: DECOMPOSITION OF COMPLEX FLOWS INTO SIMPLE SUB-FLOWS

5.1 Introduction

Referring to the schematic description of the semi-quantitative schlieren method in Figure 2-1 in Chapter 2, the third step in this approach centers on decomposing a complex high-speed flow into simpler sub-flows.

In this dissertation, the SQS technique is applied to high-speed flow in a planar nozzle. This case, the first to illustrate the SQS approach, is chosen for a number of reasons:

1. The complexity of the flow, characterized by an internal shock, Prandtl-Meyer expansion fans, near-wall oblique shocks, and boundary layers, all evolving rapidly in time, provides a stringent test bed for the proposed technique.

2. Since the schlieren images provide the experimental foundation upon which diagnostic models are built, the proposed approach is imbued with significant elements of self-correction and self-validation. This important feature is demonstrated by showing that:

   i) theoretical Prandtl-Meyer expansion fans are quantitatively consistent with those observed in schlieren images, and

   ii) theoretical near-wall Mach number fields are quantitatively consistent with image data.

3. Semi-quantitative schlieren approaches are envisioned as inexpensive alternatives (or adjuncts) to traditional, typically expensive experimental diagnostics and/or to time-consuming, technically dense computational flow simulations.

5.2 Experimental schlieren images of the time-dependent nozzle flow

Prior to describing the flow field decomposition, experimental schlieren images of the nozzle blow-down process are presented. The color schlieren images shown in Figures 5--1a through 5-1bb and Appendix C were taken at a rate of 30 frames per second. Selected images obtained at a higher rate of 5000 frames per second, are shown in Chapters 8 and 10.

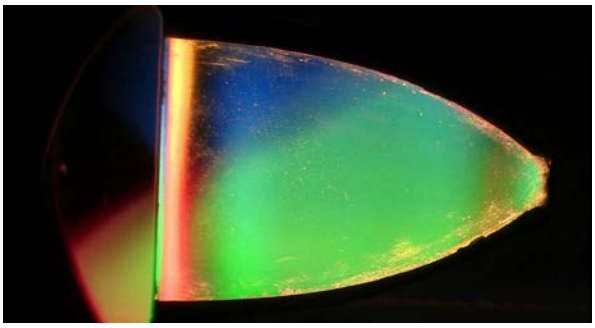

Figure 5-1a: Schlieren image 30fps, t=0.033s

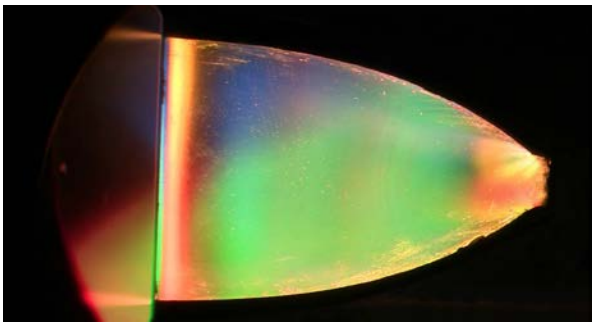

Figure 5-1b: Schlieren image 30fps, t=0.066s

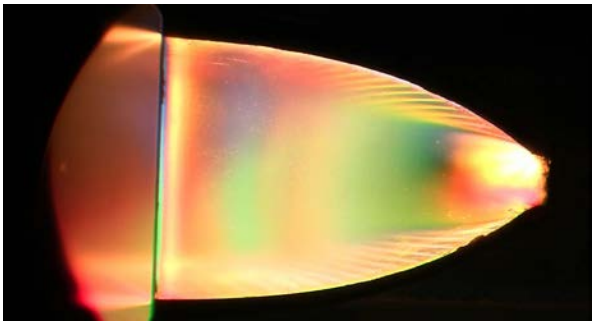

Figure 5-1c: Schlieren image 30fps, t=0.0996s

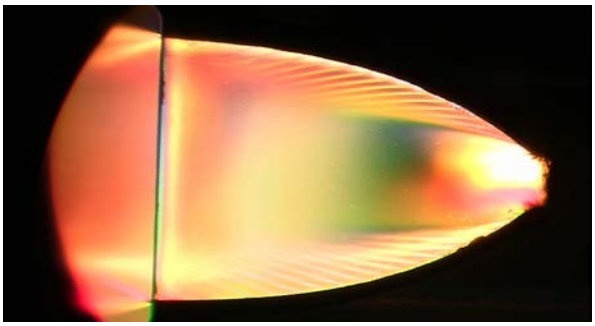

Figure 5-1d: Schlieren image 30fps, t=0.133s

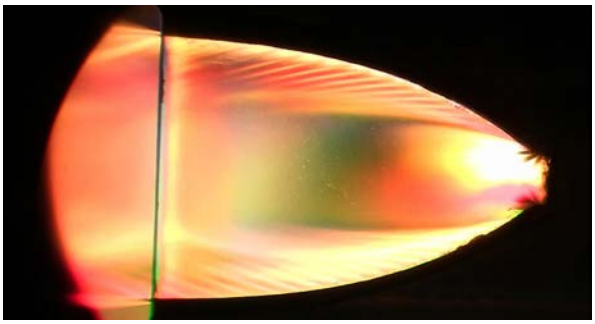

Figure 5-1e: Schlieren image 30fps, t=0.167s

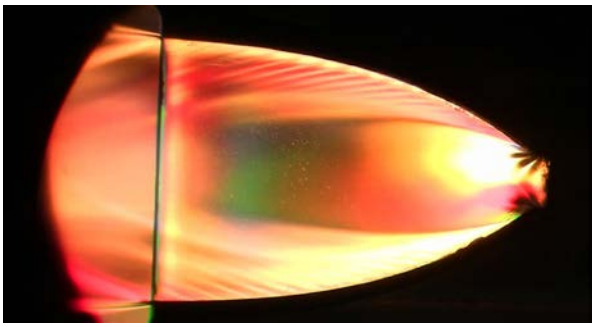

Figure 5-1f: Schlieren image 30fps, t=0.199s

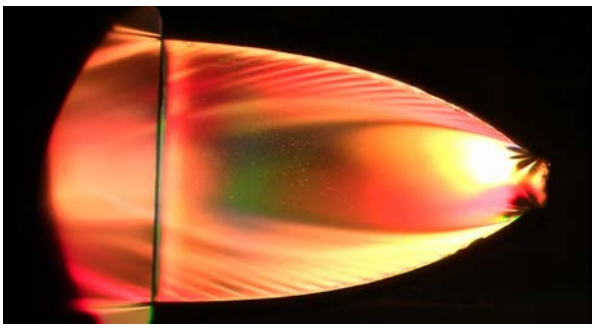

Figure 5-1g: Schlieren image 30fps, t=0.232s

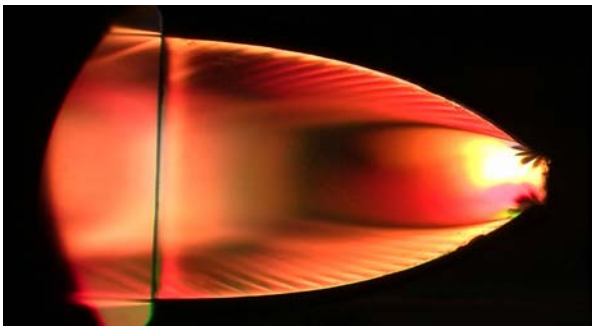

Figure 5-1h: Schlieren image 30fps, t=0.266s

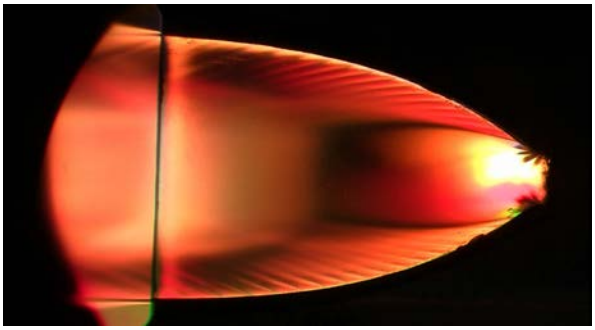

Figure 5-1i: Schlieren image 30fps, t=0.299s

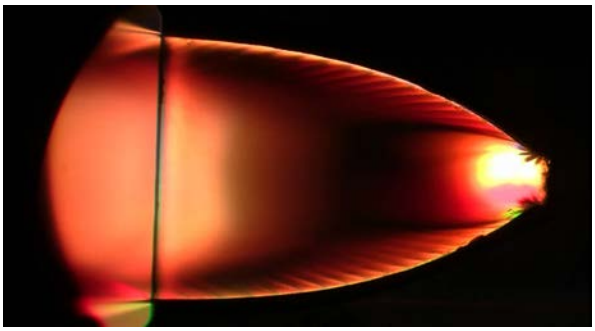

Figure 5-1j: Schlieren image 30fps, t=0.332s

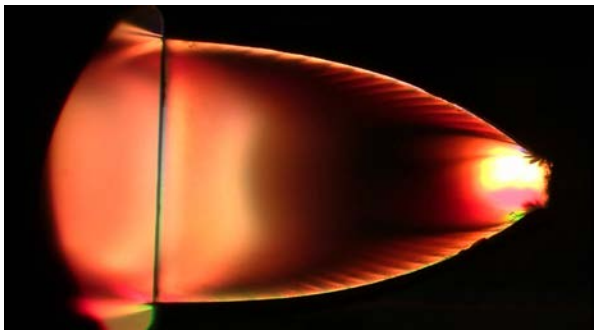

Figure 5-1k: Schlieren image 30fps, t=0.365s

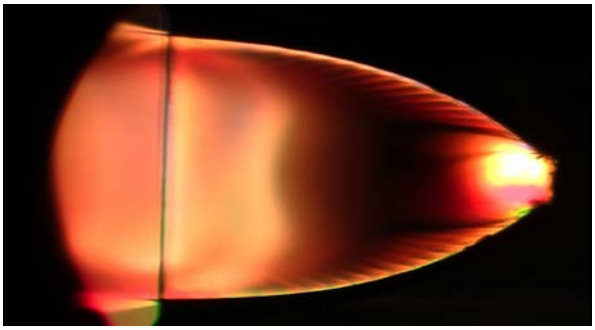

Figure 5-1l: Schlieren image 30fps, t=0.399s

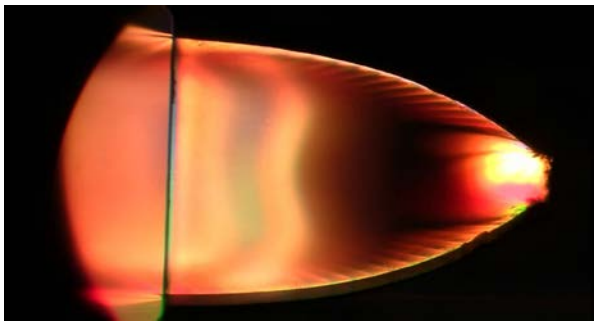

Figure 5-1m: Schlieren image 30fps, t=0.432s

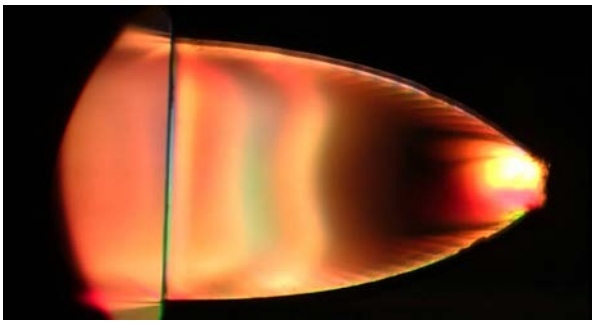

Figure 5-1n: Schlieren image 30fps, t=0.465s

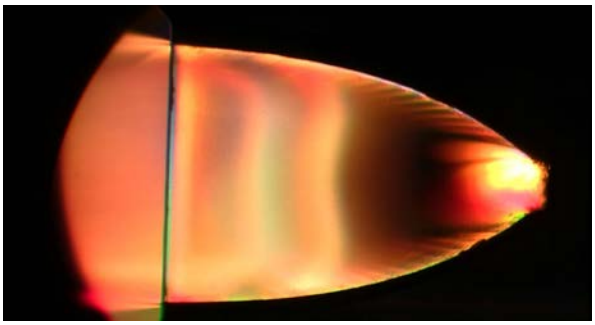

Figure 5-1o: Schlieren image 30fps, t=0.498s

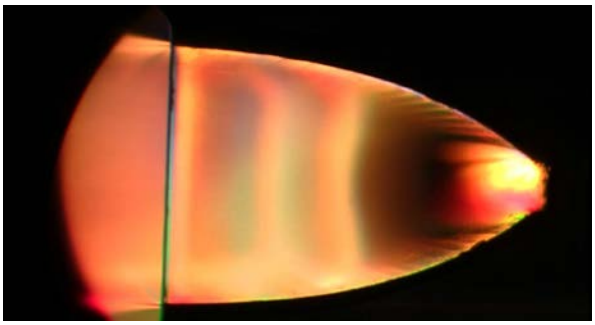

Figure 5-1p: Schlieren image 30fps, t=0.531s

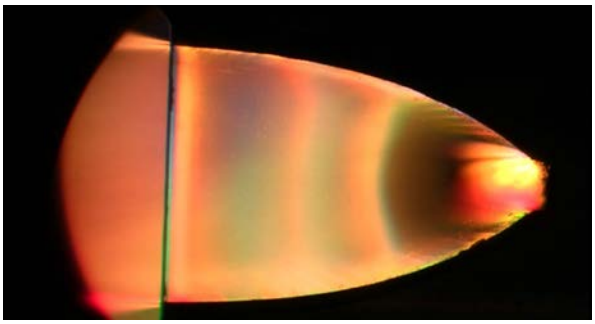

Figure 5-1q: Schlieren image 30fps, t=0.565s

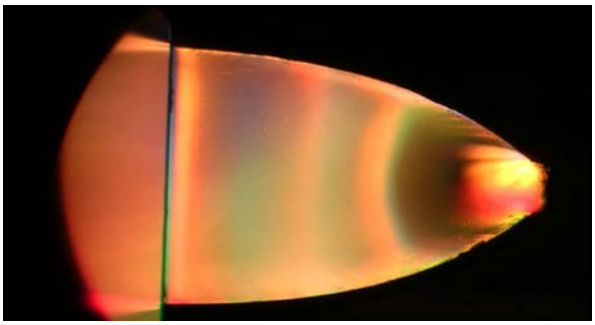

Figure 5-1r: Schlieren image 30fps, t=0.598s

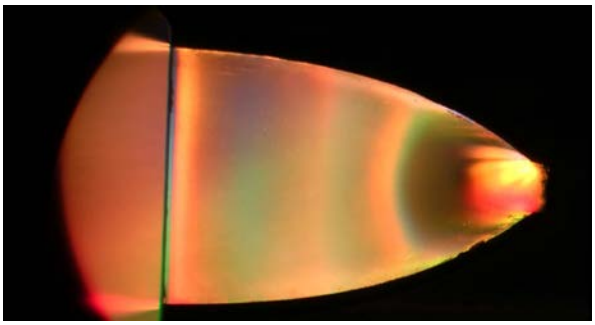

Figure 5-1s: Schlieren image 30fps, t=0.631s

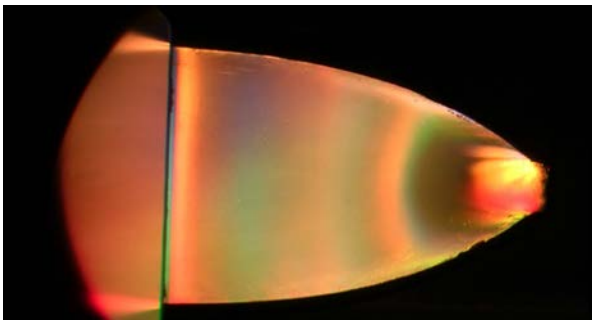

Figure 5-1t: Schlieren image 30fps, t=0.664s

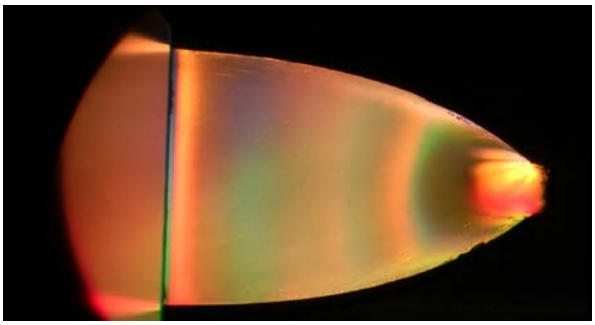

Figure 5-1u: Schlieren image 30fps, t=0.697s

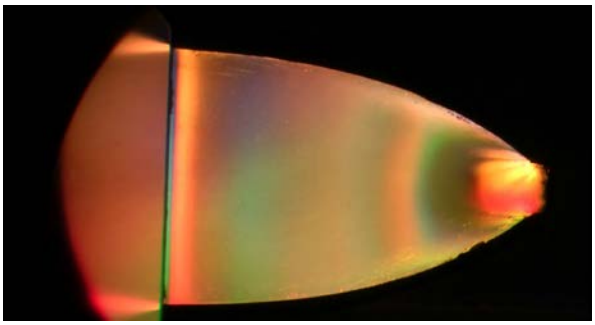

Figure 5-1v: Schlieren image 30fps, t=0.731s

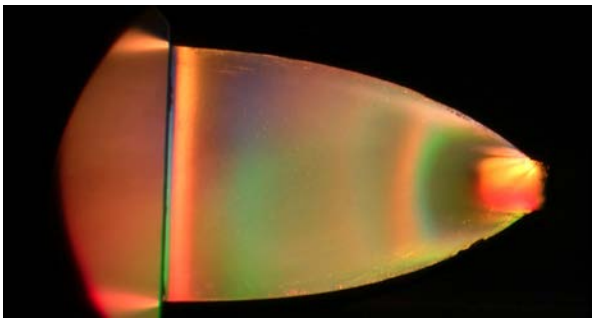

Figure 5-1w: Schlieren image 30fps, t=0.764s

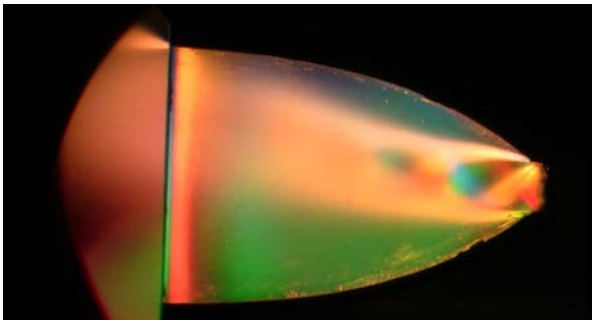

Figure 5-1x: Schlieren image 30fps, t=0.797s

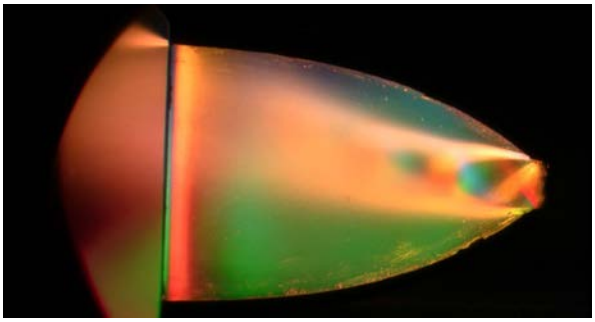

Figure 5-1y: Schlieren image 30fps, t=0.830s

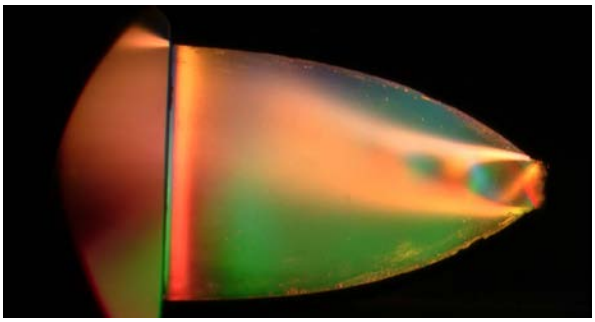

Figure 5-1z: Schlieren image 30fps, t=0.864s

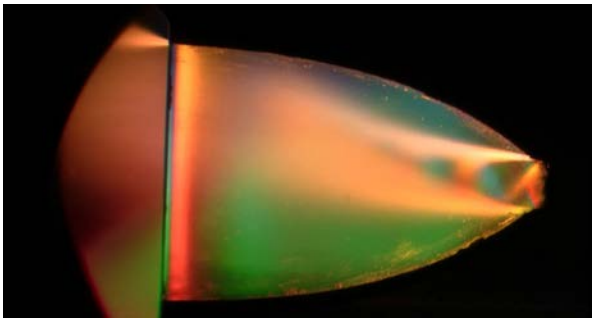

Figure 5-1aa: Schlieren image 30fps, t=0.897s

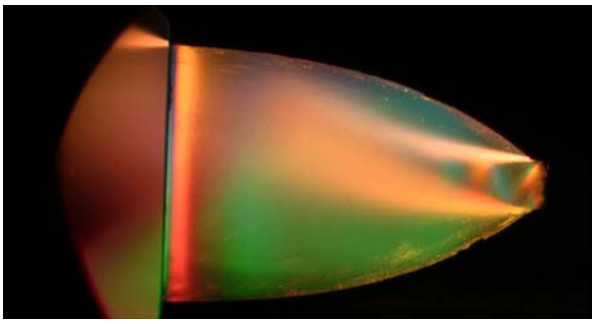

Figure 5-1bb: Schlieren image 30fps, t=0.930s

As discussed in Chapter 8, during the blow-down process, flow within the nozzle is characterized by two distinct regimes:

i) during periods when the nozzle pressure ratio (NPR) is less than approximately 16.8, the nozzle flow field is dominated by two, and sometimes three, parallel, translating, normal shocks, and

ii) when the NPR is greater than approximately 16.8, the in-nozzle flow remains free of normal shocks.

The first regime is termed “shock-train-dominated flow” and the second “shock-train-free flow.”

Detailed discussion of these regimes is deferred to Chapters 8, 9, and 10, and it is simply noted when each appears in Figures 5-1a through 5-1bb.

Thus, during the initial stages of blow-down, when the plenum is being pressurized by the high pressure holding tank and the NPR is thus still relatively small, a double-shock, initiated near the nozzle throat (not shown), traverses the nozzle and is observed exiting the nozzle in Figures 5-1c and 5-1d.

Likewise, during the much slower plenum (and holding tank) depressurization period (see Figure 6-1, Chapter 6), a pair of normal shocks first appear at the nozzle exit as observed in Figure 5-1k. As the NPR continues to decay, the shock pair then moves upstream within the nozzle, as shown in Figures 5-1k through 5-1w.

The two periods of shock-train-dominated flow are separated by an extended period of shock-train-free flow, as shown in Figures 5-1d through 5-1j. [Note, while a barrel-shaped internal shock is apparent in these latter images, further analysis by the SQS approach shows that the shock is quite weak. See Chapter 8. Thus, since the moving pair of normal shocks that constitute the shock-train are not present, this regime could also be characterized as shock-free flow.]

Importantly, nozzle flow structure remains nominally invariant during the period of shock-train-free flow; refer again to Figures 5-1d through 5-1j. Thus, as an initial test bed for developing and validating the semi-quantitative schlieren method, the SQS diagnosis is focused on the shock-train-free flow field. The next subsection describes the initial and final SQS decomposition of this flow regime.

5.3 Initial SQS flow field decomposition

As noted in the SQS flow chart in Chapter 2, one must *guess*, based on available schlieren image data, an initial decomposition.

Here, the initially guessed decomposition of the shock-train-free flow is shown in Figure 5-2, where the initial guess is based on the following assumptions:

a) The near-wall region is assumed to be dominated by *oblique shocks*, produced by facets in the nozzle wall.

b) It is assumed that the interaction of these oblique shocks produced a near-horizontal internal shock.

c) A strong normal shock is assumed to exist downstream of opposing horizontal internal shocks.

d) The region interior to the opposing horizontal internal shocks and upstream of the normal shock is assumed to be isentropic.

[Note, throughout this dissertation, the “near-wall flow region” refers to the region exterior to the internal, barrel-shaped shock.]

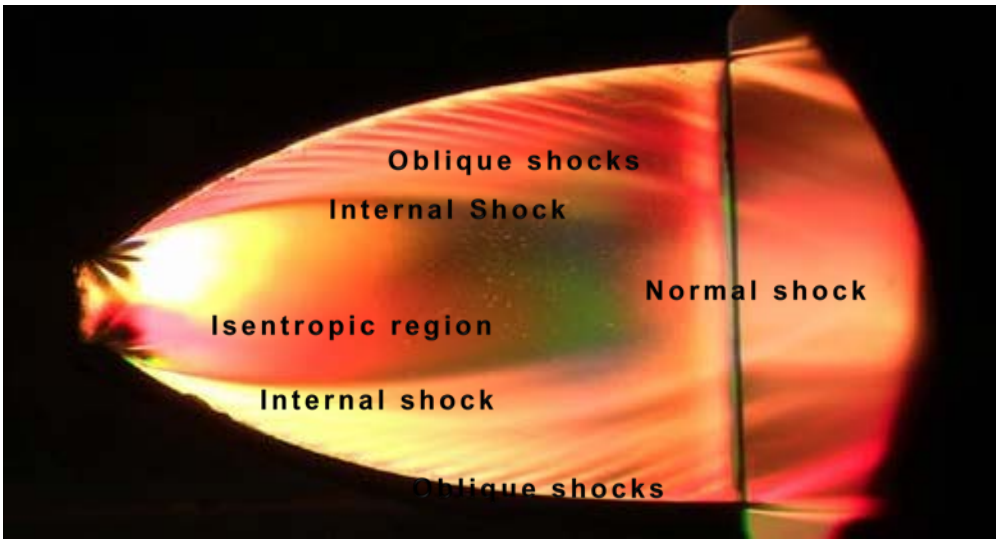

Figure 5-2: Initial flow decomposition guess

As outlined in the SQS flowchart in Chapter 2, once an initial decomposition is specified, a comparison must be made between theoretical predictions obtained from the initial guess with available experimental data. Here, three pieces of experimental data were initially available:

i) observed near-wall wave angles produced by nozzle wall facets,

ii) observed expansion fans immediately downstream of the nozzle throat, and

iii) time-varying plenum pressure measurements.

As detailed in Chapter 6, subsequent analyses, as well as introduction of limited wall pressure measurements, eventually lead to revision of the initial decomposition, as described immediately below.

5.4 Final SQS flow field decomposition

The final flow field decomposition is shown in Figure 5-3.

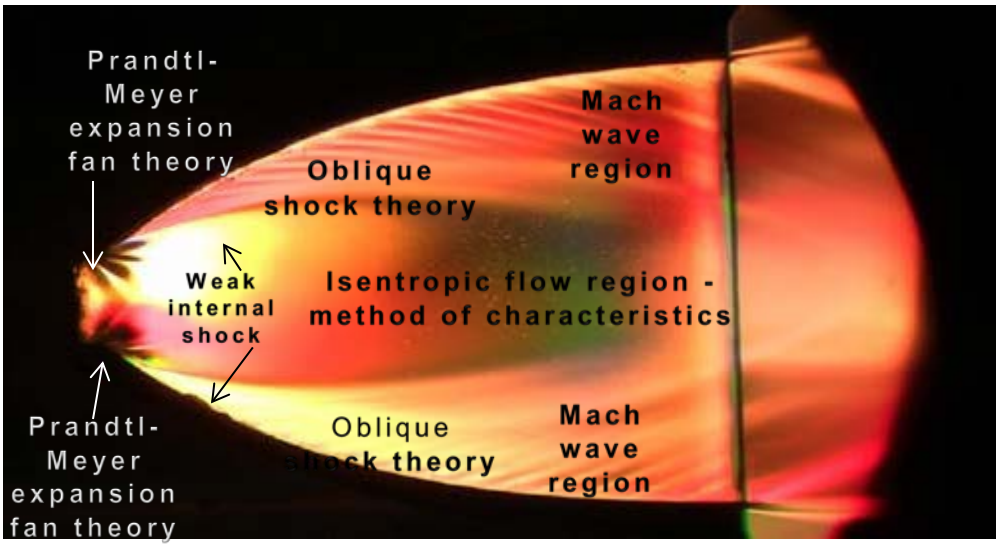

Figure 5-3: Final SQS flow field decomposition

Here, the region of flow considered purely isentropic extends from the Mach line at the throat, through the Prandtl-Meyer expansion fan, to the downstream normal shock, and is bounded radially by the barrel-shaped internal shock.

Comparing the initial and final decompositions, Figures 5-2 and 5-3, respectively, it is observed that only one significant modification was necessary: the near-wall region where oblique shock theory applies was found to extend only over the first third of the nozzle wall. Over the remaining two-thirds, much better agreement between theory and experiment was obtained by assuming this region to be isentropic; thus, near-wall waves, in reality, correspond to Mach waves. See Chapter 6.

CHAPTER 6: SEMI-QUANTITATIVE SCHLIEREN DIAGNOSIS OF QUASI-STEADY SHOCK-TRAIN-FREE FLOW IN A PLANAR NOZZLE – PART I

6.1 Introduction

This chapter presents the results of various analyses that were used to diagnose the quasi-steady flow observed in a single schlieren frame during shock-train-free flow. The imaged flow field shown in Figures 5-2 and 5-3 is representative of those observed during this period. As noted, the nozzle blow-down process is characterized by two distinct flow regimes. The first, which is observed at nozzle pressure ratios (NPR) less than approximately 16.8, is dominated by the presence of a multi-shock shock train. This regime occurs twice, first during the initial period of plenum pressurization when the NPR is increasing from 1 to approximately 16.8, and subsequently during the latter stages of the blow-down process when NPR decays from approximately 16.8 back to 1. Refer to Figure 6-1. The shock-train-dominated flow regime is analyzed in Chapter 9.

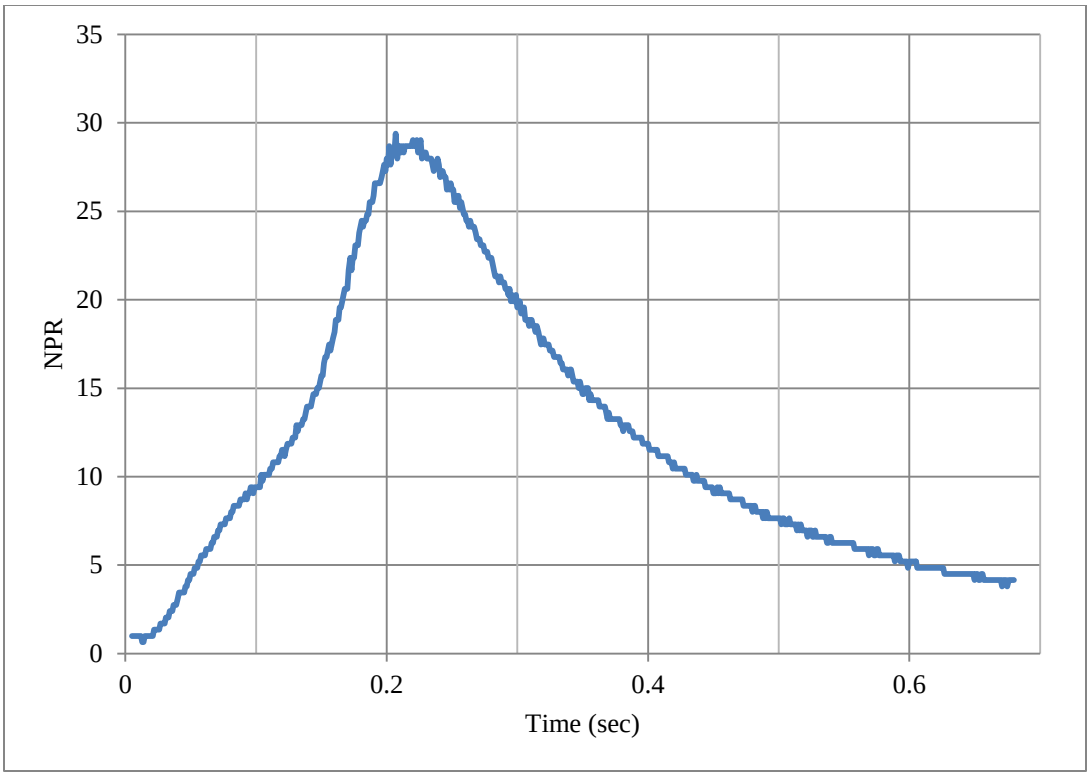

Figure 6-1: Nozzle pressure ratio (NPR) as a function of time (from experiment)

The second regime, which this chapter and the next analyzes, and which exists when the NPR is greater than approximately 16.8, is characterized by the *absence* of shock trains.

The analysis of the shock-train-free flow is organized as follows:

1) First, the expansive region immediately downstream of the nozzle throat is diagnosed (Section 6.2). Based on schlieren image data and the assumption that this region behaves as a Prandtl-Meyer expansion, experimentally observed expansion waves are compared to those computed using the standard Prandtl-Meyer model.
2) The flow region adjacent the nozzle wall, downstream of the Prandtl-Meyer expansion and extending to the exit, is next diagnosed; see Section 6.3. Here, several

different theoretical models are examined, with the objective of obtaining a model that reasonably predicts observed near-wall wave angles.

3) Analysis of the near-wall region in Section 6.3 reveals that, contrary to an initial visual assessment, waves emanating from the wall are almost certainly (isentropic) Mach waves, rather than (non-isentropic) oblique shocks. Thus, since the region interior to the weak internal shock is almost certainly isentropic, a method of characteristics analysis of both the interior, strongly isentropic region and the near-wall nearly-isentropic region is undertaken. This analysis comprises Part II of the SQS diagnosis and is presented in Chapter 7.

6.2 Prandtl-Meyer expansion region

As indicated in Figure 6-2, expansion fans appear to emanate from the outwardly expanding nozzle wall, immediately downstream of the nozzle exit. Introducing the

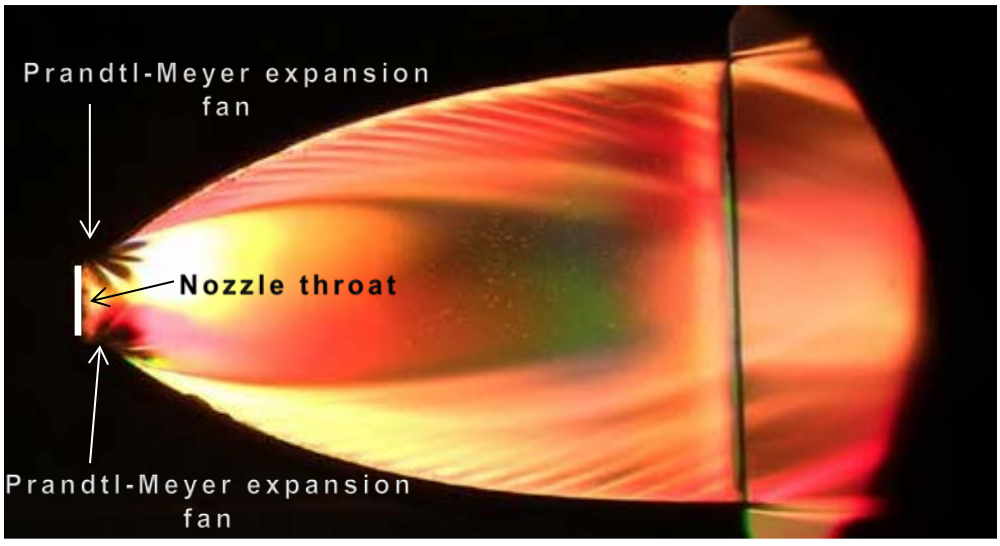

Figure 6-2: Schlieren image of Prandtl-Meyer expansion fan

assumption that flow between the throat and wall expansion is isentropic, and based on the apparent existence of expansion fans in the schlieren images, it can be assumed that these regions behave as Prandtl-Meyer expansions.

Thus, using the known wall geometry, which provides the local wall angle, θ, and assuming a sonic condition at the throat (i.e., $M_{throat} = 1$), local Mach wave angles can be sequentially computed:

i) First, and as outlined in Chapter 4, the local change in the Prandtl-Meyer function, $\upsilon(M)$, is computed, where:

$$\upsilon(M_{i+1}) - \upsilon(M_i) = \Delta\theta_i \qquad \text{Equation 6.1}$$

and where $\upsilon(M)$ is related to the local Mach number via Equation 4.2. Here, M_i and M_{i+1} denote the Mach numbers at wall nodes i and i+1 along the wall expansion, and $\Delta\theta_i$ is the known change in wall angle between nodes. See Figure 6-3.

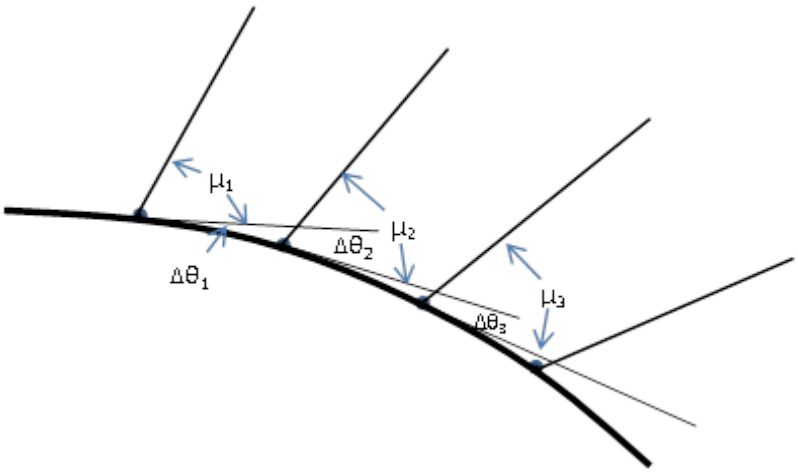

Figure 6-3: Prandtl-Meyer expansion fan

ii) Second, the angle of the local Mach wave, μ_i, given by

$$\sin^{-1}\frac{1}{Mi} = \mu_i \qquad \text{Equation 6.2}$$

can be determined given M_i.

Using this procedure leads to the results shown in Figure 6-4.

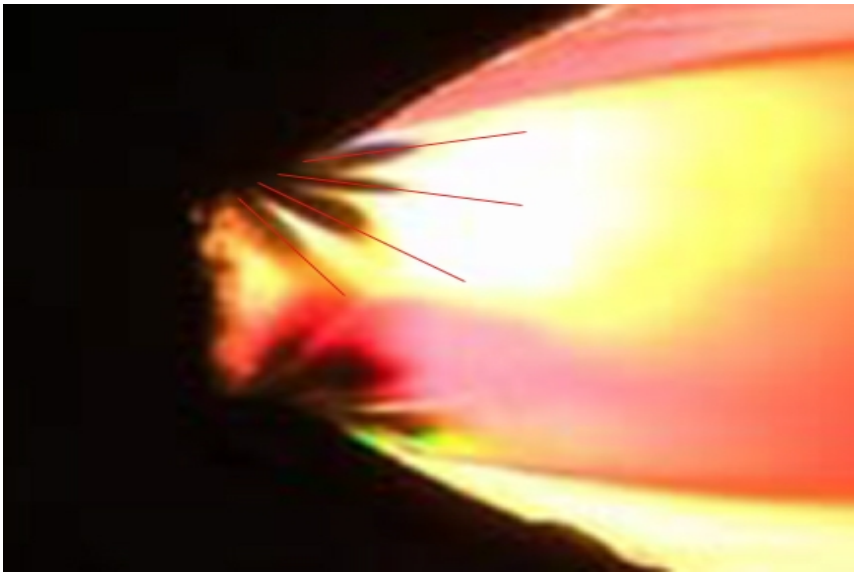

Figure 6-4: Schlieren image of Prandtl-Meyer expansion fan [Theoretical Mach waves are shown by red line segments.]

As shown, the Prandtl-Meyer model provides a reasonable description of the observed experimental expansion fans. Physically, this provides strong support for the assumption that flow over the wall expansion is nominally isentropic.

6.3 Near-wall flow region

An initial assessment of the schlieren image of the near-wall region, Figure 6-5, clearly suggests that facets in the nozzle wall produce oblique shocks. In order to test the validity of this initial assessment, a calculation was performed in which oblique shock

wave angles were determined sequentially, starting from the first wall facet, and proceeding downstream.

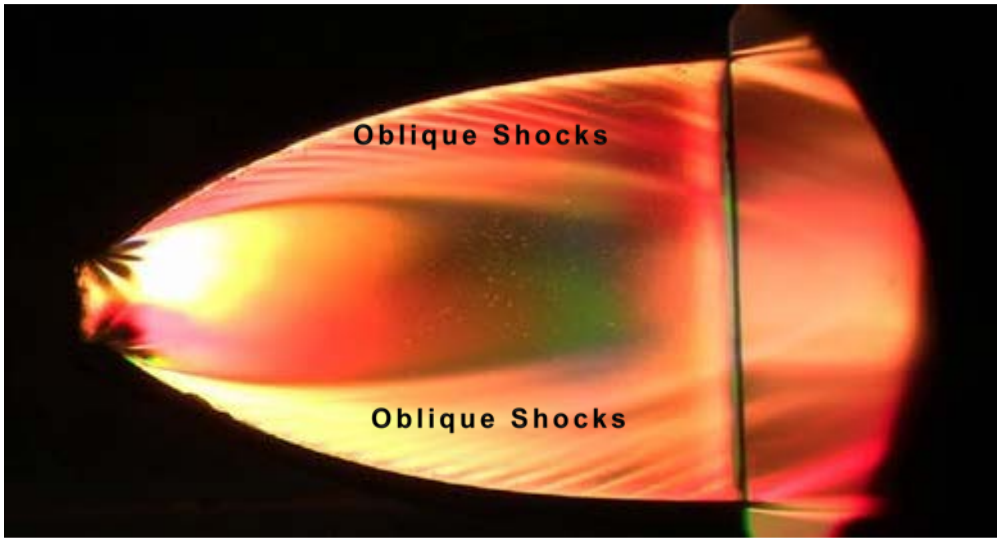

Figure 6-5: Schlieren image with oblique shocks

Using the oblique shock model outlined in Chapter 4, the following strategy was employed:

i) Starting at wall facet 1, the final computed Mach number at the exit from the Prandtl-Meyer fan (downstream of the nozzle throat) was used as the upstream Mach number at the corresponding first oblique shock.

ii) Using the known wall deflection (at the facet) and the known upstream Mach number, Equation 4-3 was then used to determine the corresponding oblique shock angle, β.

iii) Given β and the upstream Mach number, the downstream Mach number was then computed via oblique shock relations in Chapter 4.

iv) Using the downstream Mach number computed in step iii) as the *upstream* Mach number for the next downstream oblique shock, steps i) through iii) were then repeated at all subsequent downstream wall facets.

The results of this calculation are shown in Figure 6-6.

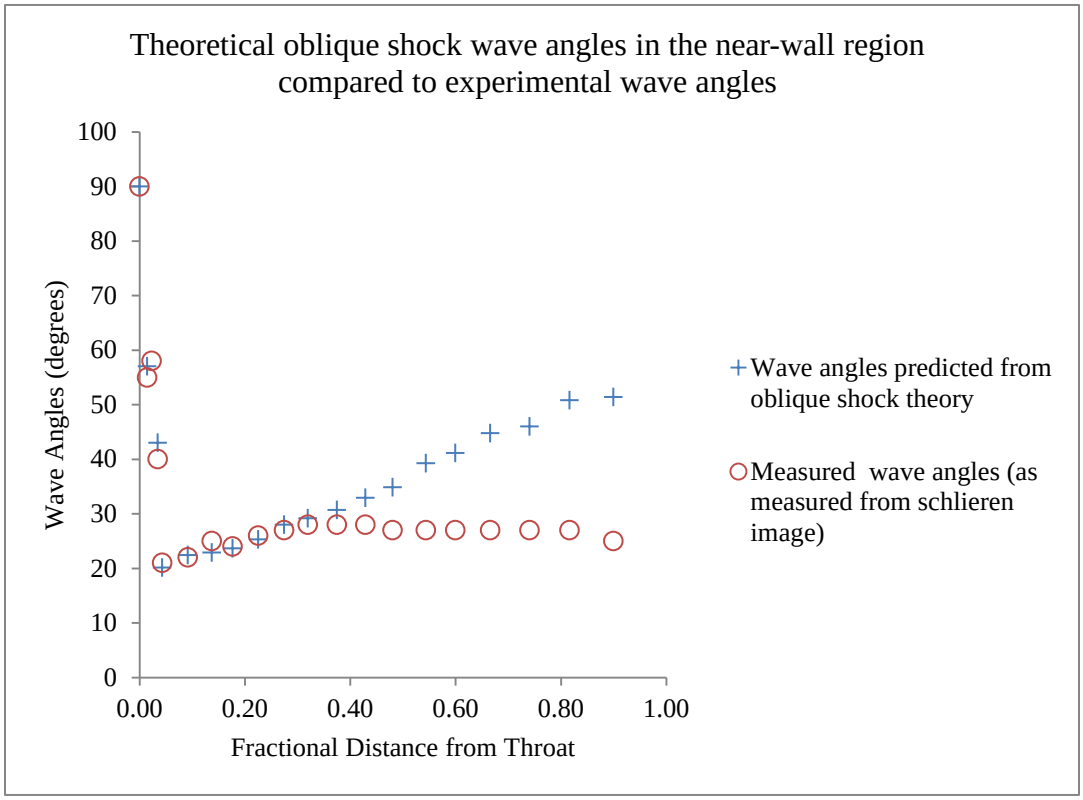

Figure 6-6: Wave angles versus fractional distance from throat

As indicated by Figure 6-6, the assumption that near-wall waves are oblique shocks appears to be quite reasonable, at least over approximately the first third of the nozzle wall. However, over the remaining two-thirds, increasing divergence between

predicted and observed wave angles clearly indicates that the oblique shock model no longer applies.

In order to address the discrepancy between theory and experiment over $0.3 \leq x/L \leq 0.9$ (where x and L are axial position and nozzle length, respectively), attention is focused on wall curvature over this range of wall positions. Specifically, close inspection shows that wall curvature is significant over $0 \leq x/L \leq 0.3$, while the wall becomes almost flat for $x/L \geq 0.30$. Thus, the oblique shock model is modified as follows:

i) Over $0 \leq x/L \leq 0.30$, it is assumed that changes in wall angle at each wall facet are large enough to produce an oblique shock.

ii) For $x/L \geq 0.30$, it is assumed that wall curvature approaches zero so that each facet creates a Mach wave.

The latter assumption means that over the near-wall region, $x/L \geq 0.30$, the (non-boundary layer) flow behaves approximately as a uniform, constant Mach number flow over a flat plate. Thus, for $x/L \geq 0.3$, wave angles remain constant, having a magnitude equal to that downstream of the last oblique shock at $x/L \approx 0.3$.

Using this modified model leads to the results shown in Figure 6-7.

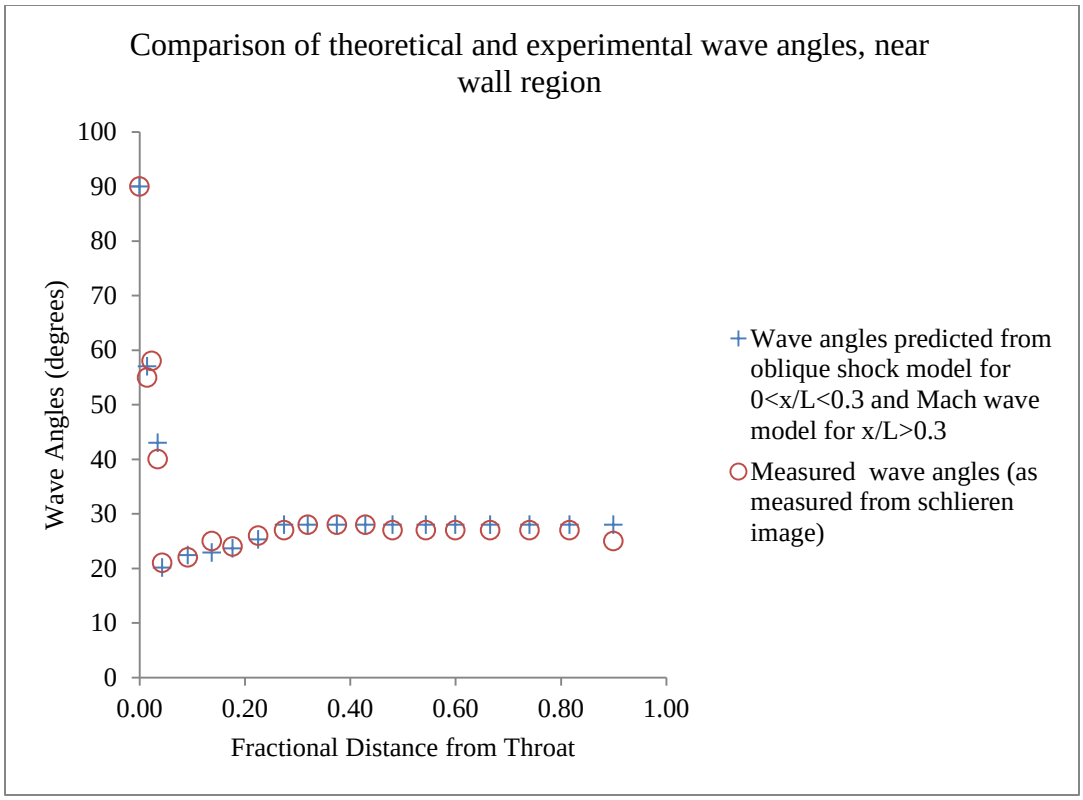

Figure 6-7: Wave angles versus fractional distance from throat (modified model)

In closing this subsection, it is noted that the assumption that Mach waves, rather than oblique shocks, are created over $x/L \geq 0.30$ is fully consistent with the two subsequent analyses presented in Sections 6.4 and 6.5 below.

6.4 Isentropic stream tube model applied to near-wall region

In this section, the idea that the near-wall flow region between $0 \leq x/L \leq 0.9$ is *approximately isentropic* is tested. This important notion is suggested by the analyses and results described in section 6.3. Specifically,

i) over $x/L \geq 0.3$, it was found that wall facets apparently generate Mach waves, while

ii) over $0 \leq x/L \leq 0.3$, due to small changes in wall slope, it appears reasonable to expect that facet-generated waves, likewise, generate either weak oblique shocks or Mach waves.

Importantly, from a physical and diagnostic standpoint, if the nature of the near-wall waves over $0 \leq x/L \leq 0.9$ can be unambiguously determined, then an appropriate compressible flow model can be used to determine field properties, such as *P, T, h, M,* and ρ, within this region.

In order to address this question, three tasks were undertaken:

i) Pressure taps were installed at two points, $x/L = 0.25$ and $x/L = 0.62$, along the nozzle wall.

ii) A third theoretical model of flow in the near-wall region was introduced, which took advantage of both wall pressure and schlieren image data.

iii) A new set of nozzle blow-down experiments were carried out.

The new model focuses on flow in stream tubes that extend from the nozzle plenum to locations along the nozzle wall. See Figure 6-8

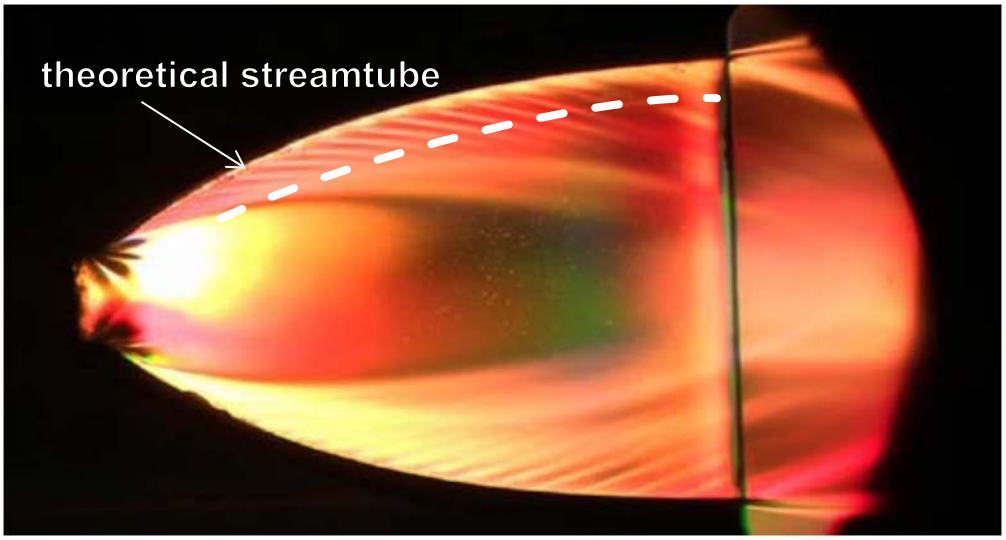

Figure 6-8: Theoretical streamtube

The model assumes that flow within any given near-wall stream tube remains isentropic and steady. Thus, near-wall pressure at any position *x*, *P(x)*, can be related to the local near-wall Mach number, *M(x)* via

$$\frac{P_o}{P(x)} = [1 + \left(\frac{\gamma-1}{2}\right) M^2(x)]^{\frac{\gamma}{\gamma-1}} \qquad \text{Equation 6.3}$$

where P_o is the measured plenum pressure, and $\gamma = c_p/c_v$, is the ratio of gas specific heats.

Thus, measured pressures at x/L = 0.25 and x/L = 0.62, $P(0.25)$ and $P(0.62)$, when combined with measured P_o in Equation 6.3, provide a theoretical prediction of associated near-wall Mach numbers, $M(0.25)$ and $M(0.62)$; corresponding theoretical Mach wave angles, $\mu(0.25)$ and $\mu(0.62)$, then follow from:

$$\mu(x) = sin^{-1}\frac{1}{M(x)} \qquad \text{Equation 6.4}$$

The results of this analysis are presented in Figure 6-9.

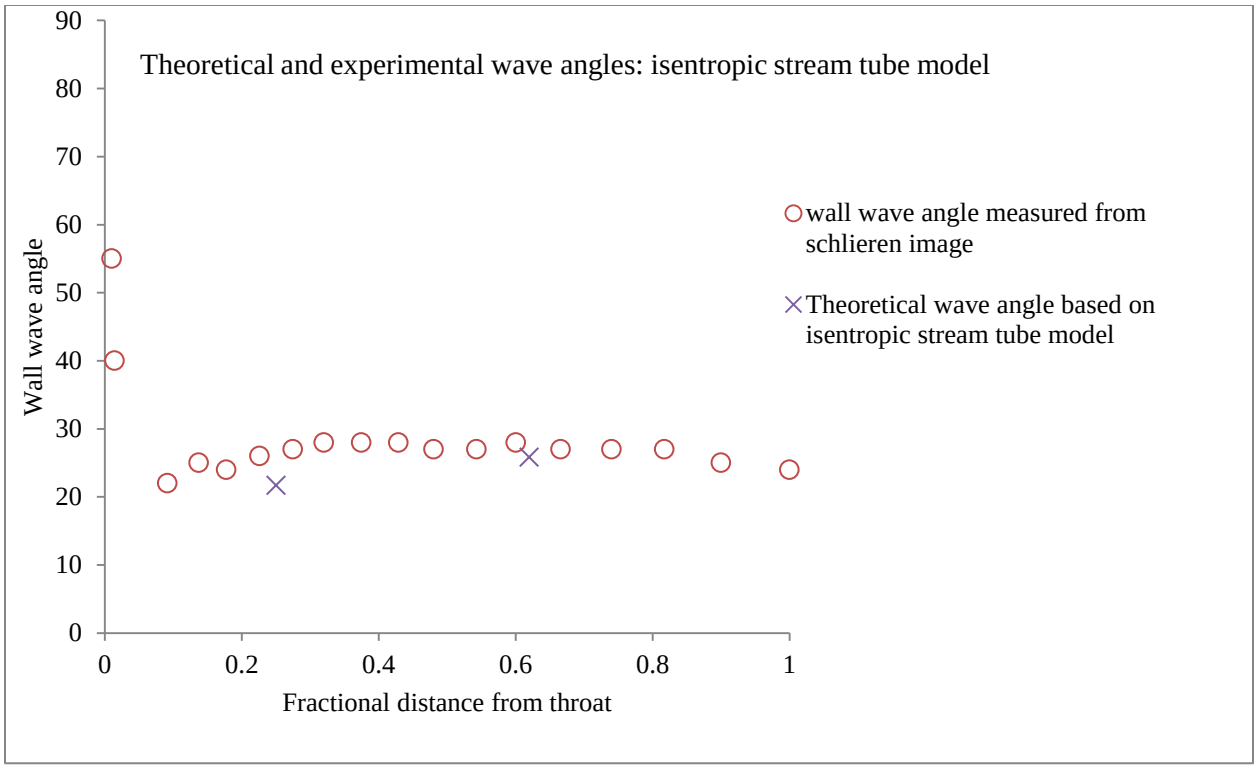

Figure 6-9: Stream tube model of wall wave angles versus fractional distance from throat

Importantly, from a diagnostic standpoint, there are now two consistent results that strongly indicate the physical nature of the near-wall flow region:

i) The close agreement between theoretical and experimental wave angles (at x/L = 0.25 and x/L = 0.62) shown in Figure 6.9 indicates that the flow from the plenum to these locations is nominally isentropic. This, in turn, suggests that the near-wall facet-induced waves between $0 \leq x/L \leq 0.3$ are, in fact, weak oblique shocks or Mach waves.

ii) Likewise, the close agreement between theoretical and experimental wave angles shown in Figure 6-7 is consistent with nominally isentropic flow. Certainly, the close agreement between computed isentropic Mach angles and observed wave

angles over $0.3 \leq x/L \leq 0.9$ provides strong, direct evidence of isentropic flow over this portion of the near-wall region.

6.5 SQS determination of near-wall temperature, pressure, and density fields

Having obtained strong evidence that the near-wall flow region is nominally isentropic, observed near-wall wave angles, $\mu_{exp}(x)$, obtained via schlieren imaging can now be combined with standard isentropic flow relations to obtain near-wall temperature, density, and pressure fields:

$$\frac{T_o}{T(x)} = 1 + (\frac{\gamma-1}{2})M^2(x) \qquad \text{Equation 6.5}$$

$$\frac{\rho_o}{\rho(x)} = [1 + \left(\frac{\gamma-1}{2}\right)M^2(x)]^{\frac{1}{\gamma-1}} \qquad \text{Equation 6.6}$$

$$\frac{P_o}{P(x)} = [1 + \left(\frac{\gamma-1}{2}\right)M^2(x)]^{\frac{\gamma}{\gamma-1}} \qquad \text{Equation 6.7}$$

[Note, again, that $M(x)$ above follows from the measured Mach angle, $\mu_{exp}(x)$, Equation 6.4.]

CHAPTER 7: SEMI-QUANTITATIVE SCHLIEREN DIAGNOSIS OF SHOCK-TRAIN-FREE FLOW REGIME, PART II – METHOD OF CHARACTERISTICS CALCULATION

Part I demonstrated that during the period of shock-train-free flow, most of the nozzle flow field is likely isentropic or nearly so. This chapter thus uses a method of characteristics analysis to obtain an approximate diagnosis of the entire shock-train-free flow.

7.1 Introduction: An overview of the method of characteristics

Although developed by mathematicians for the solution of partial differential equations, Prandtl himself was involved in the first successful implementation of the method of characteristics (MOC) for the analysis of two-dimensional supersonic flows [57]. The method presented herein is essentially the same: Determine lines in the flow field (characteristics) along which property derivatives are undefined or discontinuous and on which the partial differential equations which describe the flow reduce to ordinary differential equations. For two-dimensional flow, these can be solved using a step-by-step algebraic procedure, yielding properties for the entire flow field.

For two-dimensional, irrotational, supersonic flow, the equations describing conservation of mass, linear momentum, and energy result in well-known partial differential equations that govern the flow field. See, for example, Anderson [57]. Every point in the flow field has passing through it two lines, along which fluid properties are continuous, but across which property derivatives with respect to position are

discontinuous or undefined. These lines are called characteristics and, in fact, correspond to Mach waves. For flow proceeding left to right, the characteristic with a positive slope relative to the flow direction is termed left-running, and the one with negative slope is termed right-running. Referring to Figure 7-1, these slopes can be expressed relative to any chosen coordinate system:

$$\left.\frac{dy}{dx}\right|_{char} = \tan(\theta \pm \mu) \qquad \text{Equation 7.1}$$

where θ is the angle that the flow makes with a positive (horizontal) x axis, and μ is the Mach angle measured on either side of the flow direction.

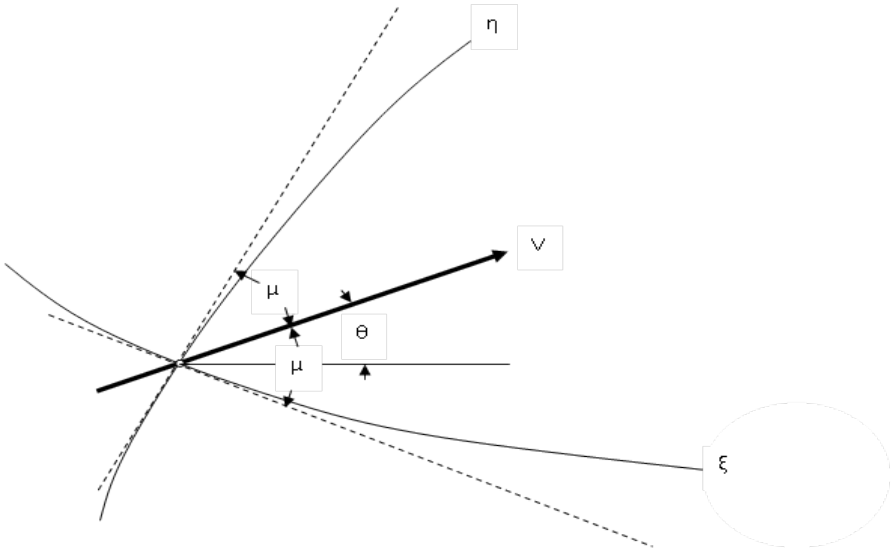

Figure 7-1: Slopes of characteristics

The system of coupled equations governing continuity (conservation of mass), momentum, and energy can be manipulated into compatibility relations, given by

$$d\theta = \pm\sqrt{M^2 - 1}\frac{dV}{V} \qquad \text{Equation 7.2}$$

where the negative sign refers to right-running characteristics and the positive to left-running characteristics. Recognizing this as the equation which is integrated to give the Prandtl-Meyer function, υ, allows the compatibility equations to be written in *algebraic* form as [57]

$$\theta + \upsilon = constant \qquad \text{Equation 7.3}$$

for right-running characteristics and

$$\theta - \upsilon = constant \qquad \text{Equation 7.4}$$

for left-running characteristics. The specific implementation of these equations is detailed below.

The implementation presented herein is numerical rather than graphical (as was favored by Prandtl). A Matlab program, listed in Appendix D, was written to perform necessary calculations.

7.2 Implementation of MOC calculation

The method of characteristics can be used to analyze steady, compressible, high speed flows that are calorically perfect and isentropic. Analysis is typically limited to two-dimensional flow. Here, assume that the flow is two-dimensional, consistent with use of a planar nozzle in experiments.

Figure 7-2 shows three general interior nodes in the characteristic grid. Parent nodes 1 and 2 can be used to obtain property values at child node 3, without regard to node locations. The characteristic grid for two-dimensional, isentropic, supersonic flow is constructed as follows.

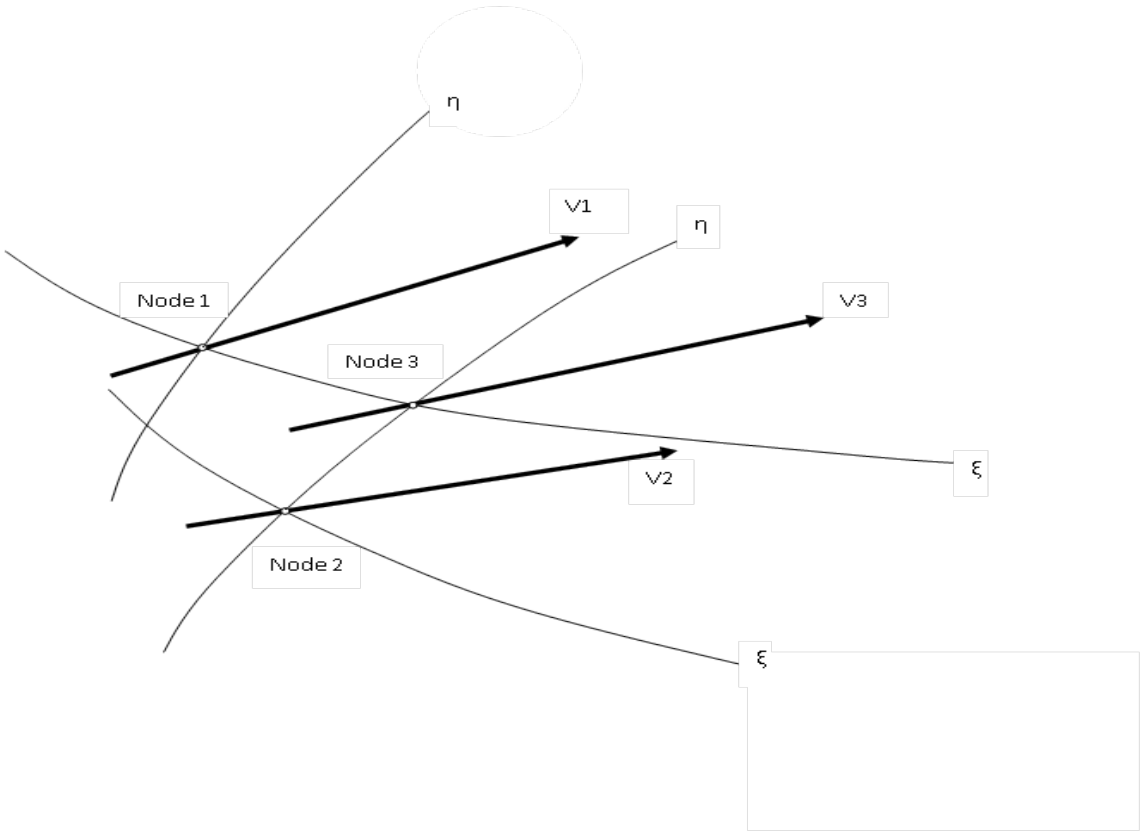

Figure 7-2: MOC grid

Along a right-running characteristic, ξ, the sum of the Prandtl-Meyer function value, υ, and the flow angle, θ, measured from the horizontal is constant, or

$$\upsilon + \theta = Q = constant \qquad \text{Equation 7.5}$$

Along a left-running characteristic, η,

$$\upsilon - \theta = R = constant. \qquad \text{Equation 7.6}$$

Therefore, for a left-running characteristic,

$$\upsilon_2 - \theta_2 = \upsilon_3 - \theta_3, \qquad \text{Equation 7.7}$$

while for a right-running characteristic,

$$\upsilon_1 + \theta_1 = \upsilon_3 + \theta_3 \qquad \text{Equation 7.8}$$

Combining these then gives

$$\upsilon_3 = \frac{\upsilon_1+\upsilon_2}{2} + \frac{\theta_1+\theta_2}{2}$$ Equation 7.9

By this method, the flow direction, θ, and Prandtl-Meyer function, υ, at any interior node – where the latter is located by the intersection of upstream left-running and right-running characteristics - are uniquely determined. Knowing the value of the Prandtl-Meyer function, the local Mach number can then be found from the former:

$$\nu(M) = \sqrt{\frac{\gamma+1}{\gamma-1}}\tan^{-1}\sqrt{\frac{(\gamma-1)(M^2-1)}{(\gamma+1)}} - \tan^{-1}\sqrt{M^2-1}$$ Equation 7.10

Since this equation is implicit in Mach number, a Matlab program was written to solve it. See Appendix A for the program listing.

For the case of a node lying on the centerline of the nozzle, only a right-running characteristic is needed to determine properties. This results from using only the upper half of the nozzle contour, where symmetry about the centerline is assumed. See Figure 7-3.

For this case flow angle $\theta_3 = 0$, (from symmetry) so from Equation 7.8,

$$\upsilon_3 = \upsilon_1 + \theta_1$$ Equation 7.11

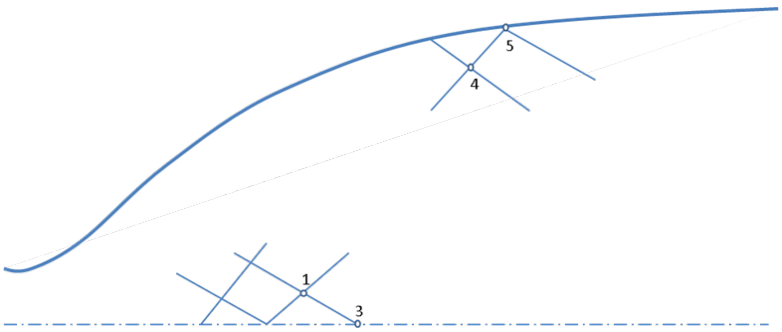

Figure 7-3: MOC symmetry

For the case of a wall node (Figure 7-3), only a left-running characteristic is needed for property determination; thus, from Equation 7.7,

$$\upsilon_5 = \upsilon_4 - \theta_4 + \theta_5 \qquad \text{Equation 7.12}$$

where θ_5 is the wall node known from the nozzle geometry. As discussed next, unlike the interior node and centerline node, for which properties can be determined independent of node location, the location of wall node 5 is needed in order to know flow direction.

The more difficult aspect of the MOC calculation involves determination of node locations. Referring to Figure 7-5, the slope of the right-running characteristic from node 1 relative to the horizontal is given by

$$\left|\frac{dy}{dx}\right| = \tan(\theta_1 - \mu_1) = m_1 \qquad \text{Equation 7.13}$$

Similarly, the slope of the left-running characteristic is given by

$$\left|\frac{dy}{dx}\right| = \tan(\theta_2 + \mu_2) = m_2 \qquad \text{Equation 7.14}$$

As is described in some textbooks [57], the characteristics could, in principle, be assumed straight, and the location of node 3 could then be taken as their point of intersection. Since the characteristics are actually curved, a better location of node 3 is determined by using the average of the slopes at the parent and child nodes, and then by finding the intersection of the resulting lines for the right-running characteristics from node 1 and the left-running characteristics from node 2. The average slopes, $\overline{m}$, can then be found as

$$\overline{m_1} = tan\left(\frac{\theta_1+\theta_3}{2} - \frac{\mu_1+\mu_3}{2}\right) = \frac{y_3-y_1}{x_3-x_1} \qquad \text{Equation 7.15}$$

and

$$\overline{m_2} = tan\left(\frac{\theta_2+\theta_3}{2} - \frac{\mu_2+\mu_3}{2}\right) = \frac{y_3-y_2}{x_3-x_2} \qquad \text{Equation 7.16}$$

For the interior nodes, these can be solved algebraically to yield the location of child node 3 (Figure 7-2) in terms of the locations of parent nodes 1 and 2.

$$x_3 = \frac{y_2 - y_1 + \overline{m_1}x_1 - \overline{m_2}x_2}{\overline{m_1} - \overline{m_2}} \qquad \text{Equation 7.17}$$

and

$$y_3 = \frac{\overline{m_2}(\overline{m_1}x_1 - y_1) + \overline{m_1}(y_2 - \overline{m_2}x_2)}{\overline{m_1} - \overline{m_2}} \qquad \text{Equation 7.18}$$

For the special case of a centerline node (Figure 7-3), where $\theta_3 = 0$,

$$\overline{m_1} = \tan\left(\frac{\theta_1}{2} - \frac{\mu_1 + \mu_3}{2}\right) \qquad \text{Equation 7.19}$$

and

$$x_3 = x_1 - \frac{y_1}{\overline{m_1}} \qquad \text{Equation 7.20}$$

and, by definition, $y_3 = 0$.

7.3 A new predictor-corrector method for flow near walls

The biggest challenge arises for nodes lying on the nozzle contour (wall nodes). Fluid properties cannot be determined for a wall node without knowing its location, since flow direction must be parallel to the wall. The wall slope (flow direction) can only be determined by knowing the axial location (x-coordinate) and by substituting this into the derivative of a third-order curve fit of the nozzle contour. The previously described averaging method for the slope of left-running characteristics cannot be used since flow properties at the wall are unknown since the node location is unspecified. This conundrum (properties cannot be found without location and location cannot be found without properties) was solved by development of a new predictor-corrector method for the determination of the position of a wall node. Referring to Figure 7-3, a trial wall location was found by using the un-averaged value of the characteristic slope, given by

$$m_4 = \tan(\theta_4 + \mu_4), \qquad \text{Equation 7.21}$$

and then by finding the intersection of this line with the third-order curve representing the wall contour

$$y = 0.0187x^3 - 0.2029x^2 + 0.7825x + 0.19 \qquad \text{Equation 7.22}$$

Note that the corresponding wall slope, *m*, is given by

$$m = \frac{dy}{dx} = 0.0561x^2 - 0.4058x + 0.7825 \qquad \text{Equation 7.23}$$

Thus,

$$m_4 = \tan(\theta_4 + \mu_4) = \frac{y_5 - y_4}{x_5 - x_4} \qquad \text{Equation 7.24}$$

and

$$y_5 = y_4 + m_4(x_5 - x_2) \qquad \text{Equation 7.25}$$

The x-coordinate of the intersection of the characteristics and the curved wall is then found by equating Equations 7.22 and 7.25 and by solving the resulting cubic equation. Since this had to be done for every wall node, the solution was incorporated in the MOC Matlab program given in Appendix C. The resulting trial (predictor) value of x (the axial location of the wall node) was used in Equation 7.23 to obtain the trial wall slope. With this wall slope representing the flow direction, Equations 7.12 and 7.10 finally give flow properties.

With properties now known at both parent and child nodes, nodes 4 and 5 respectively, the usual averaging method is used to obtain a new characteristic slope and a new, better, wall node location, along with associated properties.

7.4 Further model details and assumptions

The schlieren image of the shock-train-free flow analyzed is again shown in Figure 7-4.

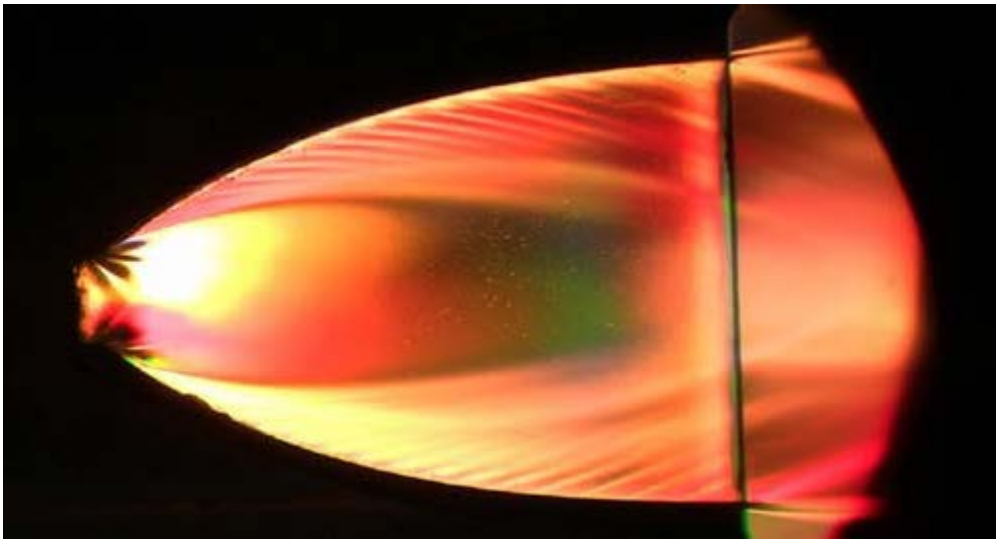

Figure 7-4: Image for analysis

To start the MOC calculation, a Mach number of 1.0 was assumed at the throat, with a straight sonic line. The expansive turn (Prandtl-Meyer region) immediately downstream of the throat occurs over a short axial distance and can, in principle, be treated as a centered expansion. However, for improved accuracy, the expansion was treated as a smooth curve, with wall characteristic lines taken as Mach waves inclined at the local Mach angle to the wall tangent. Symmetry about the nozzle centerline was assumed in order to limit the MOC calculation to half of the actual flow field.

Figure 7-5 shows the characteristic grid associated with the MOC analysis. Due to the compressive turn in the straightening section of the nozzle, the characteristics are seen to coalesce in the region where an internal shock is observed in the schlieren images. The MOC analysis fails in the area downstream, and radially outboard of the location of the predicted internal shock.

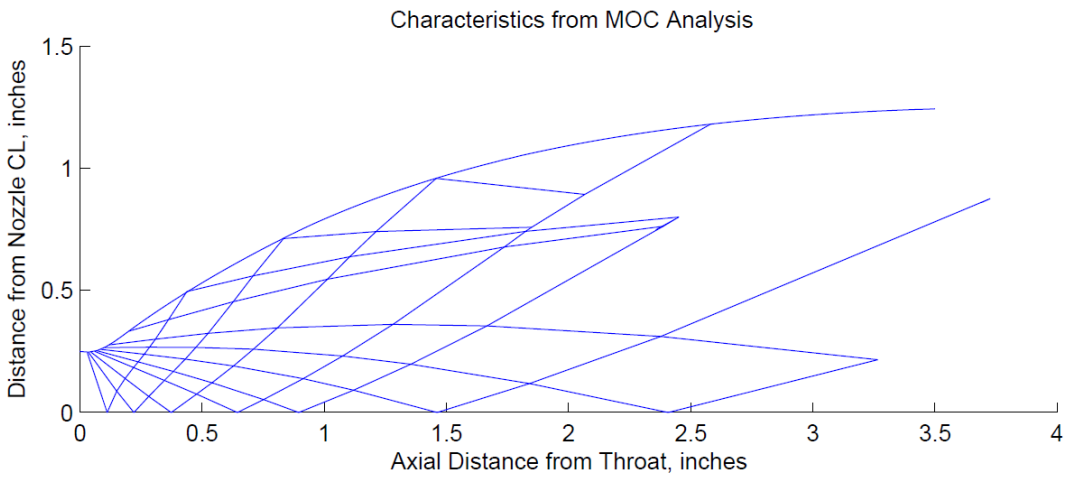

Figure 7-5: Characteristic grid for MOC analysis

Since observed facet-generated waves emanating from the wall correspond to very weak oblique shocks, or equivalently, Mach waves, the internal shock separating the large, feature-free region downstream of the nozzle throat and the near-wall flow region is assumed to be a *weak* (internal) shock. Thus, it is assumed that, outside of the near-wall boundary layers, and upstream of the internal (weak) normal shock (located immediately upstream of the nozzle exit), the *entire* flow field is isentropic. Refer to Figure 7-6.

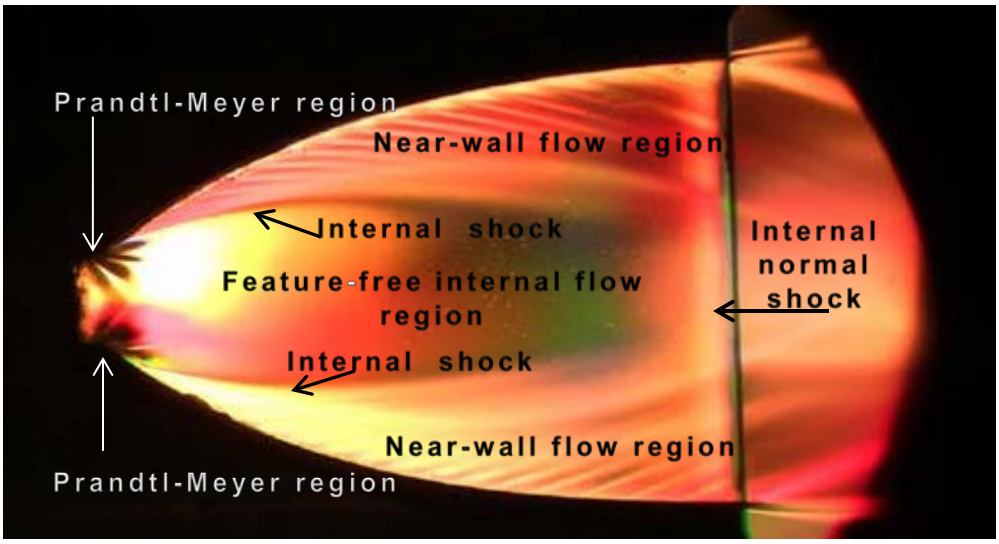

Figure 7-6: Schlieren image flow field regions/features

7.5 Results of semi-quantitative diagnosis of shock-train-free flow

The method of characteristics approach outlined above can, in principle, be is used to compute the field properties $P(\vec{x})$, $T(\vec{x})$, $M(\vec{x})$, and $\rho(\vec{x})$, throughout the entire nozzle flow field, where $\vec{x}$ denotes position within the nozzle.

Specifically, given local, i.e., nodal, Mach numbers, M, determined via the MOC calculation and given the measured plenum stagnation pressure and temperature, P_o and T_o, respectively, associated position-dependent temperature and pressure fields, $P(\vec{x})$ and $T(\vec{x})$, can be computed using the isentropic relations, Equations 6.3 and 6.5. Finally, given $T(\vec{x})$ and $P(\vec{x})$, the density field follows from the ideal gas law:

$$\rho(\vec{x}) = \frac{P(\vec{x})}{RT(\vec{x})} \qquad \text{Equation 7.26}$$

Note, in this dissertation, since the plenum stagnation temperature, T_o, was not measured, $P(\vec{x})$, $T(\vec{x})$, and $\rho(\vec{x})$ were not computed.

In order to validate the MOC calculations, predicted Mach angles along the nozzle wall are compared with those observed via the schlieren image.

As shown in Figure 7-7, the near-wall Mach angle distribution predicted by the method of characteristics calculations compares reasonably well with experimental schlieren data.

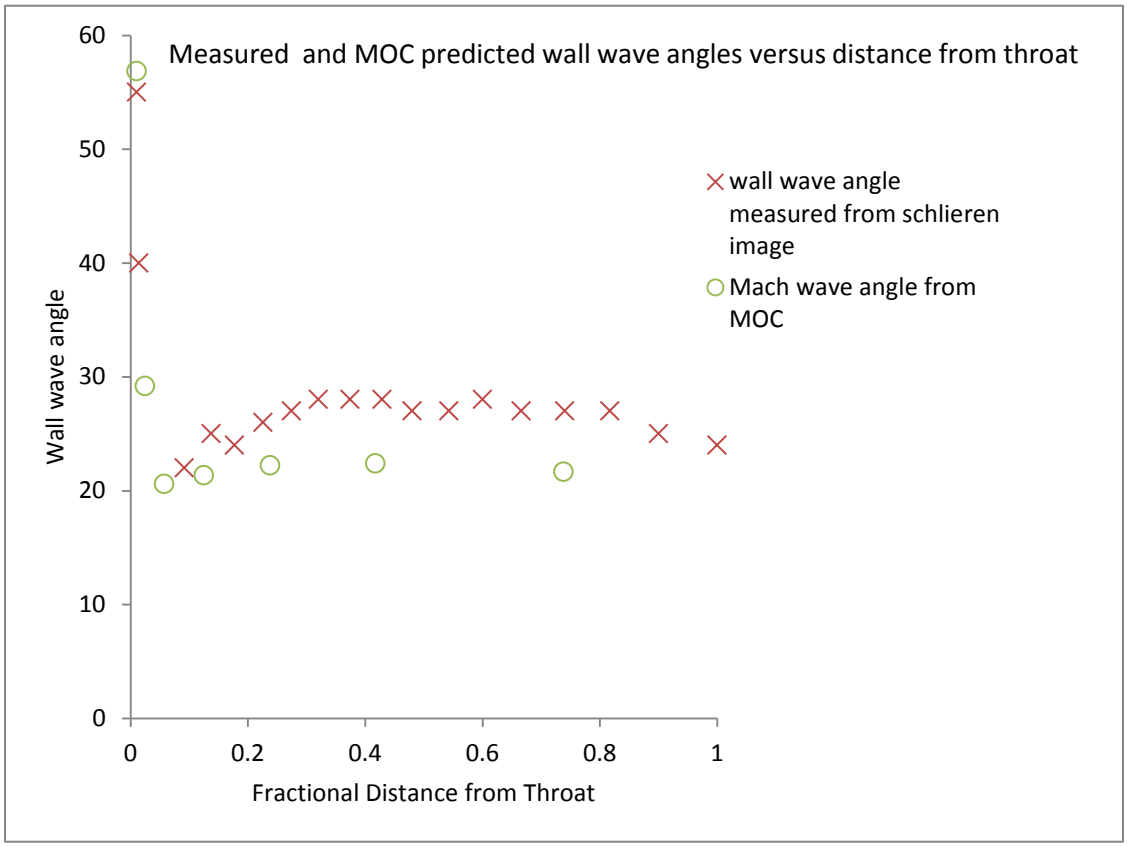

Figure 7-7: MOC-predicted wall Mach and schlieren image Mach angle versus fractional distance from throat

7.6 Final SQS diagnosis of the shock-train-free flow regime

The relatively close agreement observed between the method of characteristics calculations and the experimental data, combined with the analyses presented in Chapter 6, leads to the following, final, semi-quantitative-schlieren-based picture of shock-train-free flow in the present experimental system:

1) Prandtl-Meyer expansion fans form at the initial nozzle expansion, immediately downstream of the nozzle throat.
2) The waves generated by wall facets over $0 \leq x/L \leq 0.3$ are in fact very weak oblique shocks. The waves are classified as weak oblique shocks rather than Mach waves due to the close agreement observed between the oblique shock model calculation described in Section 6.3 and experimental image data. It should be noted, that similar results follow by assuming that the waves over $0 \leq x/L \leq 0.3$ are Mach waves; however slightly improved agreement is obtained by using the oblique shock model.
3) The facet-generated waves observed over $0.3 \leq x/L \leq 0.9$, in slight contrast, appear to be Mach waves. As noted in Section 6.3, since wall curvature is small over this region, wall facets effectively represent small perturbations to the (non-boundary layer) high speed flow. Under these circumstances, and as strongly suggested by the results in Figure 6-7 (which compare near-wall wave angles predicted by the oblique shock/Mach wave model versus experiment), it becomes apparent that these waves are most likely Mach waves.
4) Based on the above analyses of the near-wall region, it is hypothesized that weak, facet-generated waves coalesce to form a weak internal shock; refer, again to Figure 7-6.

Given the assumption that the internal shock is weak, it is idealized that the entire shock-train-free flow is nominally isentropic. Importantly, based on this idealization, a method of characteristics analysis of the entire flow was undertaken. The relatively close agreement observed between predicted and observed near-wall Mach angles in Figure 7-7 provides strong support for all of the diagnostic results described in 1) through 4).

As a closing aside, it is noted that all models used assume quasi-steady flow conditions within the nozzle. This important assumption is valid over time increments, $\Delta\tau$, that are long relative to the characteristic nozzle advective time scale (i.e. the time required for fluid particles to transit the nozzle),

$$\tau_f = L/U = O(10^{-4}\ s) \qquad \text{Equation 7.27}$$

but short relative to the experimental run-time,

$$\tau_E = O(1s) \qquad \text{Equation 7.28}$$

where, L and U are the nozzle length and characteristic flow speed, respectively. Specifically, since in-nozzle flow structure *and* plenum pressure remain nominally fixed on time scales that are long relative to τ_f, it can be safely assumed that on these scales, flow between the plenum and nozzle, as well as within the nozzle, is quasi-steady.

CHAPTER 8: TIME-DEPENDENT SEMI-QUANTITATIVE SCHLIEREN DIAGNOSIS OF THE NOZZLE BLOW-DOWN PROCESS

Chapter 7 presented a detailed semi-quantitative schlieren analysis and diagnosis of the quasi-steady nominally instantaneous flow observed in a *single* schlieren image. The essential findings of that analysis: During shock-train-free flow, most of the flow field is nominally isentropic and can thus be diagnosed using the method of characteristics. This chapter extends this instantaneous, single frame diagnosis to an examination of the time-varying, shock-train-free nozzle flow that accompanies the full nozzle blow-down process. The objective of this examination centers on gaining a broad picture of how the nozzle flow evolves during blow-down.

8.1 Methods

Consistent with a semi-quantitative schlieren-based approach, two pieces of experimental data:

i) observed, time-varying near-wall wave angles, and

ii) measured, time-varying plenum and nozzle wall pressures

are combined with a simple model of in-nozzle flow:

i) isentropic, quasi-steady flow within plenum-to-near-wall stream tubes.

8.2 Experimental Measurements

Experimentally, and as detailed in Chapter 3, time-varying wall pressures were measured at x/L = 0.25 and x/L = 0.62; the time-dependent plenum pressure was

measured at a single location within the plenum. All pressures were obtained at a sample rate of 1000 Hz.

For these experiments, a high frame rate camera (Redlake MotionXtra HG-XL), acquiring frames at 1000 frames per second, was introduced. Time-varying near-wall wave angle distributions were then determined manually, frame-by-frame, through the entire blow-down process. [Note 1: since the time scale over which in-nozzle flow structure varies is long relative to the camera frame rate, wave angle distributions were measured every 50^{th} frame.]

As noted, the blow-down process was typically complete within approximately 0.65 seconds. (See, for example, Figure 9-1 in Chapter 9.)

8.3 Isentropic stream tube model

Considering any given stream tube passing from the plenum to locations along and adjacent to either nozzle wall, it is assumed that quasi-static conditions prevail at all points within the stream tube. For this assumption to hold, time-dependent variations in nozzle and plenum pressure, temperature, density, and velocity fields must occur on time scales, τ_s, that are long relative to both the characteristic advection time scale, $\tau_f = L/U$, for particle transport through the nozzle, and the schlieren imaging and pressure measurement time scales, τ_i and τ_p, respectively. [Here, Δt_p= 0.001s and Δt_i = 0.001s are, respectively, the inverse data sample rates for the pressure sensors and the schlieren imaging system as noted in Chapter 7, $\tau_f = O(10^{-4}s)$.]

In the present set of experiments, it is readily shown that, throughout blow-down,

i) nozzle flow structure, an indirect indicator of nozzle flow field properties, varies on time scales much longer than τ_f, τ_i, and τ_p, and

ii) measured plenum and wall pressures, again surrogates for plenum and nozzle flow field properties, likewise vary on long time scales.

Thus, at any given pressure measurement time, $t_n = n\Delta t_p$, and any given schlieren imaging time, $t_m = m\Delta t_s$, it can be safely assumed that quasi-static conditions exist in any stream tube passing from the plenum and through the near-wall flow region. [The indices n and m run from 1 to N_p and 1 to N_s, respectively, where N_p and N_s are respectively the total number of pressure measurements and schlieren images captured during a given blow-down experiment.]

Based on the analyses presented in Chapter 6, it is assumed that flow in any given stream tube, is, throughout any given blow-down experiment, isentropic. Thus, assuming constant specific heats, c_p and c_v, the measured, nominally instantaneous pressures obtained at $t_n = n\Delta t_p$, within the plenum and at wall locations, $x/L = 0.25$ and $x/L = 0.62$, can be used to determine corresponding, near-wall Mach numbers:

$$\frac{P_o(t_n)}{P_{0.25}(t_n)} = [1 + \left(\frac{\gamma-1}{2}\right) M_{0.25}^2(t_n)]^{\frac{\gamma}{\gamma-1}} \qquad \text{Equation 8.1}$$

$$\frac{P_o(t_n)}{P_{0.62}(t_n)} = [1 + \left(\frac{\gamma-1}{2}\right) M_{0.62}^2(t_n)]^{\frac{\gamma}{\gamma-1}} \qquad \text{Equation 8.2}$$

Here, $t_n = n\Delta t$, is the measurement instant, $P_o(t_n)$, $P_{0.25}(t_n)$, and $P_{0.62}(t_n)$ are the measured plenum pressure and measured wall pressures at $x/L = 0.25$ and $x/L = 0.62$, respectively, $M_{0.25}(t_n)$ and $M_{0.62}(t_n)$ are corresponding near-wall Mach numbers, and $\gamma = c_p/c_v$ is the ratio of specific heats.

Consistent with the assumption of isentropic stream tube flow, and more specifically consistent with the analyses and results described in Chapter 6, it is assumed that near-wall waves are Mach waves. Thus, using the local, nominally instantaneous

Mach numbers obtained via Equations 8.1 and 8.2, corresponding theoretical Mach wave angles can finally be computed:

$$\mu_{0.25}(t_n) = \sin^{-1}\frac{1}{M_{0.25}(t_n)} \quad \text{Equation 8.3}$$

$$\mu_{0.62}(t_n) = \sin^{-1}\frac{1}{M_{0.62}(t_n)} \quad \text{Equation 8.4}$$

8.4 Comparison of time-dependent wave angles from the isentropic stream tube model with experiment

Theoretical and observed wave angle evolutions at $x/L = 0.25$ are compared in Figure 8-1. From the figure, a number of observations can be made:

a) As noted, at nozzle pressure ratios less than approximately 16.8, a shock-train exists within the nozzle. During the plenum pressurization period, extending from $t = 0$ s to approximately $t = 0.23$s, the shock-train is observed within the nozzle until approximately $t = 0.14$s. Referring to Figure 8-1, during this initial period of shock-train-dominated flow, the isentropic stream tube model does a poor job of predicting the observed evolution of the wave angle at $x/L = 0.25$.

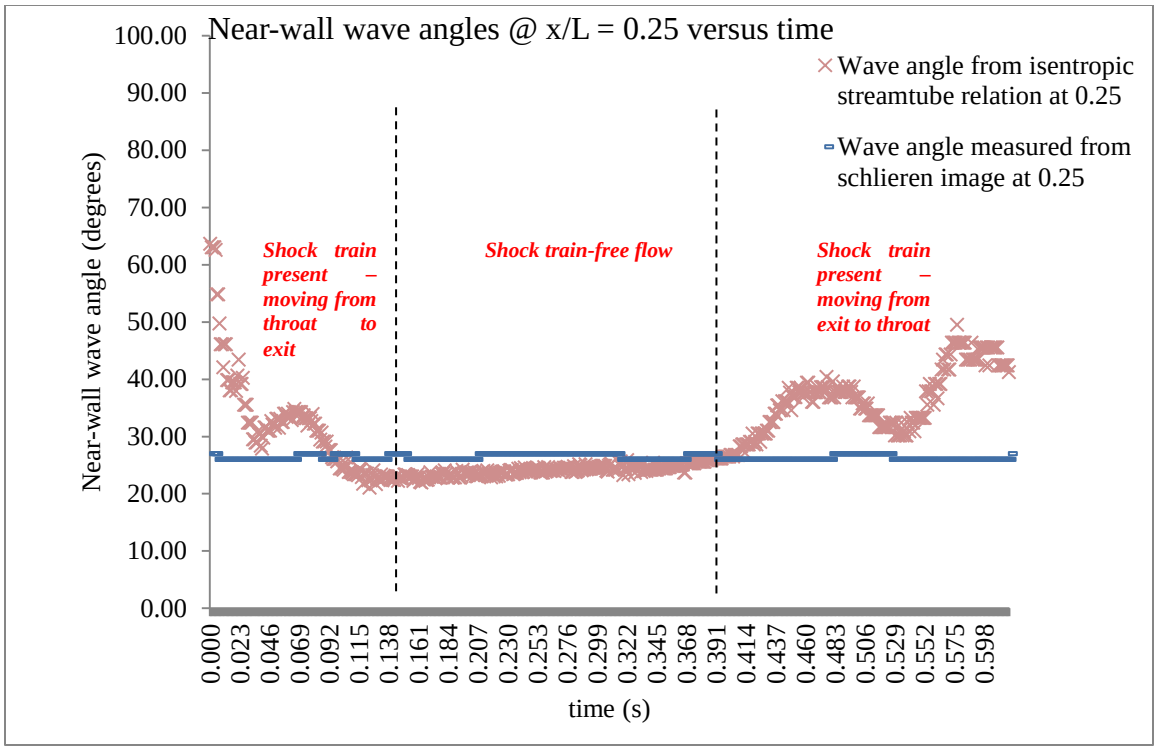

Figure 8-1: Near-wall wave angles vs time @ x/L =0.25

b) The model's over-prediction of the Mach wave angle, $\mu_{0.25}(t)$ during the first period of shock-train-dominated flow, $0 \leq t \leq 0.138$s, reflects:

i) the fact that $\mu(x)$ varies in direct proportion to $P(x)$ (which is seen, e.g., from equations 8.1 and 8.3), and

ii) the presence of a closed, pressurized, recirculation bubble which encompasses $x_{0.25}$.

With regard to the second feature, a cyclically opening and closing recirculation bubble, is strongly indicated by the cyclic pressure variation, above and below atmospheric pressure, observed at $x_{0.25}$, over the interval $0 \leq t \leq 0.138$s. Refer to Figure 8.2.

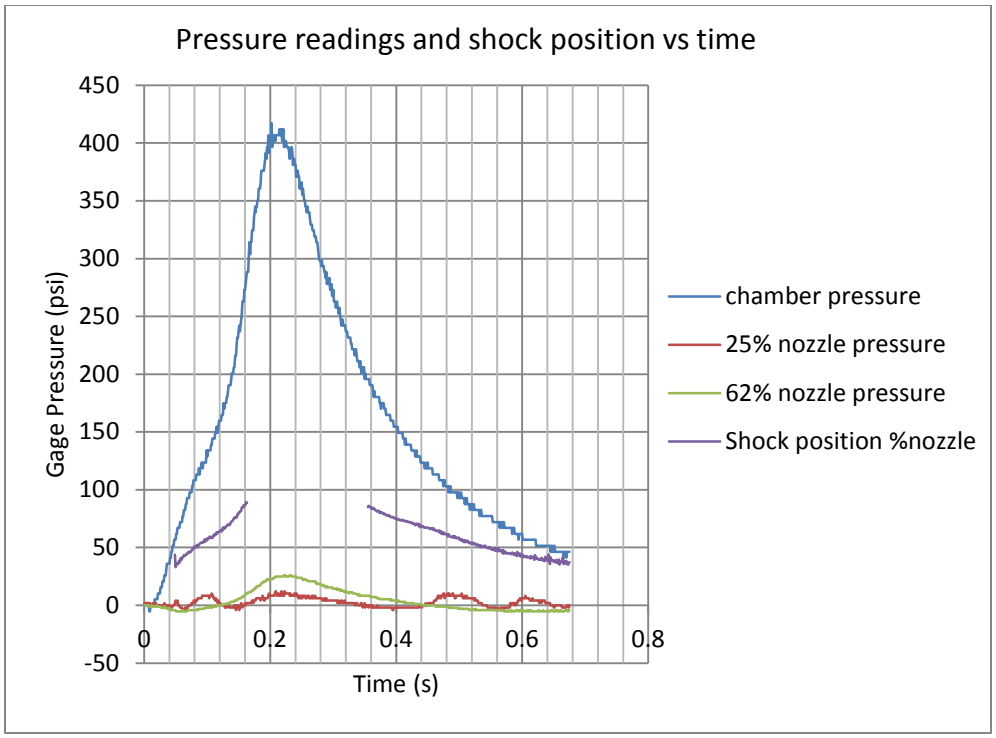

Figure 8-2: Pressure readings and shock position versus time

In particular, during the short intervals when $P_{0.25} < 0$ (i.e. when $P_{0.25}$ drops below atmospheric pressure), it is seen that $P_{0.62}$ likewise drops below atmospheric pressure. Thus, a long, thin recirculation zone, extending from the nozzle exit, upstream past $x_{0.62}$ and $x_{0.25,}$ almost certainly exists. As the normal shocks comprising the shock-train pass over $x_{0.25}$, the open recirculation zone closes, creating a (temporarily) closed recirculation bubble around $x_{0.25}$.

Thus, the model's over-prediction of $\mu_{0.25}$ during the initial period of shock-train-dominated flow, $0 \leq t \leq 0.138$s, simply reflects the existence of a closed, pressurized recirculation bubble about $x_{0.25}$.

c) Similar physical features underlie over-predicted Mach angles observed during the second period of shock-train-dominated flow, $0.391 \leq t \leq 0.598$s.

d) The relatively close agreement observed between theoretical and experimental Mach angles during the period of shock-train-free flow, $0.138 \leq t \leq 0.391$s, suggests that the flow from the plenum to $x_{0.25}$ is nominally isentropic. This result is consistent with the single-instant results reported in Chapters 6 and 7.

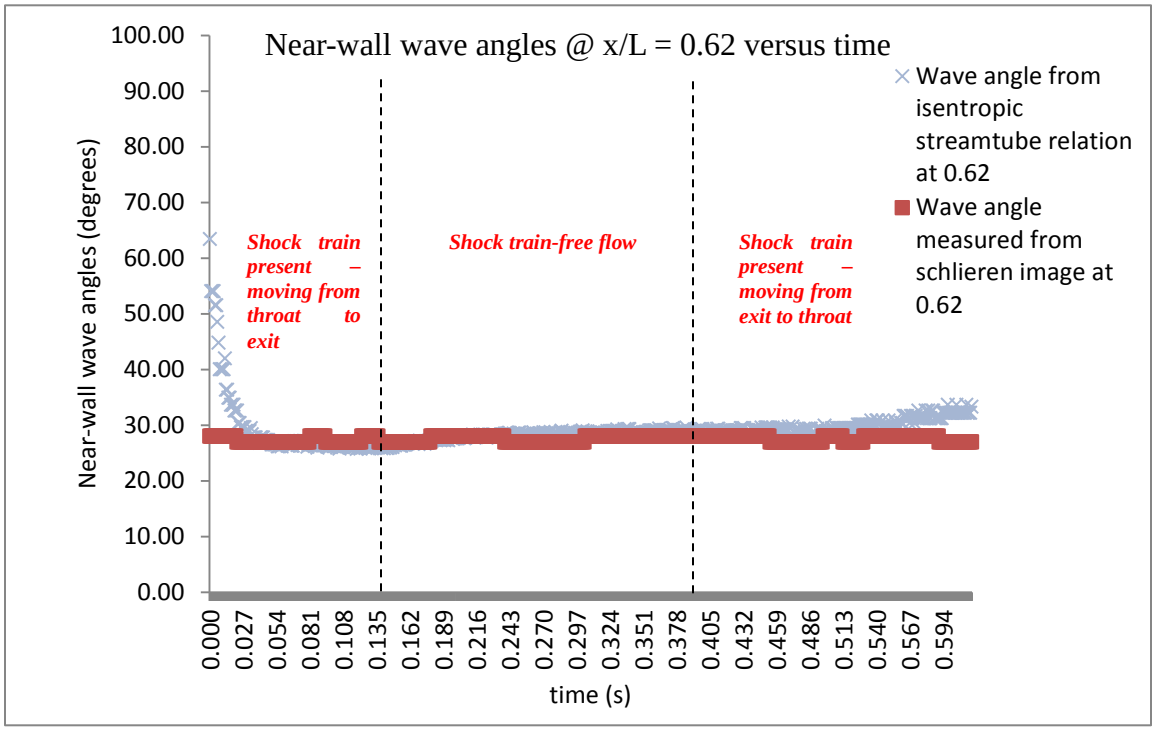

Figure 8-3: Near-wall wave angles vs time @ x/L=0.62

Figure 8-3 shows predicted near-wall wave angles at x/L = 0.62, versus wave angles measured from the schlieren image. Overall, better agreement is seen at this location compared to that obtained at x/L = 0.25. This is expected since the change in wall slope versus axial position is small, and no cyclically opening and closing separation bubble appears to exist.

CHAPTER 9: QUALITATIVE MODEL OF SHOCK-BOUNDARY LAYER INTERACTION DURING THE SHOCK-DOMINATED FLOW REGIME

9.1 Introduction

This chapter presents two new findings. First, experimental schlieren image data are presented which show that within the non-thrust optimized nozzle used in this investigation, a double-shock structure dominates the flow, at least under low NPR, overexpanded flow conditions. This appears to be the first documented observation of such structures within high-pressure ratio nozzles. Importantly, this observation represents a distinct departure from the classical picture in which only single normal shocks can exist under overexpanded flow conditions.

Second, a qualitative model is proposed which exposes the fluid dynamic processes that create this double-shock structure. The model suggests the following:

1) Under overexpanded flow conditions, the nozzle flow adjusts to the ambient external pressure through *two* shocks rather than *one* normal shock.
2) The observed double-shock structure corresponds to a *shock-train* [58,59,60,61]. This appears to be the first observation of shock-trains in high pressure nozzles.
3) The shock-train structure is produced by a series of interactions between the near-wall boundary layer, the observed shocks, and the non-boundary-layer high speed flow upstream, between, and downstream of the double shock.

The model, which provides a detailed physical description of these interactions, appears to be the first to explain the origins of shock-train structures.

9.2 Experimental schlieren and pressure data

As shown in Figures 5-1o through 5-1v, during any given blow-down experiment and during the period when plenum pressure was decaying, two nominally parallel shock-like structures were consistently observed to travel from the nozzle exit upstream toward the nozzle throat.

In order to investigate this rather unusual structure, the experimental system was enhanced as follows:

1) A Canon HD Vixia HF S100 camera, having a 30 frame-per-second image acquisition rate, was replaced by a Redlake MotionXtra HG-XL camera, having a 1000 frame-per-second image acquisition rate.
2) Pixel resolution was increased from 1431 x 767 pixels to 1504 x 1128 pixels.

Prior to presenting schlieren image data, a typical time history of the nozzle pressure ratio, NPR, is presented in Figure 9-1. As shown, the NPR exhibits a rapid initial rise as the nozzle plenum becomes pressurized by the inflow of high-pressure argon.

[As noted, for cost savings, the present experimental system uses a relatively small high pressure tank (volume = 8500 cm^3). Due to the tank's small volume, and as seen in Figure 8-1, the plenum pressure (and thus, the nozzle NPR) never achieves a fixed magnitude. Once a sufficient mass of argon has exited the supply tank, plenum pressure (and NPR) begin to decay.]

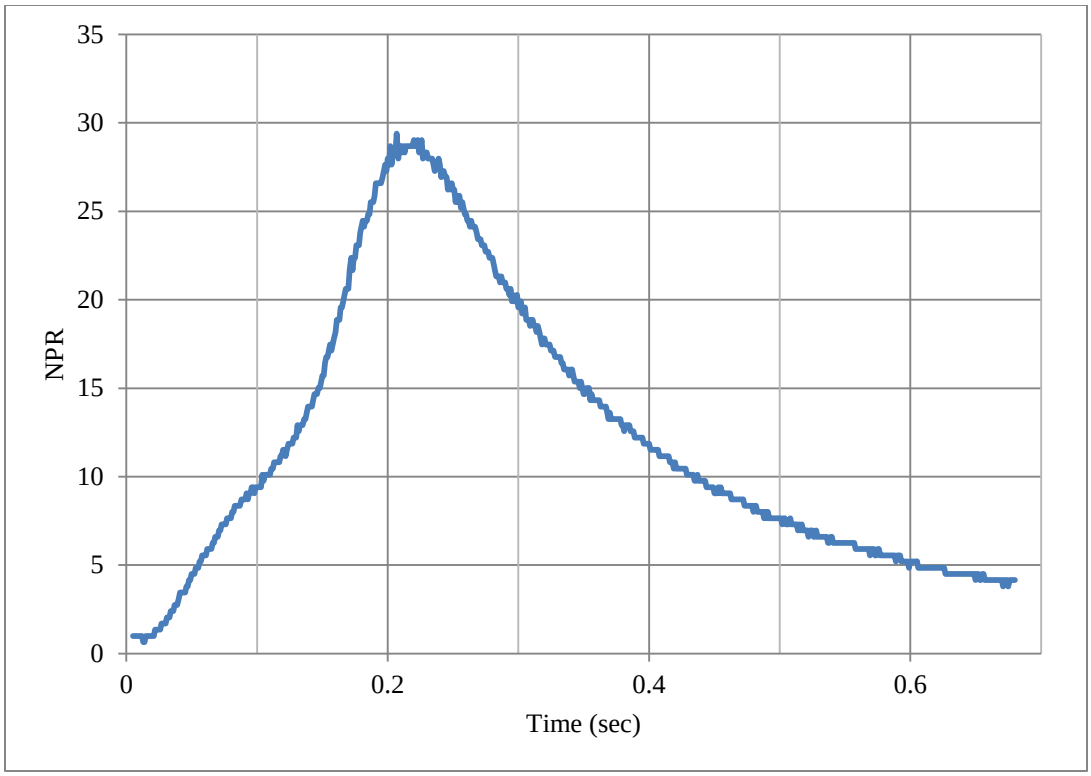

Figure 9-1: NPR as a function of time

The maximum NPR tested was approximately 30. For purposes of comparison, a typical NPR range used in full-scale rocket nozzles is on the order of $15 \leq NPR \leq 200$. Refer, for example, to Keanini and Brown [55].

Schlieren images of the blow-down process, obtained at the higher 1000 frames-per-second rate and higher image resolution, are shown in Figures 9.2a through 9.2j. It is important to note that the present experimental nozzle remains in an *overexpanded* condition – roughly indicated by the presence of normal shocks within the nozzle – at NPR's less than approximately 16.8. See, for example, Figures 9.2a through 9.2e as well as Figures 9.2g through 9.2j. By contrast, at NPR's exceeding 16.8, the nozzle flow is under-expanded and shock-free. See, for example, Figure 9.2f.

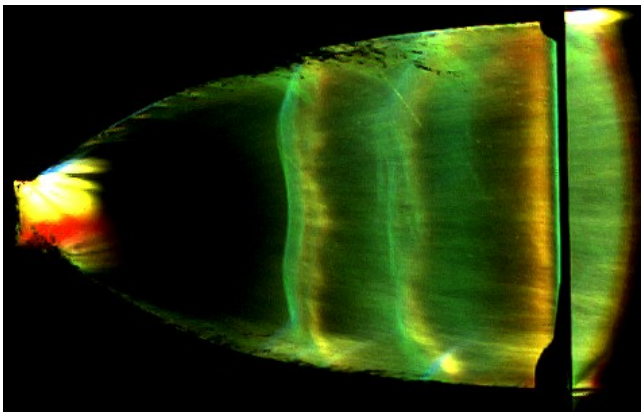

Figure 9-2a: NPR=5.905 (Time=0.062s)

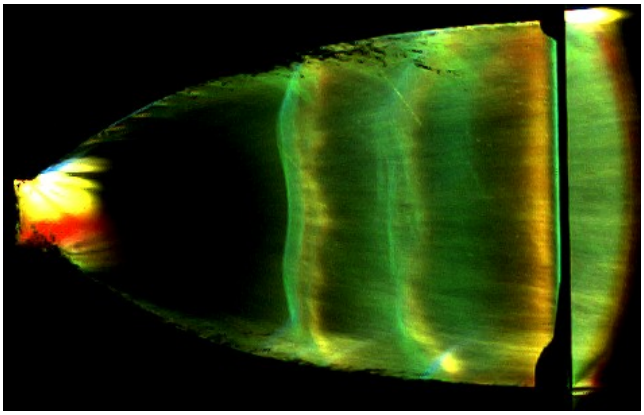

Figure 9-2b: NPR=8.708 (Time =0.088s)

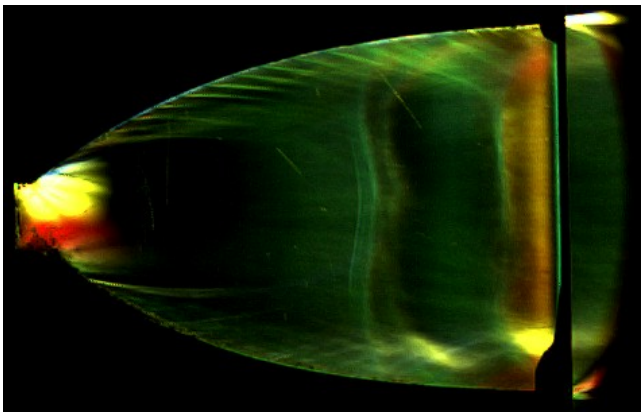

Figure 9-2c: NPR=11.511 (Time = 0.121s)

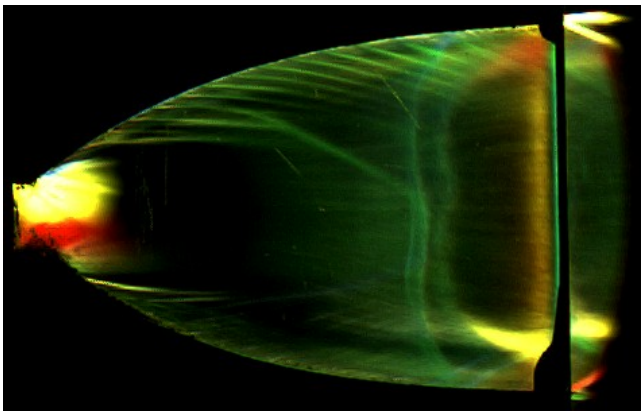

Figure 9-2d: NPR=14.314 (Time = 0.143s)

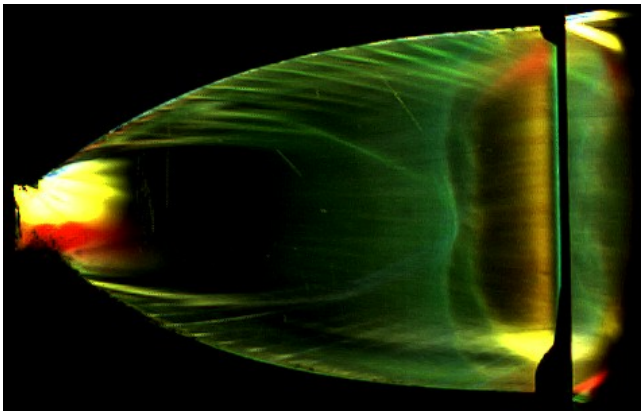

Figure 9-2e: NPR=16.767 (Time = 0.153s)

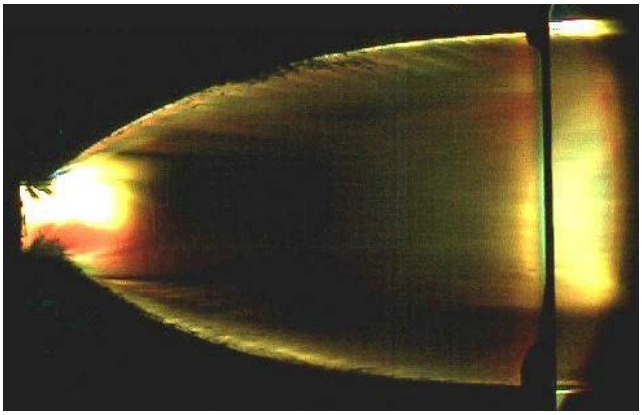

Figure 9-2f: NPR=16.767 (Time = 0.328s)

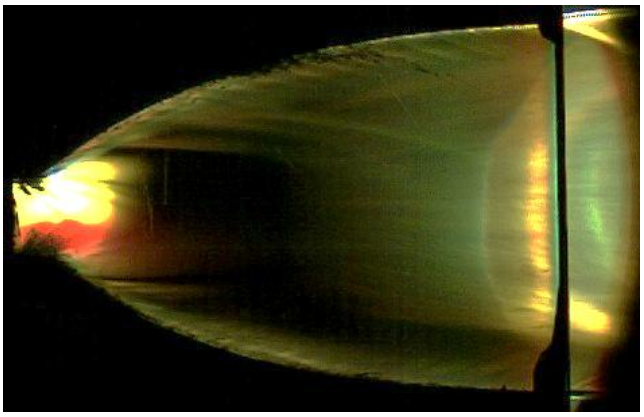

Figure 9-2g: NPR=14.314 (Time = 0.360s)

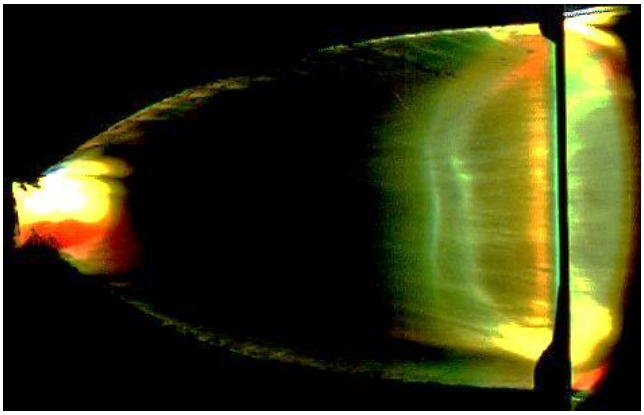

Figure 9-2h: NPR=11.511 (Time = 0.404s)

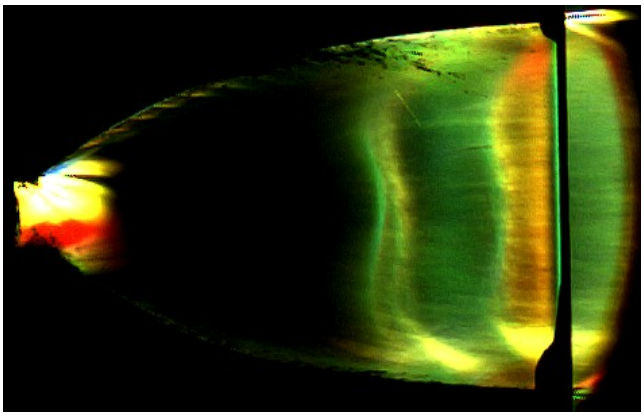

Figure 9-2i: NPR=8.708 (Time = 0.463s)

Figure 9-2j: NPR=5.905 (Time = 0.563s)

Thus, in the analyses and discussion to follow (this section and Section 9.3), it is assumed that overexpanded flow exists for NPR $\leq$ 16.8. Likewise, during shock-train-free flow, as analyzed via the semi-quantitative schlieren technique in Chapter 7, the nozzle is assumed to be underexpanded.

9.3 Discussion of new schlieren image data

During the period when plenum pressure, and thus, NPR, is increasing, an apparent pair of parallel normal shocks are observed moving downstream from the throat toward the nozzle exit; see Figures 9-2a through 9.2e.

Close examination of the figures indicates that for $11.5 \leq NPR \leq 16.77$, the shock pair still exist, but are much closer in proximity. In addition, it appears that the downstream shock becomes significantly weaker than its upstream twin. See Figures 9-2c through 9-2e.

Similarly, close examination of Figures 9-2a and 9-2b suggests the existence of *three* parallel normal shocks, where the most downstream member is weaker than the other two.

Similar structural characteristics are observed during the period when plenum pressure, and thus, NPR, is decreasing. See, for example, Figures 9-2g through 9-2j.

Note, that in many of the images, each normal shock *appears to bend* in the downstream direction. In reality, as argued in Section 9.4, the downstream-directed segments likely correspond to oblique shocks produced by the formation of virtual compression corners in the near-wall boundary layer.

Importantly, the enhanced images in Figures 9.2a through 9.2j provide the experimental foundation for exposing the physical mechanisms that produce multiple normal shocks in the experimental nozzle. Thus, in Sections 9.4 and 9.5, what appears to be the first physical model of shock-train development in high NPR nozzles is presented.

9.4 A physical model of shock trains in high NPR rocket nozzles

Random side loads often appear within overexpanded rocket nozzles, usually during low altitude flight where back pressure is relatively high. Over the last 50 years, a number of structural and catastrophic failures have been attributed to side loads [62, 63]. Current conceptual understanding traces to Summerfield et al. [64], who proposed that side load generation arises from the following chain of fluid dynamic processes: i) Under

over-expanded flow conditions, where high ambient pressure can force ambient air upstream into the nozzle. ii) The inflow, confined to the low inertia near-wall region, and in response to the inertia of the out-flowing boundary layer, eventually turns back on itself. iii) The inflow-turning process causes the nozzle boundary layer to separate which, in turn, produces a virtual compression corner. iv) The compression corner, which rings the inner circumference of the nozzle, produces an oblique shock, which also rings the nozzle. v) Since the separation line and compression corner are not perfectly symmetric – both fluctuating due to intense turbulence – a net, random, lateral pressure force, produced by the pressure jump across the asymmetric shock, acts on the nozzle wall.

While a number of visualization studies have investigated separation and side loading in planar nozzles [65], these have been carried out at nozzle pressure ratios of less than two, well-below the range, ~15<NPR<~200, characteristic of medium and large-scale rockets [66]. Due to significant variations in, e.g., shock strength, shock angle, shock-boundary-layer interaction, and separation line dynamics, under low and high NPR conditions [67, 68], visualization data at high NPRs are needed.

Current understanding of side-load generation has evolved indirectly, based in part on numerous early measurements of nozzle wall pressure distributions, obtained under overexpanded flow conditions [69, 70] (as well as reviews by [54] and [55]), and on more recent equally voluminous numerical studies (see e.g. [71, 72, 73]).

Presented, here, is the first visual data on shock-induced boundary layer separation within high NPR nozzles, obtained under time-varying NPR conditions. In marked contrast to the Summerfield picture [64] in which boundary layer separation is associated with a single normal (or quasi-normal) shock [54], a complex shock-train

structure is observed, consisting of two spatially separated, nominally self-similar quasi-normal shocks, intersecting shocks of the same family, and reflected shocks.

Significantly, the presence of a persistent, self-similar shock-train structure, visible over a range of NPR's, or equivalently, over a range of boundary layer separation locations, suggests that significant revisions to the existing Summerfield picture [64] are in order. Specifically: i) Shock-boundary layer interactions may be much more strongly coupled than previously recognized. ii) Previously measured separation-zone wall pressure distributions (see e.g. [54, 55, 64, 70]), exhibiting a gradual, rather than step-like pressure rise, may, in fact, reflect the presence of internal shock trains, as opposed to previously hypothesized single shocks [64] and (see reviews in e.g. [54] and [55]). iii) The region of near-wall turbulent flow downstream of the nominal separation line may be much thicker than previously believed (see, e.g. [54] and [55]).

In this section, visual evidence is presented of the existence of nominally self-similar, persistent shock-train structures in high-pressure-ratio rocket nozzles, as observed over a range of NPRs, and a simple physical model is proposed which explains how the nozzle boundary layer and the external non-boundary layer flow interact to create the observed shock train structure. It should be noted that this model is general and applies to any shock-train-dominated high speed flow.

9.5 A simple physical model of shock-boundary layer interaction

Figures 9-3, 9-4, and 9-5 describe a simple model which explains not only the shock-train structures observed in the present study, but those observed in, e.g., high speed duct flows, [58, 59, 60, 61]. Rather than repeating the details given in the figure and table, the following points are noted:

i) While shock-trains and associated pseudo-shock phenomena have been observed and investigated since circa. 1949 [58, 71], the model proposed here appears to be the first to provide a detailed physical explanation of how shock-shock and shock-boundary layer interactions produce an observed shock-train pattern. (See [58] for a description of pseudo-shocks and their relationship to shock-trains.)

ii) On the theoretical front, computational simulations of shock-train and pseudo-shock-dominated flows have proven difficult and non-predictive [58]. As an alternative, a number of approximate, simple models of shock-train and pseudo-shock evolution have been proposed. With respect to the latter, existing physical models [58] share the following characteristics: a) all represent lumped formulations in which amorphous boundary layers grow from the flow boundaries inward – analogous to the classical picture of internal boundary layer growth in low speed flow [74], and b) all completely neglect shock-boundary layer and shock-shock interactions.

iii) The present model, in contrast to previous physical models, provides a fine-grained description by decomposing the shock-train into simple, well-known (and easily modeled) unit-processes: a) oblique shock formation at compression corners, b) shock reflection at the intersection of shocks of the same family, c) subsonic-supersonic acceleration through convergent-divergent flow areas, d) flow through (quasi-) normal shocks, and e) boundary layer deflection due to shock

impingement. (Note: for simplicity and clarity, the figure and table below do not include, for example, formation of contact discontinuities downstream of the shock interaction lines, Prandtl-Meyer expansion fans on the lee side of diverging boundary layers, and converging shocks with shock-foot precursors to oblique shocks).

It is anticipated that the proposed model can be used in various ways: a) development of detailed, non-lumped analytical models of shock-train and pseudo-shock evolution, b) development of physically reasonable initial conditions for, e.g., parabolized numerical simulations, and c) development of inverse methods for diagnosing unresolved boundary layer regions, based on experimentally observed shock-train/pseudo-shock structures.

With respect to shock-boundary layer interaction in rocket nozzles, the present results appear to be the first to report the existence of shock-trains in high-pressure-ratio nozzles. Importantly, these results indicate that existing conceptual and theoretical constructs require revision.

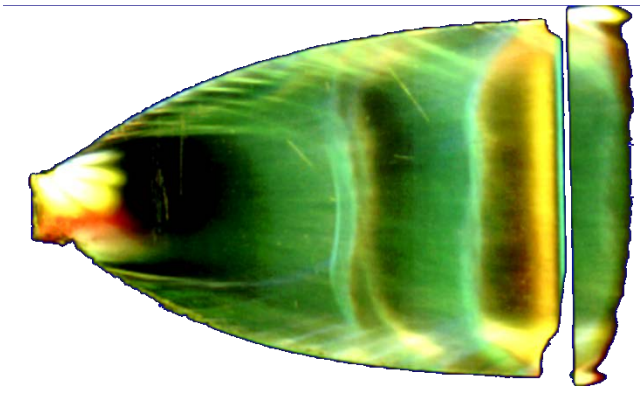

Figure 9-3: Schlieren image of shock-train structure in nozzle

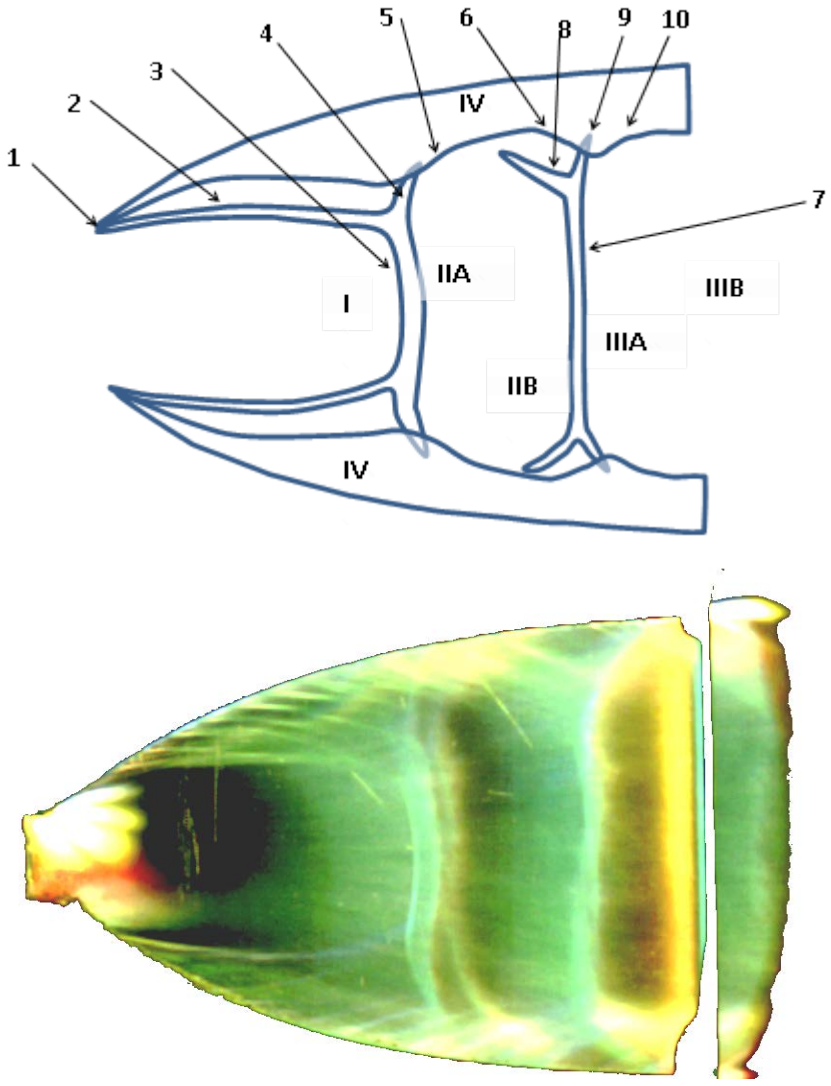

Figure 9-4: Schematic of normal shock wave/turbulent boundary layer interaction

1	Virtual compression corners formed by inflection in boundary layer.
2	Internal oblique shocks produced by 1.
3	Quasi-normal shocks.
4	Reflected shocks formed by intersection of 2 and 3.
5	Boundary layer inflection points produced by impingement of 4. The outward BL inflection produces a virtual throat, allowing the sub-sonic flow in region IIA to accelerate to supersonic conditions in region IIB.
6	Decaying pressure in supersonic region IIB produces inward BL inflections, i.e., a second set of virtual compression corners.
7	Second quasi-normal shock.
8	Second set of oblique shocks formed by 6.
9	Second set of reflected shocks formed by intersection of 7 and 8.
10	Second virtual throat, allows subsonic flow in region IIIA to accelerate to supersonic conditions in IIIB.
I	Isentropic supersonic flow region.
IIA	Subsonic Flow Region after first shock
IIB	Supersonic Flow Region before second shock
IIIA	Subsonic Flow Region after second shock
IIIB	Supersonic Flow Region after nozzle exit plane
IV	Boundary layer.

N.B. Due to slight curvature in shocks 3 and 7, regions IIA, IIB, IIIA, and IIIB are, strictly speaking, non-isentropic

Figure 9-5: Table defining the simplified physical model of shock train-boundary layer interaction

Thus, in conclusion, high speed schlieren imaging shows that, under a range of nozzle pressure ratios, a persistent, self-similar shock-train structure exists within an experimental planar nozzle. On one hand, this observation runs counter to conventional wisdom that in overexpanded nozzles, single normal (or quasi-normal) shocks underlie observed shock-induced pressure increases, and on the other, offers an alternative explanation for observed pressure increases that are gradual rather than sharp. A simple physical model provides a detailed, non-lumped, unit-process-based description of how shock-boundary layer interactions produce observed shock-train patterns. This proposed model may improve understanding of the fundamental flow processes underlying shock-train and pseudo-shock structure and evolution, and may allow the development of improved analytical and numerical models.

CHAPTER 10: CONCLUSIONS

With renewed interest in commercial supersonic flight and space vehicles, flow through rocket nozzles has been the subject of numerous computational fluid dynamics (CFD) and experimental studies.

The semi-quantitative schlieren (SQS) method offers a new, accessible, low-cost approach for investigating high-speed flow through rocket nozzles. Furthermore, SQS can serve as a precursor, adjunct, or replacement for CFD studies or can be used to further understand the flow processes within structurally complex, compressible flows. While much research has been done on combining two or more experimental high-speed flow diagnostic methods, such as combining two or more density-sensitive visualization techniques, a long-sought objective in the broad field of compressible flow diagnostics centers on development of methods like SQS which allow measurement of multiple flow field variables such as Mach number, velocity, pressure, temperature, and density fields without the introduction of sensors or other instrumentation which could disrupt the complex compressible flow fields.

Indeed, this work has shown that complex, unsteady compressible flows can be analyzed both qualitatively and quantitatively with reasonable accuracy using a relatively simple, low-cost, bench-top apparatus composed of a machined plenum/convergent-divergent nozzle fed by the blow down of a high-pressure tank. Depending on the contour chosen for the divergent portion of the nozzle, various flow structures can be produced,

including Prandtl-Meyer expansion fans, internal shocks, near-wall oblique shocks, quasi-normal shocks, shock/boundary-layer interactions, and shock trains. Using a basic schlieren system, these structures can be imaged as they evolve in time. Basic unit processes of compressible flow can then be applied to estimate flow properties such as pressures, temperatures, densities, and Mach numbers, for the entire flow field.

Future work could include other planar nozzle wall contour analysis, a comparative CFD analysis of this planar nozzle, and a loss model for the blow-down analysis.

REFERENCES

1. Tkacik, P., Keanini, R., Srivastava, N., Tkacik, M.: Color schlieren imaging of high-pressure overexpanded planar nozzle flow using a simple, low-cost test apparatus. J. Vis., no. DOI: 10.1007/s12650-010-0056-8 (2010)

2. Settles, G.S.: Schlieren and shadowgraph techniques: visualizing phenomena in transparent media. Springer, New York (2001)

3. Bryanston-Cross, P., Skeen, A., Timmerman, B., Dunkley, P., Paduano, J., Guenette, G.: Low-cost digital visualization and high-speed tracking of supersonic shockwaves. Proceedings of SPIE 5191, 156-165 (2004)

4. Merzkirch, W.: Flow Visualization, 2nd ed. Academic Press, (1987)

5. Porro, R.: Pressure Probe Designs for Dynamic Pressure Measurements in a Supersonic Flow Field. Paper appears in Instrumentation in Aerospace Simulation Facilities, 19th International Congress on ICIASF 2001, 417-426 (2001)

6. Tavoularis, S.: Measurements in Fluid Mechanics Chapter 8, Cambridge University Press, 179-207 (2005)

7. Buchele, D., Griffin, D.: Compact color schlieren optical system. Applied Optics 32(22), 4218-4222. (1993)

8. Elsinga, G., Van Oudheusen B., Scarano, F., Watt, D.: Assessment and application of quantitative schlieren methods: calibrated color schlieren and background-oriented schlieren. Experiments in Fluids 36, 309-325 (2004)

9. Kleine, H., Takayama, K.: Flow visualization by colour schlieren and holographic interferometry. Proceedings of SPIE In *Optical Diagnostics for Industrial Applications*, Neil A. Halliwell, Editor. 4076, 78-87 (2000)

10. Kleine, H., Gronig, H., Takayama, K.: Simultaneous Shadow, Schlieren, and Interferometric Visualization of Compressible Flows, Optics and Lasers in Engineering. 44, 170-189 (2006)

11. Goldstein R., Kuehn, T.: Optical Systems for flow measurement: Shadowgraph, schlieren, and interferometric techniques. In Fluid Mechanics Measurement. Taylor and Francis 451-508. (1996)

12. Arnaud, E., Memin, E., Sosa, R., Artana, G.: Author manuscript published in "IEEE European Conference on computer vision. A fluid motion estimator for Schlieren image velocimetry. (2006)

13. Bruun, H.: Measurement Science and Technology. Hot-Wire Anemometry: Principles and Signal Analysis. 7(10) (1996)

14. Fingerson, L., Freymuth, P.: Chapter 3, Fluid Mechanics Measurements, Edited by Richard J Goldstein, Taylor and Francis Phila 2, 115-174 (1996)

15. Seiner, J.: The wedge hot-film anemometer in supersonic flow. NASA Scientific and Technical Information Branch, Washington DC. (1983)

16. Clemens, N., Mungal, M.: A planar Mie scattering technique for visualizing supersonic mixing flows. Experiments in Fluids 11(2), 175-185 (1991)

17. Gendrich, C., Koochesfahani, M., Nocera, D.: Molecular tagging velocimetry and other novel applications of a new phosphorescent supramolecule. Experiments in Fluids 23(5), 361-372 (1997)

18. Herring, G., Lee, S., She, C.: Measurements of a supersonic velocity in a nitrogen flow using inverse Raman spectroscopy. Optics Letters 8(4), 214-216 (1983)

19. Mueller, T.: Flow visualization by direct injection. Fluid Mechanics Measurements (ed. R.J. Goldstein) Hemisphere, Washington, 307-375 (1983)

20. Lippisch, A.: Aeronautical Engineering Review 17, 24-36 (1958)

21. McGregor, I.: The vapour-screen method of flow visualization. J. Fluid Mech. 11, 481-511 (1961)

22. Falco, R., Chu, C.: Measurement of two-dimensional fluid dynamic quantities using a photochromic grid-tracing technique. Proc. SPIE 814, 706-710 (1978)

23. Stanislas, M.: Ultra-high-speed smoke visualization of unsteady flows using a pulsed ruby laser 3rd Int. Symposium on Flow Visualization, W.J. Yang, Editor, Hemisphere Pub. (1983)

24. Shiraishi, N., Matsumoto, M., Shirato, H.: On aerodynamic instabilities of tandem structures. 6th Colloquium industrial aerodynamics, Fachhochschule Aachen, Germany, 2, 179 (1985)

25. Dimotakis, P., Debussy, F., Koochesfahani, N.: Particle streak velocity field measurements in a two-dimensional mixing layer. Phys. Fluids 24, 995-999 (1981)

26. Van Dyke, M.: An Album of Fluid Motion. The Parabolic Press, Stanford, CA Aeronautical Sciences 128-283 (1982)

27. Escoda, M., Long, M.: Rayleigh scattering measurements of the gas concentration field in turbulent jets. AIAA J. 21, 81-84 (1983)

28. Long, M., Fourguette, D., Escoda, M., Layne, C.: Instantaneous Ramanography of a turbulent diffusion flame. Optics Letters 8(5), 244-246 (1983)

29. Lapp, M.: Laser Raman Gas Diagnostics edited by M.Lapp and C.Peare Plenum, New York. 130 (1974)

30. Harvey, A.: editor. Chemical applications of nonlinear Raman spectroscopy. Academic Press, New York. (1981)

31. Miles, R.: Resonant Doppler velocimeter. Phys. Fluids 18, 751 (1975)

32. Massey, G., Lemon, C.: Feasibility of measuring temperature and density fluctuations in air using laser-induced O_2 fluorescence. IEEE J. Quantum Elect. QE-20, 454-457 (1984)

33. Lee, M., Paul, P., Hanson, R.: Quantitative imaging of temperature fields in air using planar laser-induced fl-O_2. Opt. Lett 12, 75-77 (1987)

34. Zimmermann, M., Miles, R.: Hypersonic helium flow field measurements with the resonant Doppler velocimeter. Appl. Phys. Ltrs. 37, 885-887 (1980)

35. Miles, R., Connors, J., Markovitz, E., Howard, P., Roth, G.: Proposed single-pulse two-dimensional temperature and density measurements of oxygen and air. Optics Letters 13, 195-197 (1988b)

36. Miles, R., Cohen, C., Connors, J., Howard, P., Huang, S., Markovitz, E., Russell, G.: Velocity measurements by vibrational tagging and fluorescent probing of oxygen. Optics Letters, 12, 861 (1987)

37. Miles, R., Connors, J., Markovitz, E., Howard, P., Roth, G.: Instantaneous supersonic velocity profiles in an underexpanded sonic air jet by oxygen flow tagging. Phys Fluids A 1, 389-393 (1989)

38. Miles R., Nosenchuck D.: Three-dimensional quantitative flow diagnostics. In Lecture Notes in Engineering 45. Springer Verlag, Berlin 74, 33-107 (1989)

39. Faris, G., Byer, R.: Beam-deflection optical tomography. Optics Letters, 12, 72 (1987)

40. Sweeney, D., Vest, C.: Measurement of three-dimensional temperature fields above heated surfaces by holographic interferometry. Intl J. of Heat and Mass Transfer, 17, 1443-1454 (1974)

41. Snyder, R., Hesselink, L.: Measurement of mixing flows with optical tomography. Optics Letters 13, 87-89 (1988)

42. Fujii, K.: CFD Contributions to high-speed shock-related problems. Shock Waves 18, 145-154 (2008)

43. Hadjadj, A., Onofri, M.: Nozzle flow separation. Shock Waves 19, 163-169 (2009)

44. Fiorina B., Lele S.: An artificial nonlinear diffusivity method for supersonic reacting flows with shocks. Journal of Computational Physics 222, 246-264 (2007)

45. Adams, N., Shariff, K.: A high-resolution hybrid compact-ENO scheme for shock turbulence interaction problems, J. Computational Physics 127, 27-51 (1996)

46. Adams, N.: Direct numerical simulation of the turbulent boundary layer along a compression ramp at M=3 and Re=1685. J. Fluid Mechanics 420, 47-83 (2000)

47. Pirozzoli, S.: Conservative hybrid compact-WENO schemes for shock-turbulence interaction. J. Computational Physics 178, 81-117 (2002)

48. Rizzetta, D., Visbal, M., Gaitonde, D.: Large-eddy simulation of supersonic compression ramp flow by high-order method. AIAA J. 39(12), 2283-2292 (2001)

49. Deng, X., Zhang, H.: Developing high-order weighted compact nonlinear schemes. J. Computational Physics 165, 22-44 (2000)

50. Ristic, S.: Optical methods in wind tunnel flow visualization. FME Transactions 34, 7-13 (2006)

51. Buchele, D., Griffin, D.: Compact color schlieren optical system. Applied Optics 32(22), (1993)

52. Vandiver, J.: High speed colour schlieren photography. Nature 252 (1974)

53. Srivastava, N., Tkacik, P., Keanini, R.: Influence of nozzle random side loads on launch vehicle dynamics. J. Appl Phys. 108, 11-19 (2010)

54. Ostlund, J.: Flow Processes in Rocket Engine Nozzles with Focus on Flow Separation and Side-loads. Royal Institute of Technology, PhD Thesis, Stockholm, Sweden, (2002)

55. Keanini, R., Brown, A.: Scale Analysis and Experimental Investigation of Compressible Turbulent Boundary Layer Separation in Nozzles. Euro. J. Mech. B - Fluids 26, 494-510 (2007)

56. Meyer, T.: Über zweidimensionale Bewegungsvorgänge in einem Gas, das mit Überschallgeschwindigkeit strömt. Göttingen: Ph.D. dissertation, Georg-August Universität, (1908)

57. Anderson, J.: Modern compressible flow with historical perspective. New York: McGraw-Hill, (1990)

58. Matsuo, K., Miyazato, Y., Kim, H.: Shock train and pseudo-shock phenomena in internal gas flows. Progress in Aerospace Sciences 35, 33-100 (1999)

59. Nill, L., Mattick, A.: An experimental study of shock structure in a normal shock train. AIAA Paper, 96-0799, 96-99 (1996)

60. Hunter, L., Couch, B.: A CFD study of precombustion shock-trains from Mach 3-6. AIAA Paper, 90-2220 (1990)

61. Sullins, G., McLafferty, G.: Experimental results of shock trains in rectangular ducts. AIAA Paper, 92-5103 (1992)

62. Doyle, S., Biggs, R.: Space Shuttle Main Engine the First Ten Years. In: History of Liquid Rocket Engine Development in the United States: 1955-1980. American Astronautical Society (1992)

63. Sekita, R., Watanabe, A., Hirata, K., Imoto, T.: Lessons Learned from H-2 Failure and Enhancement of H-2A Project. Acta Astronautica 48, 5-12 (2001)

64. Summerfield, M., Foster, C., Swan, W.: Flow separation in overexpanded supersonic exhaust nozzles. 24, 319-321 (1954)

65. Papamoschou, D., Zill, A., Johnson, A.: Supersonic Flow Separation in Planar Nozzles. Shock Waves 19, 171-183 (2009)

66. Dungan, T.: A-4/V-2 Makeup - Tech Data & Markings. V2ROCKET.COM http://www.v2rocket.com/start/makeup/design.html (2012)

67. Tkacik, P., Keanini, R., Srivastava, N., Tkacik, M.: Color schlieren imaging of high-pressure overexpanded planar nozzle flow using a simple, low-cost test apparatus. J. Vis., no. DOI: 10.1007/s12650-010-0056-8, (2010)

68. Keanini, R., Srivastava, N., Tkacik, P., Weggel, D., Knight, P.: Stochastic Rocket Dynamics Under Random Nozzle Side Loads: Ornstein-Uhlenbeck Boundary Layer Separation and its Coarse Grained Connection to Side Loading and Rocket Response. Ann. Phys. 523 (2011)

69. Tomita, T., Takahashi, M., Sasaki, M., Sakamoto, H.: Experimental evaluation of side-loads in LE-7A prototype. Shock Waves 19 (2009)

70. Foster, C., Cowles,F.: Experimental Study of Gas-Flow Separation in Overexpanded Exhaust Nozzles for Rocket Motors. Jet Propulsion Laboratory, California Institute of Technology, Pasadena, CA, USA (1949)

71. Gross, A., Weiland, C.: Numerical Simulation of Separated Cold Gas Nozzle Flows. J. Prop. Power 20(3) (2004)

72. Chen, C., Chakravarthy, S., Hung, C.: Numerical Investigation of Separated Nozzle Flows. AIAA Journal 32(9) (1994)

73. Bocaletto, L., Lequette, L.: CFD Computation for Rocket Engine Start-up Simulation. in 41st AIAA/ASME/SAE/ASEE Joint Propulsion Conference & Exhibit, Tuscon, AR, USA (2005)

74. Schlichting, H., Kestin, J.: Boundary Layer Theory, Berlin: McGraw-Hill (1979)

APPENDIX A: PRANDTL-MEYER FUNCTION ANALYSIS

```
function prandtl_meyer_fn  %                    2011       Thorsett-
Hill
%This program determines the downstream properties which result from
an
%expansive wall turn of theta degrees starting at an input Mach
number.
%The Prandtl-Myer function is solved using a root finder which
employs
%Newton's method. This is valid for compressive or expansive turns
as %long as there is no slope discontinuity in the wall
%(smooth turns rather than ramps.)
%A plot of Prandtl-Myer function vs Mach number is produced for the
%specified gamma.  Gamma must be hard coded.
clc;
gamma = 1.4;   %ratio of specific heats
M1 = input('input upstream Mach number: ');
nu = get_nu(M1,gamma); %get P-M function, nu, for upstream Mach
theta = input('input turning angle,(degrees): ');
theta = theta*pi/180;  %convert to radians
nu = nu + theta;       %calculate downstream P-M function, nu
pm(nu,gamma,M1);
end
%-------------------------------------------------------------------
-----
function pm(nu,gamma,M1)
M = newton(nu,gamma);  %calculate downstream Mach
nu_d= nu*180/pi;       %convert to degrees
mu = asin(1/M)*180/pi; %mach angle in degrees
poop = (1 + M*M*(gamma-1)/2)^(gamma/(gamma-1)); %stag pres/stat
pressue
fprintf('Mach= %g    f(M)=  %g      mu=%g\n',M,f(nu,M,gamma),mu);
plot_PM(gamma,M1,M,nu_d,mu,poop);
end %pm
%-------------------------------------------------------------------
-----
function root = newton(nu,gamma)
%locate the root using the Newton-Raphson technique
count = 0;                %count the number of times through the
loop
M = 2.5;                  %initial guess for Mach number (used in
Newton)
while(abs(f(nu,M,gamma)) >= .0001) %while not converged
    count = count + 1;    %increment counter
    M = M - f(nu,M,gamma)/fprime(nu,M,gamma);
    if count > 500        %solver failed
        fprintf('root not found');
        break             %quit looking after 500 attempts
    end
end %while
```

```
root = M; %return current root
end %newton
%-------------------------------------------------------------------
-----
function fx = f(nu,M,gamma) %evaluate function at current Mach
    fx = get_nu(M,gamma) - nu;
    %RHS - nu is zero for correct value of Mach
end
%-------------------------------------------------------------------
-----
function fp = fprime(nu,M,gamma) %evaluate the derivative
numerically
     fp = (f(nu,M + .001,gamma) - f(nu,M,gamma))/.001;
end


%-------------------------------------------------------------------
------
function plot_PM(gamma,M1,mach,nu_d,mu,poop)
m=1;          %starting value of Mach for plot
  for i = 1:50
    M(i)=m;   %store Mach number as vector for plotting
    nu(i) =get_nu(m,gamma); %P-M function
    m = m + .1; %increment Mach number
  end
  plot(M,nu*180/pi);
  title('Prandtl-Myer function vs. Mach number')
  xlabel('Mach number')
  ylabel('Prandtl-Myer angle (degrees)')
  grid
  gamma_string = sprintf('gamma = %g',gamma);
  mach_string = sprintf('downstream Mach number = %4.2f',mach);
  up_mach_string = sprintf('upstream Mach number = %4.2f',M1);
  nu_string = sprintf('P-M functiion, nu = %4.2f degrees',nu_d);
  mu_string = sprintf('Mach angle, mu = %4.2f degrees',mu);
  poop_string = sprintf('total press/static pres = %4.2f',poop);
  text(1.45,64,gamma_string);
  text(1.45,58,up_mach_string);
  text(3.25,15,mu_string);
  text(3.25,25,mach_string);
  text(3.25,35,nu_string);
  text(3.25,5,poop_string);
end %plot
%-------------------------------------------------------------------
-------
function nu = get_nu(M,gamma)
  gp = (gamma + 1)/(gamma - 1);
  M2 = M*M;
  nu = sqrt(gp)*atan(sqrt((M2-1)/gp))-atan(sqrt(M2-1));
end %get_nu
```

APPENDIX B: BLOWDOWN MODEL

```
function blowdown                                          %Thorsett-Hill
11/10
%This program calculates the isentropic blowdown of a calorically
perfect
%gas through a CD nozzle
%
clc;               %clear command window
clear;             %clear variables and functions from memory
PoverP0_crit = .99;%Pb/P0 required to choke nozzle for given area
ratio (user input)
conv_only = 0;     %set this flag to 1 if convergent nozzle,
PoverP0_crit is calc below
T0 = 300.;         %stagnation temperature, K (user input)
t = 0;             %initialize time
P0 = 14400.;       %stagnation pressure, kPa  (user input)
Pb = 101;          %atmospheric pressure (back pressure), kPa  (user
input)
dt = .001;         %time step
%assume choked flow from the start
Cp = .5203;        %kJ/kg-K  (user input)
Cv = .3122;        %kJ/kg-K  (user input)
R = Cp - Cv;       %gas constant
k = Cp/Cv;
vol = 8.66e-3;     %volume to be blown down, m^3  (user input)
Aratio = 5;        %user input (exit plane area)/(throat area)
At = 3.221e-4;     %throat area, m^2 (CD nozzle throat) (user input)
if conv_only == 1  %nozzle is convergent only
    PoverP0_crit = (2/(k+1))^(k/(k-1)); %Pb/P0 required to choke
nozzle
    Aratio = 1;
    fprintf('P/P0 crit = %g\n',PoverP0_crit);
end
Ae = At*Aratio;    %exit plane area
m = P0*vol/R/T0;   %initial mass in blowdown volume, kg
fprintf('m = %g   P0 = %g   T0 = %g\n',m,P0,T0); %print initial cond.
for i = 1:1000
    if Pb/P0 > PoverP0_crit  %nozzle not choked, subsonic solution
using
                             %exit plane props
        Pe = Pb;             %exit plane pressure = Pb (back
pressure)
        Te = T0*(Pe/P0)^((k-1)/k);     %calc exit plane temp as
                             %isentropic expansion
        Ve = sqrt(2*Cp*(T0-Te)*1000);  %speed at exit plane
        mach = Ve/sqrt(k*R*Te*1000);
        mdot = Pe*Ve*Ae/R/Te;%mass flw rate at ext pln for unchoked
flow;
        T = Te;                    %for use in T0new calculation
below
```

```
        fprintf('unchoked t=%g  P0=%g  T0=%g  Ve=%g  Pe=%g  Te=%g
mach=%g\n',t,P0,T0,Ve,Pe,Te,mach);
    else           %choked, using throat properties for mdot
calculation
        Tt = T0/(1+(k-1)/2) ;      %temp at throat, M = 1
        Vt = sqrt(k*R*Tt*1000);%spd at throat=spd of sound at throat
temp
        Pt = P0*(Tt/T0)^(k/(k-1));%calc throat press as an isntrpic
exp
        mdot = Pt*Vt*At/R/Tt; %mass flow rate at throat for choked
flow;
        T = Tt;                    %for use in T0new calculation
below
        fprintf('t=%g  P0=%g  T0=%g  Vt=%g  Pt=%g
Tt=%g\n',t,P0,T0,Vt,Pt,Tt);
    end
    fprintf('mass=%g  mdot=%g\n',m,mdot);
    mnew = m - mdot*dt;        %calc new mass in volume after time
step
    T0new = (m*T0 - mdot*k*T*(1+R/2/Cv)*dt)/mnew;   %new stagnation
temp
                                                    %after time step
    P0new = mnew*R*T0new/vol;%calc new stag pres frm idl gas eqn of
state
    %P0new = P0*(T0new/T0)^((k/(k-1))); %calc new stag pressure as
                                       %isentropic expansion
    m = mnew;
    T0 = T0new;
    P0 = P0new;
    t0plot(i) = T0; %store T0 in array for plotting
    p0plot(i) = P0; %store P0 in array for plotting
    tplot(i) = t;   %store time in array for plotting
    t = t + dt;     %increment time
    if P0 <= Pb     %stop if sta press is less than or eql to bk
pressure
        ifinal = i; %number of times through the loop
        break       %get out of for loop
    end
end
fprintf('%d times through the loop\n',ifinal);
plot_pressure(tplot,p0plot,t0plot);  %call plot function
%-------------------------------------------------------------------
-----
function plot_pressure(tplot,p0plot,t0plot)
title('Stagnation Pressure and Stagnation Temperature vs. Time')
ax = plotyy(tplot,p0plot,tplot,t0plot);
xlabel('Time (seconds)')
axes(ax(1));
ylabel('Stagnation Pressure (kPa)') %y axis label on left
axes(ax(2));
ylabel('Stagnation Temperature (K)')%y axis label on right
%grid
```

APPENDIX C: SCHLIEREN IMAGES TAKEN AT 30 FRAMES PER SECOND

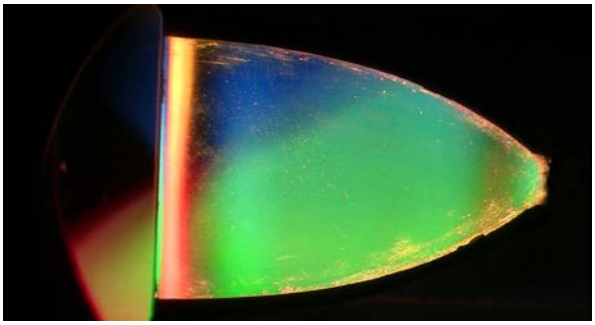

Figure C-1a Schlieren image 30fps, t=0.033s

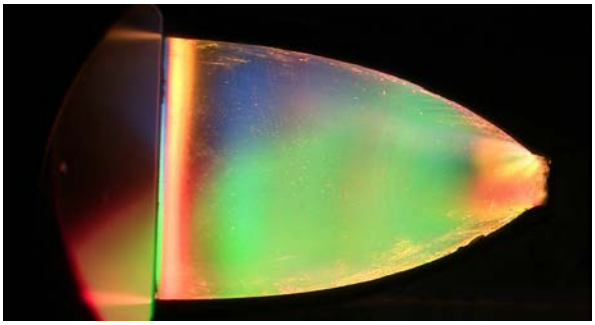

Figure C-1 Schlieren image 30fps, t=0.066s

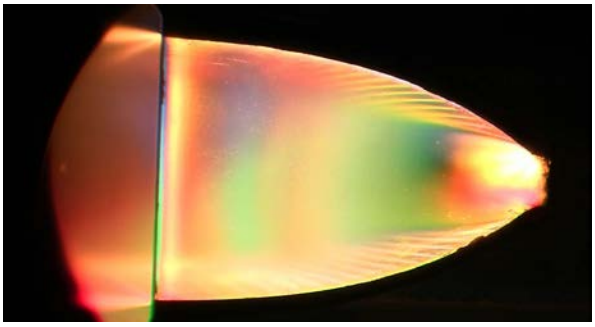

Figure C-2 Schlieren image 30fps, t=0.0996s

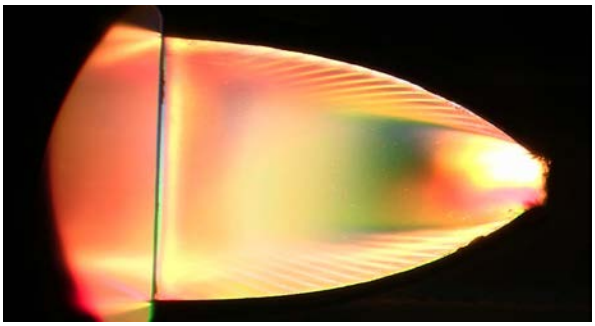

Figure C-3 Schlieren image 30fps, t=0.133s

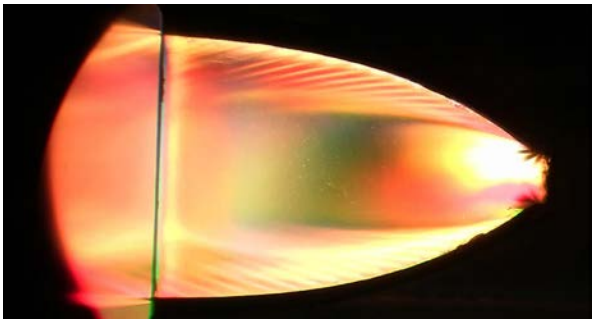

Figure C-4 Schlieren image 30fps, t=0.167s

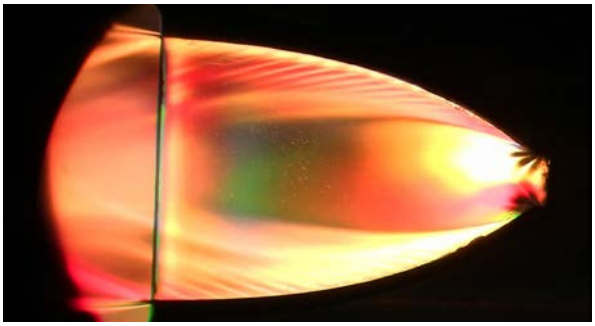

Figure C-5 Schlieren image 30fps, t=0.199s

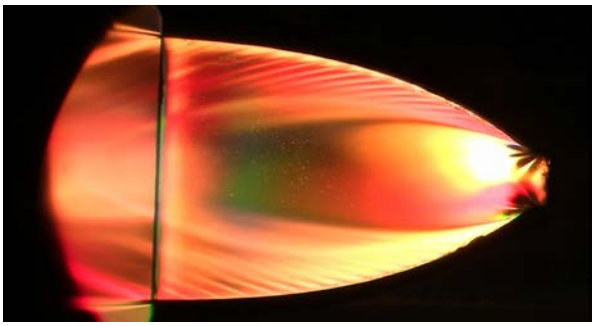

Figure C-6 Schlieren image 30fps, t=0.232s

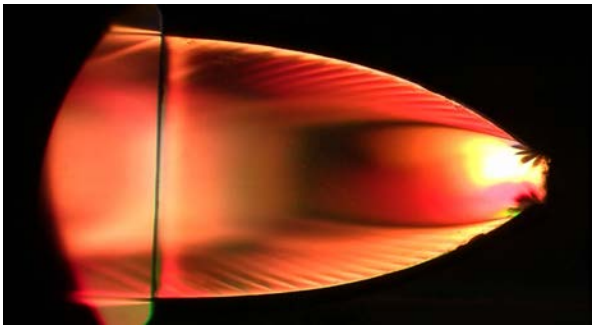

Figure C-7 Schlieren image 30fps, t=0.266s

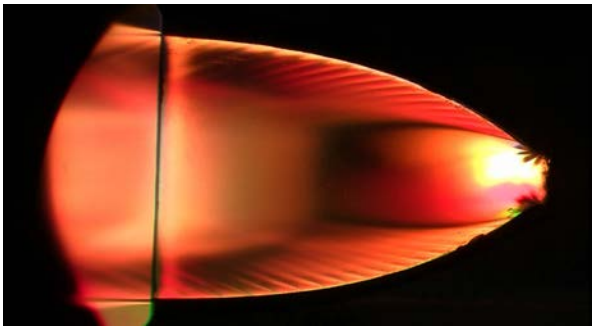

Figure C-8 Schlieren image 30fps, t=0.299s

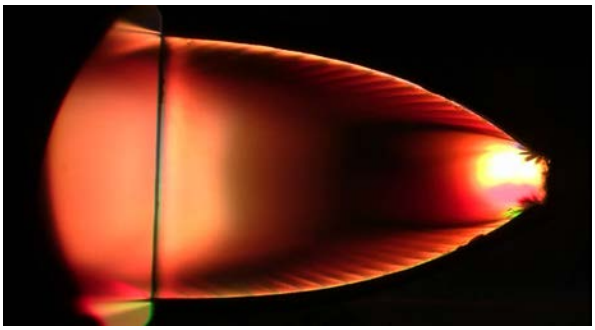

Figure C-9 Schlieren image 30fps, t=0.332s

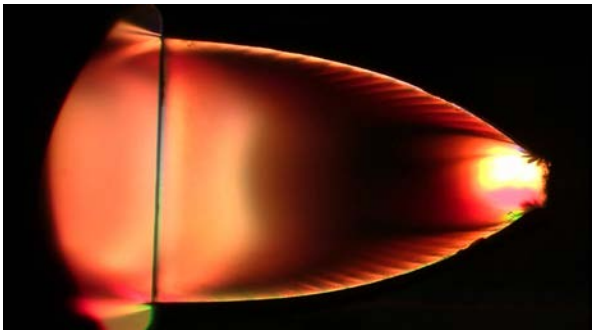

Figure C-10 Schlieren image 30fps, t=0.365s

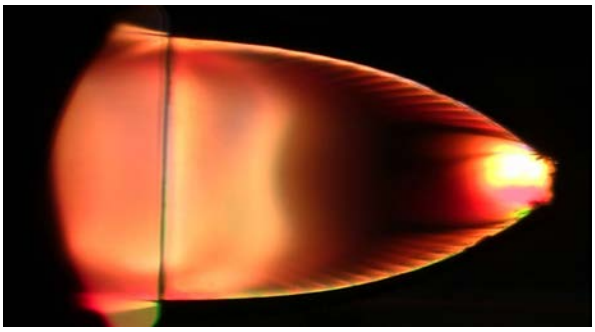

Figure C-11 Schlieren image 30fps, t=0.399s

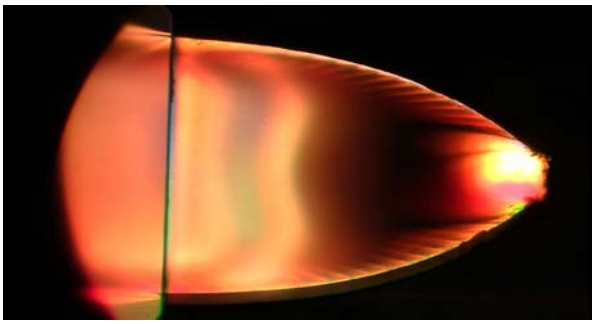

Figure C-12 Schlieren image 30fps, t=0.432s

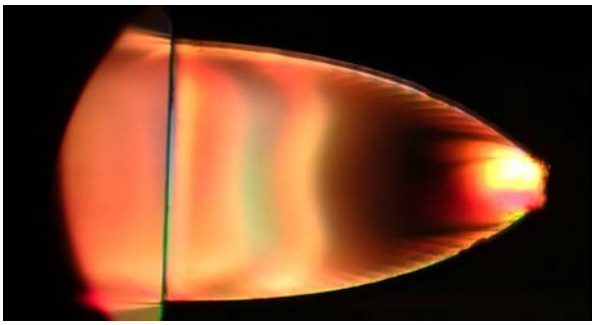

Figure C-13 Schlieren image 30fps, t=0.465s

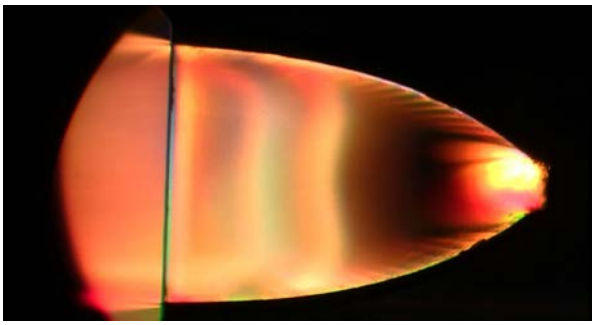

Figure C-14 Schlieren image 30fps, t=0.498s

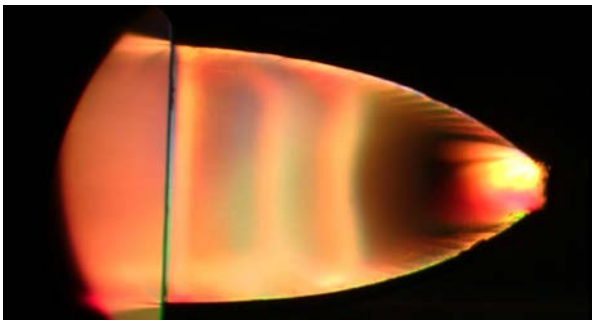

Figure C-15 Schlieren image 30fps, t=0.531s

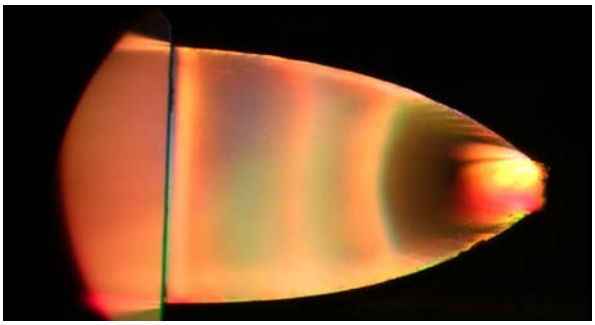

Figure C-16 Schlieren image 30fps, t=0.565s

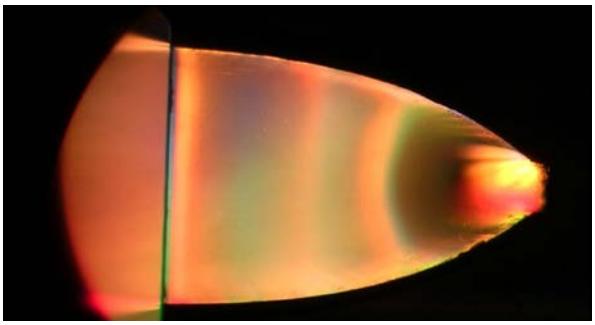

Figure C-17 Schlieren image 30fps, t=0.598s

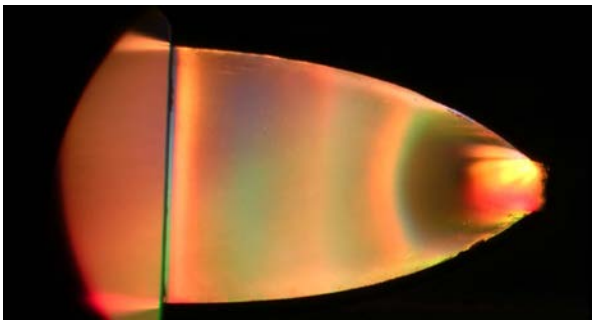

Figure C-18 Schlieren image 30fps, t=0.631s

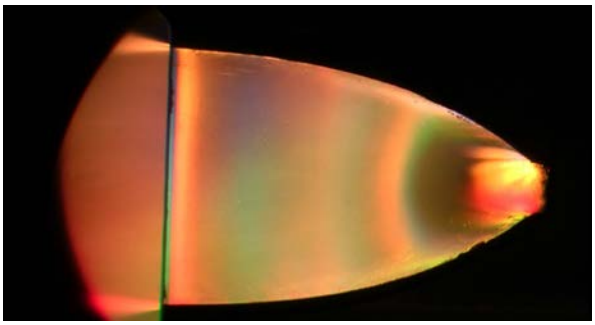

Figure C-19 Schlieren image 30fps, t=0.664s

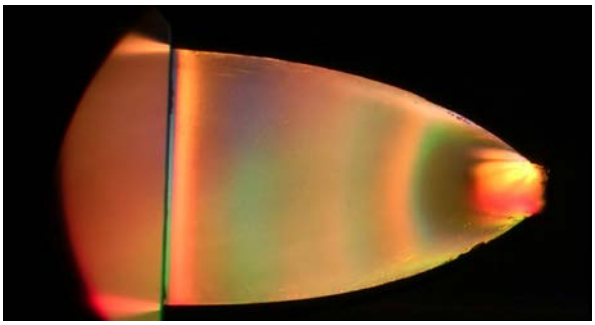

Figure C-20 Schlieren image 30fps, t=0.697s

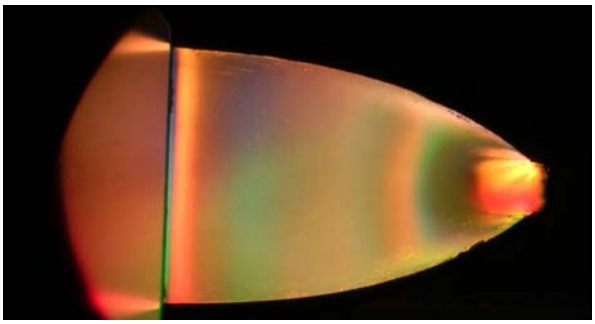

Figure C-21 Schlieren image 30fps, t=0.731s

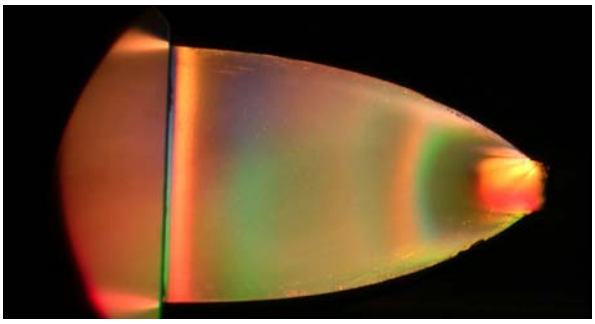

Figure C-22 Schlieren image 30fps, t=0.764s

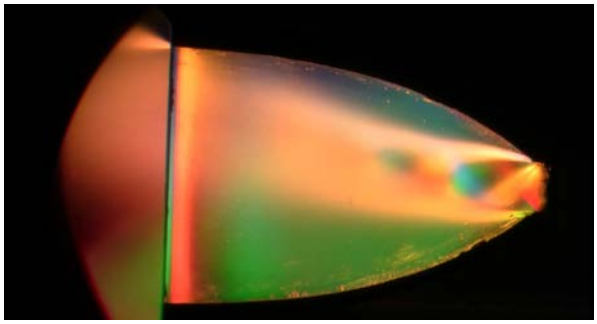

Figure C-23 Schlieren image 30fps, t=0.797s

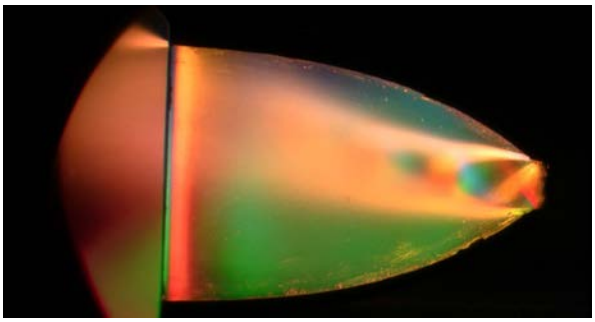

Figure C-24 Schlieren image 30fps, t=0.830s

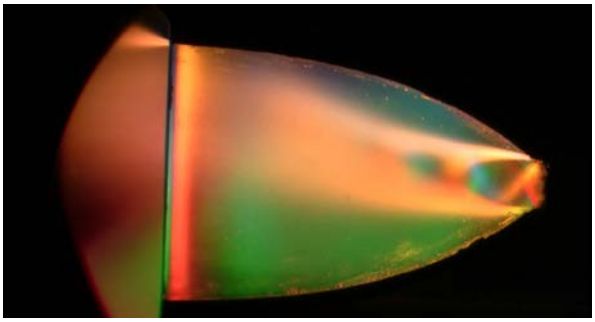

Figure C-25 Schlieren image 30fps, t=0.864s

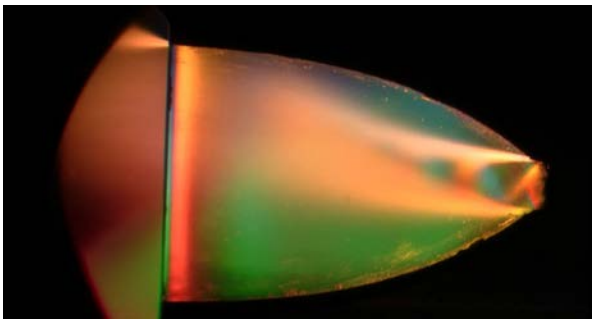

Figure C-26 Schlieren image 30fps, t=0.897s

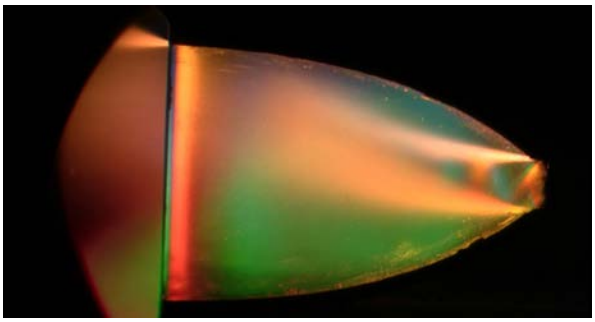

Figure C-27 Schlieren image 30fps, t=0.930s

APPENDIX D: METHOD OF CHARACTERISTICS NUMERICAL SOLUTION

```
function moc  %                                                    2012
Thorsett-Hill
%This program does the MOC calculations for an interior node
clc;
%----o----o----o----o----data input----o----o----o----o----o----o
gamma = 1.667;   %ratio of specific heats
th_left =   14.99  ; %left-running thetam,degrees
nu_left = 21.03    ;    %PM function for left-running
characteristic,deg
xleft =     .3823  ;
yleft =     .1678 ;
th_right =  22.84           ;   %right-running theta,deg
nu_right =  22.84     ;   %PM function for right-running char, deg
xright =      .2633  ;
yright =    .2388  ;
%----o----o----o----o----end data input----o----o----o----o----o----
o
nu = (nu_right + nu_left)/2 + (th_right - th_left)/2; %new value of
nu,deg
theta = (nu_right - nu_left)/2 + (th_right + th_left)/2; %new
theta,deg
M_right = newton(nu_right*pi/180,gamma); % Mach number for rr char
M_left = newton(nu_left*pi/180,gamma); % Mach number for lr char
Mach = newton(nu*pi/180,gamma); %new Mach number
mu = asin(1/Mach)*180/pi;       %Mach angle at new Mach number
mu_right = asin(1/M_right)*180/pi;  %Mach angle for right running
mu_left = asin(1/M_left)*180/pi;    %Mach angle for left running
mright = tan(((th_right+theta)/2-(mu_right+mu)/2)*pi/180); %slope
for rt ch
mleft = tan(((th_left+theta)/2+(mu_left+mu)/2)*pi/180); %slope for
rt ch
x=(yleft-yright+mright*xright-mleft*xleft)/(mright-mleft);%new x
y=(mleft*(mright*xright-yright)+mright*(yleft-mleft*xleft))/(mright-
mleft);
%fprintf(' M_right = %g      M_left = %g\n',M_right,M_left)
fprintf(' nu = %g   theta = %g    Mach = %g \n',nu,theta,Mach);
fprintf(' r_slope = %g  l_slope =
%g\n',atan(mright)*180/pi,atan(mleft)*180/pi);
fprintf(' x = %g   y = %g   mu = %g\n',x,y,mu);
fprintf('x_scale = %g          y_scale = %g\n',x*4,y*4);
end %moc
%-------------------------------------------------------------------
-------
function root = newton(nu,gamma)
%locate the root using the Newton-Raphson technique
count = 0;                %count the number of times through the
loop
M = 2.5;                  %initial guess for Mach number (used in
Newton)
```

```
while(abs(f(nu,M,gamma)) >= .0001) %while not converged
    count = count + 1;    %increment counter
    M = M - f(nu,M,gamma)/fprime(nu,M,gamma);
    if count > 500        %solver failed
        fprintf('root not found');
        break             %quit looking after 500 attempts
    end
end %while
root = M; %return current root
end %newton
%-------------------------------------------------------------------
-------
function fx = f(nu,M,gamma) %evaluate function at current Mach
    fx = get_nu(M,gamma) - nu;
    %RHS - nu is zero for correct value of Mach
end
%-------------------------------------------------------------------
-------
function fp = fprime(nu,M,gamma) %evaluate the derivative
numerically
     fp = (f(nu,M + .001,gamma) - f(nu,M,gamma))/.001;
end
%-------------------------------------------------------------------
-----
function nu = get_nu(M,gamma)
  gp = (gamma + 1)/(gamma - 1);
  M2 = M*M;
  nu = sqrt(gp)*atan(sqrt((M2-1)/gp))-atan(sqrt(M2-1));
end %get_nu
```

APPENDIX E: NUMERICAL SOLUTION FOR A SUPERSONIC COMPRESSION CORNER

```
function theta_beta_mach  %                    Thorsett-Hill
January 2012
%This program solves the equation which relates deflection
angle (theta),
%shock angle (beta), and upstream Mach number for the supersonic
flow ofa
%calorically-perfect gas over a compression corner, given two of the
%three parameters. A root finder is used to solve for the strong and
weak
%shock beta. The other two are solved explicitly. Downstream Mach is
%calculated, along with static pressure and temperature ratios, as
well
%as pressure ratio across the shock. For a given Mach number, if a
%deflection angle theta is input which is greater than the max
possible
%for an attached shock, the solution fails.
%-----------------------------------------------------------------
-----
clc;           %clear screen
gamma = 1.667; %user input
select = input('input 1 to find theta, 2 to find beta, 3 to find
Mach:');
if select == 1 %calculate shock angle theta given Mach number and
beta
    [theta,beta,M] = get_theta(gamma);
elseif select == 2 %calculate beta given Mach and deflection angle,
theta
    [theta,beta1,M] = get_beta(gamma);
    fprintf('beta for weak shock = %g degrees\n',beta1(1));
    fprintf('beta for strong shock = %g degrees\n',beta1(2));
    fprintf('theta = %g degrees \n',theta*180/pi);
    fprintf('Mach number = %g   \n',M);
    beta = beta1(1)*pi/180; %for downstream Mach calculation
else %calculate Mach number given deflection angle theta and shock
angle beta
    [theta,beta,M] = get_Mach(gamma);
end
if select ~= 2   %beta is single valued
    fprintf('theta = %g degrees \n',theta*180/pi)
    fprintf('beta = %g degrees  \n',180*beta/pi)
    fprintf('upstream Mach number = %g\n',M)
end
Mn1 = M*sin(beta); %normal component of upstream Mach number
Msq = Mn1*Mn1;     %upstream Mach number squared for use in
following eqns
Mn2 = sqrt((Msq+2/(gamma-1))/(2*gamma*Msq/(gamma-1)-1));%norm comp
dwnstr M
M2 = Mn2/sin(beta - theta); %downstream Mach number
```

```
p_ratio = 1 + 2*gamma*(Msq - 1)/(gamma + 1); %st pres ratio across
shock p2/p1
rho_ratio = (gamma + 1)*Msq/((gamma - 1)*Msq + 2);%density ratio
across shock
T_ratio = p_ratio/rho_ratio; %static temperature ratio across shock
T2/T1
num = 1 + (gamma-1)*M2*M2/2;
den = 1 + (gamma-1)*M*M/2;
Pt2oPt1=p_ratio*(num/den)^(gamma/(gamma-1)); %total pressure ratio
mu = asin(1/M); %mach angle for upstream Mach number
    fprintf('p2/p1 = %g\n',p_ratio);
    fprintf('T2/T1 = %g\n',T_ratio);
    fprintf('Pt2/Pt1 = %g\n',Pt2oPt1);
    fprintf('downstream Mach number = %g\n',M2);
    fprintf('Mach angle (for upstream Mach) = %g\n',mu*180/pi);


%-------------------------------------------------------------------
-----
function [theta,beta,M] = get_theta(gamma)
    beta = input('input shock angle, beta (degrees): ');
    beta = beta*pi/180; %convert to radians
    M = input('input upstream Mach number, M: ');
    num = 2*cot(beta)*(M*M*sin(beta)*sin(beta) - 1);
    den = M*M*(gamma + cos(2*beta)) + 2;
    theta = atan(num/den);
%-------------------------------------------------------------------
-----
function [theta,beta,M] = get_Mach(gamma)
    beta = input('input shock angle, beta (degrees): ');
    beta = beta*pi/180; %convert to radians
    theta = input('input deflection angle, theta: ');
    theta = theta*pi/180; %convert to radians
    num = -2*(tan(theta) + cot(beta));
    den = tan(theta)*(gamma + 1) - 2*tan(theta)*sin(beta)^2 -
2*cot(beta)*sin(beta)^2;
    M = sqrt(num/den);
%-------------------------------------------------------------------
-----
function [theta,beta1,M] = get_beta(gamma) %uses functions
bata1,root,fx and fp
    theta = input('input deflection angle, theta (degrees): ');
    theta = theta*pi/180; %convert to radians
    M = input('input upstream Mach number: ');
    beta1 = findroot(theta, M, gamma);  %beta1 is a two-element
array
%-------------------------------------------------------------------
-----
function beta1 = findroot(theta,M,gamma)
% Incremental Search Root Finder with the Newton-Raphson Method
i = 1;                  %initialize root array index
xleft = 1.e-3;          %input('Input start of interval:');
xright= 90;             %input('Input end of interval:');
nsteps = 20;            %number of steps on the interval
```

```
epsilon = .0001;         %set convergence criterion
dx = (xright - xleft)/nsteps; %determine step size
x = xleft;               %initialize x to left side of the interval
while (x <= xright)      %while beta < 90 degrees
  y = f(x,theta,M,gamma);%evaluate function at left end of intervel
  %fprintf('x = %g    f(x) =  %g\n',x,y);
  x = x + dx;            %increment x (x = beta in degrees)
  yright = f(x,theta,M,gamma); %evaluate function on right side of
interval
  if(y * yright <= 0)          %a root is trapped in the interval
      root = newton(x, epsilon,theta,M,gamma);  %invoke the Newton-
Raphson method
      beta1(i) = root;   %degrees
      %fprintf('root = %6.4f   y =
%6.4g\n',root,f(root,theta,M,gamma));
      i = i+1;           %increment root array index
  end
end



%-------------------------------------------------------------------
-----
function root = newton(x, epsilon,theta,M,gamma)
%locate the root in the sub-interval using the Newton-Raphson
technique
count = 0;
while(abs(f(x,theta,M,gamma)) >= epsilon) %while not converged
    count = count + 1;                    %increment counter
    x = x - f(x,theta,M,gamma)/fprime(x,theta,M,gamma);
    if count > 500
        fprintf('root not found');
        break  %quit looking after 500 attempts
    end
end
root = x; %return current root
%-------------------------------------------------------------------
-----
function fx = f(x,theta,M,gamma) %evaluate function at current x (x
= beta)
    beta = x*pi/180; %convert beta to radians
    num = 2*cot(beta)*(M*M*sin(beta)*sin(beta) - 1);
    den = M*M*(gamma + cos(2*beta)) + 2;
    fx =-tan(theta)+num/den; %fx is the theta-beta-Mach eq'n set to
zero
%-------------------------------------------------------------------
-----
function fp = fprime(x,theta,M,gamma) %evaluate the derivative
numerically
     fp = (f(x + .001,theta,M,gamma) - f(x,theta,M,gamma))/.001; %x
= beta
```